

SYNTHESIS AND CHARACTERIZATION OF CARBON
MONOXIDE-RELEASING MOLECULES (CORMS) AS
BIOACTIVE AGENTS

LEE SHIAW XIAN

FACULTY OF SCIENCE
UNIVERSITI MALAYA
KUALA LUMPUR

2021

SYNTHESIS AND CHARACTERIZATION OF CARBON
MONOXIDE-RELEASING MOLECULES (CORMS) AS
BIOACTIVE AGENTS

LEE SHIAW XIAN

THESIS SUBMITTED IN FULFILLMENT OF THE
REQUIREMENTS FOR THE DEGREE OF DOCTORAL OF
PHILOSOPHY

DEPARTMENT OF CHEMISTRY
FACULTY OF SCIENCE
UNIVERSITI MALAYA
KUALA LUMPUR

2021

UNIVERSITI MALAYA
ORIGINAL LITERARY WORK DECLARATION

Name of Candidate: **LEE SHIAW XIAN**

Matric No: **SVA180022**

Name of Degree: **DOCTOR OF PHILOSOPHY**

Title of Thesis ("this work"):

SYNTHESIS AND CHARACTERIZATION OF CARBON MONOXIDE-RELEASING MOLECULES (CORMS) AS BIOACTIVE AGENTS

Field of Study:

INORGANIC CHEMISTRY (ORGANOMETALLICS)

I do solemnly and sincerely declare that:

- (1) I am the sole author/writer of this Work;
- (2) This Work is original;
- (3) Any use of any work in which copyright exists was done by way of fair dealing and for permitted purposes and an excerpt or extract from, or reference' to or reproduction of any copyright work has been disclosed expressly and sufficiently and the title of the Work and its authorship have been acknowledged in this Work;
- (4) I do not have any actual knowledge nor do I ought reasonably to know that the making of this work constitutes an infringement of any copyright work;
- (5) I hereby assign all and every rights in the copyright to this Work to the University of Malaya ('UM'), who henceforth shall be owner of the copyright in this Work and that any reproduction or the used in any form or by any means whatsoever is prohibited without the written consent of UM having been first had and obtained;
- (6) I am fully aware that if in the course of making this Work I have infringed any copyright whether intentionally or otherwise, I may be subject to legal action or any other action as may be determined by UM.

Candidate's Signature

Date: 9/7/2021

Subscribed and solemnly declared before,

Witness's Signature

Date: 9/7/2021

Name:

Designation

SYNTHESIS AND CHARACTERIZATION OF CARBON MONOXIDE- RELEASING MOLECULES (CORMS) AS BIOACTIVE AGENTS

ABSTRACT

Despite the toxicity of CO, the development of carbon monoxide-releasing molecules (CORMs) has gained increasing popularity since the discovery of the potential therapeutic properties of CO towards human body. In this study, four series of UV activable photoCORMs with the general structure of $ML(CO)_4$ and $M_2L(CO)_8$ (Bimetallic), where $M = Cr, Mo, \text{ and } W$, were synthesized by reacting group 6 hexacarbonyl ($Cr, Mo, \text{ and } W$) with four new Schiff base ligands based on phenanthroline containing fluorene, 2-hydroxynaphthalene, 2-hydroxy-3-methoxy and phenylene-phenanthroline as side groups (Correspond to **L1, L2, L3, and L4**). All the synthesized photoCORMs release CO in the presence of UV light (365 nm). All compounds were characterized by FT-IR, 1H -NMR, ^{13}C -NMR, and CHN elemental analysis. Twelve X-ray crystal structures were obtained out of the sixteen synthesized compounds. The half-life and the number of CO released of the synthesized photoCORMs were studied using a three-layered myoglobin solution which is a modified version of the standard myoglobin assay. Chromium photoCORMs **C1, C2, C3, and C4** had much shorter half-life compared to molybdenum and tungsten photoCORMs. Molybdenum and tungsten photoCORMs were stable in 10% DMSO-PBS solution in the absence of light over 48 hours but chromium photoCORMs showed signs of decomposition. All compounds were subjected to anticancer and antimicrobial studies in the absence and presence of UV light illumination. The synthesized photoCORMs showed notable photo-induced cytotoxicity against human colorectal cancer cell lines (HT-29 and HCT 116) and showed remarkably high selectivity when tested against the human normal colon fibroblast (CCD18-Co). However, all photoCORMs were generally non-active against all the tested microbes and only the second and the third series photoCORMs displayed slight photo-induced

antimicrobial activities. The SwissADME simulation predicted that most of the synthesized compounds possess “drug-like” properties.

Keywords: Carbon monoxide, UV activable photoCORMs, Schiff base ligands, three-layered myoglobin solution, antimicrobial, anticancer.

Universiti Malaya

SINTESIS DAN PENCIRIAN TERHADAP MOLEKUL PELEPASAN KARBON MONOKSIDA (CORMS) SEBAGAI AGEN BIOAKTIF

ABSTRAK

Pengembangan molekul pelepasan karbon monoksida telah mendapati populariti yang semakin tinggi sejak penemuan potensi karbon monoksida sebagai agen terapi terhadap manusia walaupun karbon monoksida adalah berbahaya. Dalam penyelidikan ini, empat siri fotoCORMs dengan struktur $ML(CO)_4$ dan $M_2L(CO)_8$ (Bimetallik) boleh diaktifkan dengan cahaya UV setelah disintesis menggunakan heksakarbonil dari unsur kumpulan 6 (Cr, Mo, and W) dan bes ligan Schiff baharu yang berasal daripada fenantrolina. Semua fotoCORMs mampu melepaskan karbon monoksida di hadapan cahaya UV (365 nm). Semua sebatian telah dicirikan dengan kaedah FT-IR, 1H -NMR, ^{13}C -NMR, dan analisis unsur CHN. Dua belas struktur kristal X-ray telah diperolehi. Separuh hayat dan jumlah karbon monoksida yang telah dilepaskan oleh fotoCORMs telah pun didapati dengan cara larutan myoglobin tiga lapis. FotoCORMs berasal dari kromium yang dinamakan **C1**, **C2**, **C3**, and **C4** mempunyai separuh hayat yang rendah dibandingkan dengan molibdenum dan fotoCORMs tungsten. Selain itu, fotoCORMs yang berasal dari molibdenum dan tungsten adalah stabil di dalam larutan 10% DMSO-PBS yang berada dalam keadaan yang tiada cahaya untuk 48 jam. Namun, fotoCORMs yang berasal dari kromium adalah tidak stabil di dalam 10% DMSO-PBS dan telah terurai. Aktiviti antikanser dan antimikrobial oleh semua sebatian telah pun dianalisis di dalam keadaan yang tiada dan ada sinaran UV. Semua fotoCORMs telah menunjukkan ciri-ciri sitotoksik terhadap sel kanser kolorektal manusia (HT-29 and HCT 116) apabila disinarkan dengan cahaya UV dan menunjukkan ciri-ciri selektif terhadap sel kanser kolorektal manusia apabila diujikan dengan sel biasa fibroblast kolon manusia (CCD18-Co). Namun begitu, semua fotoCORMs tidak menunjukkan aktiviti di ujian antimikrob. Tetapi, fotoCORMs dari siri dua dan tiga menunjukkan sedikit aktiviti antimikrob apabila disinarkan oleh cahaya UV.

Simulasi dari SwissADME meramalkan bahawa hampir semua sebatian mempunyai ciri-ciri sebagai ubat.

Kata kunci: Karbon monoksida, UV aktif fotoCORMs, Schiff base ligan, larutan myoglobin tiga lapis, antimikrob, antikanser.

Universiti Malaya

ACKNOWLEDGEMENT

I would like to extend my deepest gratitude to my supervisors, Prof. Dr. Richard Wong Chee Seng and Associate. Prof. Dr. Tan Kong Wai for their supervision and guidance throughout the project. I would also like to express my deepest appreciation to Associate. Prof. Dr. Sim Kae Shin, Dr. Cheow Yuen Lin, Tan Chun Hoe, and Mah Wee Li for their guidance and help in anticancer and antimicrobial studies.

I would like to extend my sincere thanks to MyBrainSc scholarship and Ministry of Education for their financial support throughout my study. I would like to thank Universiti Malaya and Department of Chemistry for their advice and support. I am also grateful to have Choong Zheng Lin and Gan Chun Hau as my mentors and friends throughout my years in the lab.

Lastly, I like to thank my mother, father and sister for their love and supports. They provide me with warmth and never give up on me even during my worst time and behaviour.

TABLE OF CONTENTS

ABSTRACT	iii
ABSTRAK	v
ACKNOWLEDGEMENTS	vii
TABLE OF CONTENTS	viii
LIST OF FIGURES AND SCHEMES	xi
LIST OF TABLES	xv
LIST OF ABBREVIATIONS	xviii
LIST OF APPENDICES	xx
CHAPTER 1: INTRODUCTION	1
1.1 Introduction	1
1.2 Objectives	4
1.3 Scope of Studies	4
CHAPTER 2: LITERATURE REVIEW	5
2.1 Carbon Monoxide (CO)	5
2.1.1 Toxicity of CO	5
2.1.2 Biological Role of CO	5
2.1.3 Therapeutic Potentials of CO	6
2.2 Carbon Monoxide-releasing Molecules (CORMs)	8
2.3 Photo-activable CORMs (PhotoCORMs)	11
2.4 Schiff Base Ligands and its PhotoCORMs	16
CHAPTER 3: METHODOLOGY	19

3.1 Materials and Solutions	19
3.2 Physical Measurements	20
3.3 Syntheses	20
3.3.1 Synthesis of Schiff Base Ligands	20
3.3.2 Synthesis of PhotoCORMs	23
3.4 Myoglobin Assay	30
3.5 PhotoCORMs Dark Stability Test	31
3.6 Cytotoxicity Evaluation	32
3.6.1 Cell Culture	32
3.6.2 MTT Cytotoxicity Assay	32
3.7 Antimicrobial Study	33
 CHAPTER 4: RESULTS AND DISCUSSION	 34
4.1 Structural Elucidations	34
4.1.1 Infra-Red Spectroscopy	34
4.1.2 ¹ H-NMR Spectroscopy	37
4.1.3 ¹³ C-NMR Spectroscopy	45
4.1.4 UV-Vis Spectroscopy	52
4.1.5 X-ray Crystallography	55
4.2 Myoglobin Assays	72
4.2.1 Three-Layered Myoglobin Solution	72
4.2.2 Half-life of PhotoCORMs C1, M1, and T1	75
4.2.3 Half-life of PhotoCORMs C2, M2, and T2	77
4.2.4 Half-life of PhotoCORMs C3, M3, and T3	78
4.2.5 Half-life of PhotoCORMs C4, M4, and T4	79
4.2.6 Overall Half-life of PhotoCORMs	81

4.3 Dark Stability of PhotoCORMs	82
4.4 Cytotoxic Evaluation	87
4.4.1 Cytotoxic Evaluation of L1, C1, M1, and T1	87
4.4.2 Cytotoxic Evaluation of L2, C2, M2, and T2	90
4.4.3 Cytotoxic Evaluation of L3, C3, M3, and T3	93
4.4.4 Cytotoxic Evaluation of L4, C4, M4, and T4	96
4.4.5 Overall Cytotoxic Result	99
4.5 Antimicrobial Study	101
4.5.1 Antimicrobial Activity of L1, C1, M1, and T1	101
4.5.2 Antimicrobial Activity of L2, C2, M2, and T2	104
4.5.3 Antimicrobial Activity of L3, C3, M3, and T3	110
4.5.4 Antimicrobial Activity of L4, C4, M4, and T4	116
4.5.5 Overall Antimicrobial Activity	119
4.6 ADME Properties	120
4.6.1 ADME Calculations of L1, C1, M1, and T1	120
4.6.2 ADME Calculations of L2, C2, M2, and T2	130
4.6.3 ADME Calculations of L3, C3, M3, and T3	140
4.6.4 ADME Calculations of L4, C4, M4, and T4	150
4.6.5 Overall ADME Calculations	160
CHAPTER 5: CONCLUSION	161
5.1 Conclusion	161
5.2 Future works	162
REFERENCES	163
LIST OF PUBLICATIONS	173
APPENDIX	176

LIST OF FIGURES AND SCHEMES

Figure 3.1	: Three-layered myoglobin solution.	31
Figure 4.1	: UV-Vis spectra of L1 , C1 , M1 , and T1 at 60 μ M in 10% DMSO-H ₂ O.	53
Figure 4.2	: UV-Vis spectra of L2 , C2 , M2 , and T2 at 60 μ M in 10% DMSO-H ₂ O.	53
Figure 4.3	: UV-Vis spectra of L3 , C3 , M3 , and T3 at 60 μ M in 10% DMSO-H ₂ O.	54
Figure 4.4	: UV-Vis spectra of L4 , C4 , M4 , and T4 at 60 μ M in 10% DMSO-H ₂ O.	54
Figure 4.5	: Crystal structure and crystal packing viewed along c-axis of L1 .	57
Figure 4.6	: Crystal structure and crystal packing viewed along c-axis of C1 .	58
Figure 4.7	: Crystal structure and crystal packing viewed along c-axis of L2 .	62
Figure 4.8	: Crystal structure and crystal packing viewed along c-axis of C2 .	63
Figure 4.9	: Crystal structure and crystal packing viewed along b-axis of L3 .	66
Figure 4.10	: Crystal structure and crystal packing viewed along c-axis of M3 .	67
Figure 4.11	: Crystal structure and crystal packing viewed along b-axis of L4 .	70
Figure 4.12	: Crystal structure and crystal packing viewed along b-axis of M4 .	71

Figure 4.13	: UV-Vis spectrum of conventional myoglobin assay of M1 (60 μ M) showed deviations in the absorbance.	73
Figure 4.14	: Cuvette before UV irradiation (left). After UV irradiation at 365 nm, the CO released were captured by the myoglobin solution on top, all the insoluble iCORM remained at the bottom layer (right).	74
Figure 4.15	: UV-Vis spectrum of myoglobin assay of M1 (60 μ M) conducted using three-layered myoglobin solution.	74
Figure 4.16	: a) UV-Vis and b) ATR-IR spectra of C1 (60 μ M) in 10% DMSO-PBS buffered solution in at 24 and 48 hours.	83
Figure 4.17	: a) UV-Vis and b) ATR-IR spectra of C2 (60 μ M) in 10% DMSO-PBS buffered solution in at 24 and 48 hours.	84
Figure 4.18	: a) UV-Vis and b) ATR-IR spectra of C3 (60 μ M) in 10% DMSO-PBS buffered solution at 24 and 48 hours.	85
Figure 4.19	: a) UV-Vis and b) ATR-IR spectra of C4 (60 μ M) in 10% DMSO-PBS buffered solution at 24 and 48 hours.	86
Figure 4.20	: The drug-likeness bioavailability radar of L1 .	122
Figure 4.21	: The BOILED-Egg graphical representation of L1	123
Figure 4.22	: The drug-likeness bioavailability radar of C1 .	124
Figure 4.23	: The BOILED-Egg graphical representation of C1 .	125
Figure 4.24	: The drug-likeness bioavailability radar of M1 .	126
Figure 4.25	: The BOILED-Egg graphical representation of M1 .	127
Figure 4.26	: The drug-likeness bioavailability radar of T1 .	128
Figure 4.27	: The BOILED-Egg graphical representation of T1 .	129
Figure 4.28	: The drug-likeness bioavailability radar of L2 .	132
Figure 4.29	: The BOILED-Egg graphical representation of L2 .	133

Figure 4.30	: The drug-likeness bioavailability radar of C2 .	134
Figure 4.31	: The BOILED-Egg graphical representation of C2 .	135
Figure 4.32	: The drug-likeness bioavailability radar of M2 .	136
Figure 4.33	: The BOILED-Egg graphical representation of M2 .	137
Figure 4.34	: The drug-likeness bioavailability radar of T2 .	138
Figure 4.35	: The BOILED-Egg graphical representation of T2 .	139
Figure 4.36	: The drug-likeness bioavailability radar of L3 .	142
Figure 4.37	: The BOILED-Egg graphical representation of L3 .	143
Figure 4.38	: The drug-likeness bioavailability radar of C3 .	144
Figure 4.39	: The BOILED-Egg graphical representation of C3 .	145
Figure 4.40	: The drug-likeness bioavailability radar of M3 .	146
Figure 4.41	: The BOILED-Egg graphical representation of M3 .	147
Figure 4.42	: The drug-likeness bioavailability radar of T3 .	148
Figure 4.43	: The BOILED-Egg graphical representation of T3 .	149
Figure 4.44	: The drug-likeness bioavailability radar of L4 .	152
Figure 4.45	: The BOILED-Egg graphical representation of L4 .	153
Figure 4.46	: The drug-likeness bioavailability radar of C4 .	154
Figure 4.47	: The BOILED-Egg graphical representation of C4 .	155
Figure 4.48	: The drug-likeness bioavailability radar of M4 .	156
Figure 4.49	: The BOILED-Egg graphical representation of M4 .	157
Figure 4.50	: The drug-likeness bioavailability radar of T4 .	158
Figure 4.51	: The BOILED-Egg graphical representation of T4 .	159
Figure 4.52	: The chemical structure of Cyclosporine A.	160
Scheme 3.1	: Schematic representation of the formation of L1 .	21
Scheme 3.2	: Schematic representation of the formation of L2 .	21
Scheme 3.3	: Schematic representation of the formation of L3 .	22

Scheme 3.4	: Schematic representation of the formation of L4 .	23
Scheme 3.5	: Schematic representation of the synthesis of C1 , M1 , and T1 .	24
Scheme 3.6	: Schematic representation of the synthesis of C2 , M2 , and T2 .	26
Scheme 3.7	: Schematic representation of the synthesis of C3 , M3 , and T3 .	28
Scheme 3.8	: Schematic representation of the synthesis of bimetallic photoCORMs C4 , M4 , and T4 .	30

Universiti Malaysia

LIST OF TABLES

Table 2.1	: Therapeutic effects of gaseous/inhaled CO in preclinical models in mice.	6
Table 2.2	: Chemical structures, half-life, and biological effects of early CORMs.	9
Table 2.3	: Example of photoCORMs and their potential biological properties.	12
Table 2.4	: PhotoCORMs containing Schiff base ligand and potential biological properties.	17
Table 4.1	: Selected infrared frequencies for L1 , C1 , M1 , and T1 .	35
Table 4.2	: Selected infrared frequencies for L2 , C2 , M2 , and T2 .	35
Table 4.3	: Selected infrared frequencies for L3 , C3 , M3 , and T3 .	36
Table 4.4	: Selected infrared frequencies for L4 , C4 , M4 , and T4 .	36
Table 4.5	: ¹ H-NMR shifting of L1 , C1 , M1 , and T1 .	38
Table 4.6	: ¹ H-NMR shifting of L2 , C2 , M2 , and T2 .	40
Table 4.7	: ¹ H-NMR shifting of L3 , C3 , M3 , and T3 .	42
Table 4.8	: ¹ H-NMR shifting of L4 , C4 , M4 , and T4 .	44
Table 4.9	: ¹³ C-NMR shifting of L1 , C1 , M1 , and T1 .	46
Table 4.10	: ¹³ C-NMR shifting of L2 , C2 , M2 , and T2 .	48
Table 4.11	: ¹³ C-NMR shifting of L3 , C3 , M3 , and T3 .	49
Table 4.12	: ¹³ C-NMR shifting of L4 , C4 , M4 , and T4 .	51
Table 4.13	: Crystallographic data summary for L1 , C1 , M1 , and T1 .	56
Table 4.14	: Crystallographic data summary for L2 , C2 , M2 , and T2 .	61
Table 4.15	: Crystallographic data summary for L3 and M3 .	65
Table 4.16	: Crystallographic data summary for L4 and M4 .	69
Table 4.17	: Half-life ($t_{1/2}$) of C1 , M1 , and T1 at different concentrations.	76

Table 4.18	: Number of CO released per molecule of C1 , M1 , and T1 .	76
Table 4.19	: Half-life ($t_{1/2}$) of C2 , M2 , and T2 at different concentrations.	77
Table 4.20	: Number of CO released per molecule of C2 , M2 , and T2 .	78
Table 4.21	: Half-life ($t_{1/2}$) of C3 , M3 , and T3 at different concentrations.	79
Table 4.22	: Number of CO released per molecule of C3 , M3 , and T3 .	79
Table 4.23	: Half-life ($t_{1/2}$) of C4 , M4 , and T4 at different concentrations.	80
Table 4.24	: Number of CO released per molecule of C4 , M4 , and T4 .	80
Table 4.25	: IC ₅₀ value of L1 , C1 , M1 , and T1 against HT-29, HCT 116 and CCD18-Co in the presence and absence of UV light illumination.	89
Table 4.26	: Selectivity Index (SI) of L1 , C1 , M1 , and T1 against HT-29, HCT 116 and CCD18-Co in the presence and absence of UV light illumination.	90
Table 4.27	: IC ₅₀ value of L2 , C2 , M2 , and T2 against HT-29, HCT 116 and CCD18-Co in the presence and absence of UV light illumination.	92
Table 4.28	: Selectivity Index (SI) of L2 , C2 , M2 , and T2 against HT-29, HCT 116 and CCD18-Co in the presence and absence of UV light illumination.	93
Table 4.29	: IC ₅₀ value of L3 , C3 , M3 , and T3 against HT-29, HCT 116 and CCD18-Co in the presence and absence of UV light illumination.	95
Table 4.30	: Selectivity Index (SI) of L3 , C3 , M3 , and T3 against HT-29, HCT 116 and CCD18-Co in the presence and absence of UV light illumination.	96
Table 4.31	: IC ₅₀ value of L4 , C4 , M4 , and T4 against HT-29, HCT 116 and CCD18-Co in the presence and absence of UV light illumination.	98
Table 4.32	: Selectivity Index (SI) of L4 , C4 , M4 , and T4 against HT-29, HCT 116 and CCD18-Co in the presence and absence of UV.	99

Table 4.33	: MIC value for L1, C1, M1, and T1 against a series of microbes.	102
Table 4.34	: MBC value for L1, C1, M1, and T1 against a series of microbes.	103
Table 4.35	: MIC value for L2, C2, M2, and T2 against a series of microbes in the absence of UV light.	106
Table 4.36	: MIC value for L2, C2, M2, and T2 against a series of microbes in the presence of UV light.	107
Table 4.37	: MBC value for L2, C2, M2, and T2 against a series of microbes in the absence of UV light.	108
Table 4.38	: MBC value for L2, C2, M2, and T2 against a series of microbes in the presence of UV light.	109
Table 4.39	: MIC value for L3, C3, M3, and T3 against a series of microbes in the absence of UV light.	112
Table 4.40	: MIC value for L3, C3, M3, and T3 against a series of microbes in the presence of UV light.	113
Table 4.41	: MBC value for L3, C3, M3, and T3 against a series of microbes in the absence of UV light.	114
Table 4.42	: MBC value for L3, C3, M3, and T3 against a series of microbes in the presence of UV light.	115
Table 4.43	: MIC value for L4, C4, M4, and T4 against a series of microbes.	117
Table 4.44	: MBC value for L4, C4, M4, and T4 against a series of microbes.	118
Table 4.45	: ADME properties of L1, C1, M1, and T1 .	121
Table 4.46	: ADME properties of L2, C2, M2, and T2	131
Table 4.47	: ADME properties of L3, C3, M3, and T3 .	141
Table 4.48	: ADME properties of L4, C4, M4, and T4 .	151

LIST OF ABBREVIATIONS

ADME	: Absorption, distribution, metabolism, and excretion
ATR-IR	: Attenuated total reflectance Infra-red
BBB	: Blood brain barrier
cGMP	: Cyclic guanosine monophosphate
CLP	: Cecal ligation and puncture
CO	: Carbon monoxide
CORMs	: Carbon monoxide releasing molecules
D.P.	: Decomposition point
EMEM	: Eagle's minimum essential medium
FBS	: Fetal bovine serum
FT-IR	: Fourier-transform infra-red
HBA	: Hydrogen bond acceptor
HbCO	: Carboxyhemoglobin
HBD	: Hydrogen bond donor
HIA	: Human gastrointestinal absorption
HO	: Heme oxygenase
iCORMs	: Inactive-CORMs
IR	: Infra-red
IRI	: Ischemia-reperfusion injury
Mb	: Myoglobin
MBC	: Minimum bactericidal concentration
MbCO	: Carboxymyoglobin
MHA	: Mueller-Hinton agar
MHB	: Mueller-Hinton broth
MIC	: Minimum inhibitory concentration

MLCT	: Metal-to-ligand charge transfer
M.P.	: Melting point
NMR	: Nuclear magnetic resonance
NSAIDs	: Non-steroidal anti-inflammatory drugs
PBS	: Phosphate buffered saline
PGP	: Permeability glycoprotein
PhotoCORMs	: Photo-activable carbon monoxide-releasing molecules
PNA	: Peptide nucleic acids
ROS	: Reactive oxygen species
RotB	: Rotatable bond
SD	: Standard deviation
sGC	: Soluble guanylate cyclase
SI	: Selectivity index
THF	: Tetrahydrofuran
TMNO	: Trimethylamine-N-oxide
TPSA	: Topological polar surface area

LIST OF APPENDICES

APPENDIX A	: Crystal structures and crystal packings viewed along c-axis for M1 , T1 , M2 , and T2 .	176
APPENDIX B	: Selected bond lengths (Å) and bond angles (°) for all compounds with x-ray crystal structures.	180

Universiti Malaysia

CHAPTER 1: INTRODUCTION

1.1 Introduction

Contrary to the public impression that carbon monoxide (CO) is a dangerous gas, CO was found to be produced in human body in small quantity by the heme oxygenase enzyme (HO-1) during the catabolism of heme (Mann & Motterlini, 2007). CO acts as a signalling molecule mimicking the function of nitric oxide (NO) as a vasodilator in human cardiovascular system (Mann, 2010). Besides its biological role in the body, CO was discovered to be a potential therapeutic agent. Studies suggest that CO act as anti-inflammatory, anti-apoptotic, anti-proliferative and vascular protective agent (Motterlini et al., 2002; Ryter & Otterbein, 2004). However, the administration of CO gas through inhalation as a treatment is not a viable option as CO gas will only be localized in the lung area and strongly bound to the heme group in the blood cells before it could be transported to the targeted area in the body (Gorman et al., 2003). This prompted numerous researches into the development of CO carriers such as carbon monoxide-releasing molecules (CORMs) to potentially transport the therapeutic CO to the targeted site in human body (Motterlini et al., 2002). CORMs were first reported by Motterlini and co-workers in which several clinical studies based on the potential therapeutic properties of CO had been conducted using $[\text{Mn}_2(\text{CO})_{10}]$ (CORM-1), $[\text{Ru}(\text{CO})_3\text{Cl}_2]_2$ (CORM-2), and *fac*- $[\text{RuCl}(\text{glycinato})(\text{CO})_3]$ (CORM-3) (James et al., 2003; Foresti et al., 2004; Iacono et al., 2011; Motterlini et al., 2002; Yabluchanskiy et al., 2012). Most of the CORMs are developed based on transition metal series such as Co, Mn, Re, Fe, Ru, Cr, Mo and W (Kautz et al., 2016). However, the earlier generation CORMs release CO spontaneously and uncontrollably, hence the amount of CO reaches the targeted site is significantly reduced (Romão et al., 2012). This sparked the development of activable

CORMs in which the CORMs are able to release CO in response to activations or triggers such as light irradiation (UV, visible, infrared and far-infrared), enzyme (esterase) and magnetic heating (Botov et al., 2013; Kunz et al., 2013; Romanski et al., 2011; Wright & Wright, 2016). The more common types are the photo-activable carbon monoxide-releasing molecules, photoCORMs in which the term was first suggested by Ford and co-workers (Rimmer et al., 2012). The investigation of photoCORMs has been conducted to evaluate their potential as prodrugs to release CO in a controlled and therapeutic fashions. For instance, Tinajero-Trejo et al. has reported that Mn-based photoCORMs significantly reduced the viability and growth of *Escherichia coli*, EC958 pathogenic strain (Tinajero-Trejo et al., 2016). Moreover, photo-induced cytotoxicity of photoCORMs against several human cancer cell lines were also reported. For example, derivatives of manganese tricarbonyl complexes with attached ligands were cytotoxic against HT-29 colon cancer cell line and their cytotoxicity were significantly improved upon UV light illumination (Jimenez et al., 2018).

To the best of our knowledge, most of the photoCORMs were developed based on group 7 and 8 elements (Mn, Re, Fe, and Ru), while those from group 6 elements are still lacking (Bischof et al., 2013; Jimenez et al., 2018; Pierri et al., 2012; Slanina & Šebej, 2018). Despite the scarcity, group 6 compounds showed promising photo-induced CO releasing properties in the development of photoCORMs when combined with ligands containing high number of double bond conjugations (Chakraborty et al., 2014). In this study, four new ligands based on phenanthroline with high double-bond conjugations were synthesized and reacted with group 6 hexacarbonyls to form UV activable photoCORMs. The first series involved conjugation with fluorene because it is a well-known fluorophore and could lead to the formation of a fluorescent CORMs. The planar fluorene ring may also enhance cytotoxicity by promoting the binding to DNA. On the other hand, the second and third series contain 2-hydroxynaphthalene, and 2-hydroxy-3-

methoxybenzene moiety that bestowed the compounds with additional binding sites that can promote solubility or formation of dinuclear complexes. The final series with bisphenanthroline moieties will enable the exploration on the effect of dinuclear CORMs on bioactivity. The chemical structures of the compounds were fully characterized and their CO releasing half-life, cytotoxicity, and antimicrobial activities were evaluated.

Universiti Malaya

1.2 Objectives

1. To synthesize new highly conjugated phenanthroline ligands containing fluorene, 2-hydroxy naphthalene, and 2-hydroxy-3-methoxybenzene as side chains with potential antimicrobial and anticancer properties.
2. To synthesize new ligand with bisphenanthroline moieties that can bind to two metal centres to form bimetallic photoCORMs.
3. To synthesize new group 6 (chromium, molybdenum, and tungsten) UV activable photoCORMs that will release CO in response to light.
4. To develop a modified version of standard myoglobin assay to allow a more accurate CO releasing kinetic determination.
5. To study the antimicrobial and anticancer properties of all the synthesized compounds.
6. To determine the potential photo-induced antimicrobial and anticancer properties of the synthesized photoCORMs.

1.3 Scope of Studies

In this research, four new series of group 6 photoCORMs based on chromium, molybdenum, and tungsten carbonyl were synthesized by reacting with the four new highly conjugated ligands based on phenanthroline derivatives. The CO releasing properties of the compounds were evaluated using a modified version of myoglobin solution assay (Three-layered myoglobin solution), and their potential photo-induced antimicrobial and anticancer activities were also studied.

CHAPTER 2: LITERATURE REVIEW

2.1 Carbon monoxide (CO)

2.1.1 Toxicity of CO

The lethal nature of the CO towards human has been known for nearly 2 centuries (Weaver, 2009). Common symptoms of CO poisoning are shortness of breath, headache, nausea, and in serious case it can be fatal because CO is classified as chemical asphyxiant (Gorman et al., 2003). Excessive CO exposure through lung inhalation can lead to tissue hypoxia and organ failure due to the fact that hemoglobin in human blood has a much higher affinity for CO than oxygen (O_2). The inhaled CO will compete with O_2 to bind with the heme groups' iron centre of hemoglobin to form carboxyhemoglobin (HbCO) thereby hindering the gaseous exchange process in the lung (Ryter & Otterbein, 2004).

2.1.2 Biological role of CO

Despite its toxicity, numerous research suggested that CO plays several biological roles in human body. CO was found to be produced in human body endogenously through the degradation of heme catalysed by heme oxygenase enzymes (HO). The degradation of each heme catalysed by HO will produce one molecule of CO, iron, and biliverdin (Bauer et al., 2008). CO plays a role in vascular signalling by stimulating the production cyclic guanosine monophosphate (cGMP) through the binding of CO towards soluble guanylate cyclase (sGC). The initiation of the sGC/cGMP biological pathway by CO will cause vascular relaxation, bronchodilation, and smooth muscle relaxation (Cardell et al., 1998; Duckers et al., 2001; Morita et al., 1997).

2.1.3 Therapeutic potentials of CO

The potential therapeutic effects of CO gas had been studied using animal models particularly in mice. Table 2.1 summarised some of the effects of CO studied using preclinical disease models in mice.

Table 2.1: Therapeutic effects of gaseous/inhaled CO in preclinical models in mice.

Induced disease	Therapeutic effects of CO
Autoimmune disease	Reverses paralysis in induced autoimmune neuroinflammation after the exposure of 450 ppm of CO gas for 30 days (Chora et al., 2007).
Ischemia-reperfusion injury	Prevents Ischemia-reperfusion injury (IRI) and cell apoptosis after subjected to 250 ppm of CO gas (Kohmoto et al., 2008; Mishra et al., 2006).
Acute inflammation and injury in lung	Curbs hyperoxia-induced lung inflammation and lung injury after the inhalation of 250 ppm of CO (Otterbein et al., 1999; Otterbein et al., 2003).
Acute liver failure	Stops fulminant hepatic failure after the exposure to 100 – 500 ppm of CO gas (Tsui et al., 2007).

Table 2.1, Continued.

Induced disease	Therapeutic effects of CO
Bacterial infections	Ameliorates multiple organ failures caused by Gram-positive and -negative bacterial infections after the administration of 250 ppm of CO gas (Chung et al., 2008; Desmard et al., 2009).
Hemorrhagic shock	Prevents organ failure and improves tissues availability after resuscitation and administration of 250 ppm of CO gas (Cabrales et al., 2007; Zuckerbraun et al., 2005).
Pulmonary hypertension	Reverses the size of right heart and lowers the pulmonary artery pressure after administration of 250 ppm of CO gas per hour for 21 days (Dubuis et al., 2005; Zuckerbraun et al., 2006).
Cardiac graft rejection	Increases survival rate after exposure of 20 ppm of CO and prevents cardiac graft rejection after exposure of 250 – 400 ppm of CO for 5 – 6 days (Nakao et al., 2006; Sato et al., 2001).
Myocardial infarction	Prevents infarct mass caused by cardiac injury after subjected to 250 – 1000 ppm of CO gas (Guo et al., 2004).

2.2 Carbon monoxide-releasing molecules (CORMs)

Despite the therapeutic effects, inhalation of CO gas is not utilized as a mean to treat patient because hemoglobin in blood has strong affinity for CO as mentioned previously and the amount of CO that reaches the targeted site in the body is very low. Besides, quantitative administration of CO is difficult to achieve and the dosage is limited by the toxicity of CO inhaled through the lung. To overcome the aforementioned problems, carbon monoxide-releasing molecules (CORMs) based on transition metal complexes were developed and proposed as a potential vehicles or prodrugs to carry and transport the therapeutic CO in the bloodstream to the targeted sites in the body without going through the lung. The early examples of CORMs such as CORM-2, CORM-3, ALF186, and ALF062 had been subjected to numerous biological studies to determine the therapeutic potentials of CO and the compounds (Motterlini & Otterbein, 2010). The chemical structures, half-life, and biological effect of the early CORMs are shown in Table 2.2.

Table 2.2: Chemical structures, half-life, and biological effects of early CORMs.

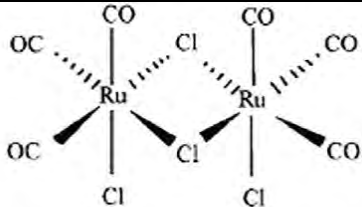
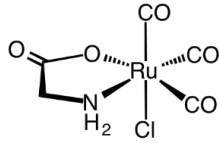
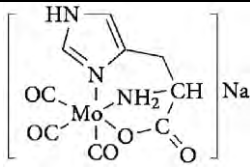
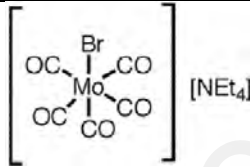
Chemical structures	Half-life, CO releasing trigger	Biological properties
 <p>CORM-2</p> <p>$[\text{Ru}(\text{CO})_3\text{Cl}_2]_2$</p>	<p>$t_{1/2} = 1$ *mins,</p> <p>solvent</p> <p>displacement</p>	<p>Prolong aortic graft survival,</p> <p>reduce liver damage induced by</p> <p>cecal ligation and puncture (CLP),</p> <p>reduces mortality and</p> <p>antimicrobial response in mice</p> <p>(Chen et al., 2009; Chung et al., 2008; Tsoyi et al., 2009).</p>
 <p>CORM-3</p> <p>$[\text{Ru}(\text{CO})_3\text{Cl}(\text{glycinato})]^-$</p>	<p>$t_{1/2} = \sim 1$ mins,</p> <p>Solvent</p> <p>displacement</p>	<p>Prolong cardiac graft survival,</p> <p>induces dilation in afferent</p> <p>arterioles, and prevents</p> <p>inflammation in intestinal</p> <p>musculari, and improves renal</p> <p>microcirculations in animal</p> <p>models (Clark et al., 2003; De</p> <p>Backer et al., 2009; Ren et al., 2008).</p>

Table 2.2, Continued.

Chemical structures	Half-life, CO releasing trigger	Biological properties
 <p>ALF186 [Mo(CO)₃(Histidinato)]Na</p>	<p>$t_{1/2} = \sim 24$ mins,</p> <p>Oxidation, solvent displacement</p>	<p>Stops non-steroidal anti-inflammatory drugs (NSAIDs) induced gastric ulcer, moderate neuroprotective properties, inhibit the expression of inflammatory cytokines Interleukin-6 and slow down the IRI induced inflammation in animal models. (Schallner et al., 2013; Ulbrich et al., 2017).</p>
 <p>ALF062 [Mo(CO)₅Br][NEt₄]</p>	<p>$t_{1/2} = < 30$ mins</p> <p>Oxidation, solvent displacement</p>	<p>Controls antigen-induced arthritis and displayed antimicrobial activity through the induction of reactive oxygen species (ROS) in rat models (Motterlini & Otterbein, 2010; Nobre et al., 2016; Zobi, 2013).</p>

*Mins = minutes

2.3 Photo-activable CORMs (PhotoCORMs)

The earlier CORMs release CO spontaneously and uncontrollably in the presence of oxygen or solvent molecules such as water and DMSO, this caused large amount of CO lost before it could reach the targeted site in the body to be therapeutically useful (Motterlini et al., 2002; Wilson et al., 2013). Hence, this prompted numerous research into more controllable type of CORMs, namely activable CORMs in which the CO release can be triggered by activators such as light source, enzyme, and electromagnetic heating (Botov et al., 2013; Kunz et al., 2013; Romanski et al., 2011; Wright & Wright, 2016). However, the most common type of activable CORMs are photo-activable CORMs (PhotoCORMs) in which the CO release can be triggered by the illumination of light from wide range of wavelengths such as ultraviolet (UV), visible, infrared, and far-infrared light (Wright & Wright, 2016). Table 2.3 showed the list of structures of photoCORMs, activation wavelengths and biological properties.

Table 2.3: Example of photoCORMs and their potential biological properties.

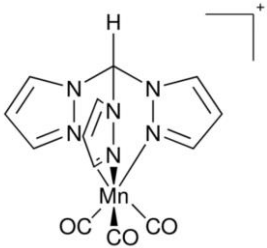
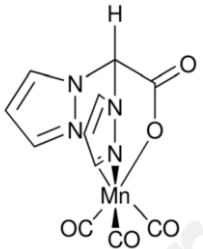
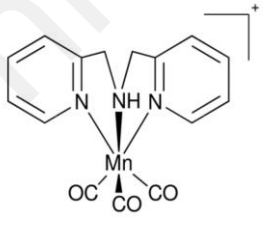
PhotoCORMs	Half-life, activation wavelength	Biological properties
	$t_{1/2} = \text{*n.d.,}$ UV (365 nm)	Photo-induced cytotoxicity against human colon cancer cell line, HT-29 with result comparable to 5- fluorouracil (5-FU) (Niesel et al., 2008).
	$t_{1/2} = 10 - 15 \text{ *mins,}$ UV (366 nm) (Berends & Kurz, 2012).	n.d.
	$t_{1/2} = \text{n.d.,}$ UV (>350 nm)	Induced vascular relaxation in aortic muscle ring of mice after UV illumination (Gonzalez et al., 2012).

Table 2.3, Continued.

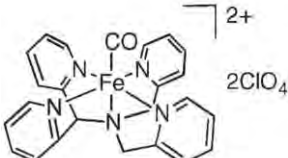
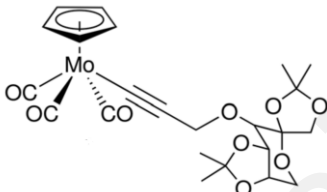
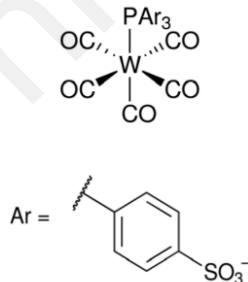
PhotoCORMs	Half-life, activation wavelength	Biological properties
	$t_{1/2} = \text{n.d.},$ UV (365 nm)	Strong photo-induced cytotoxicity against prostate cancer cell PC-3 after 10 minutes of UV light illumination (Jackson et al., 2011).
	$t_{1/2} = 962$ *secs, UV (325 nm) (Zhang et al., 2011).	n.d.
	$t_{1/2} = \text{n.d.},$ UV (315 nm) (Rimmer et al., 2010).	n.d.

Table 2.3, Continued.

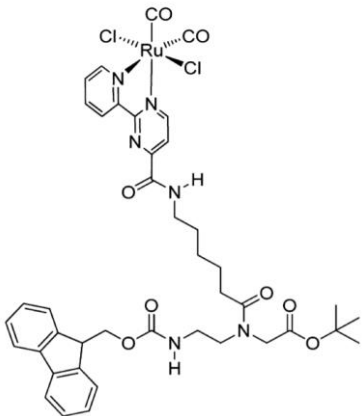
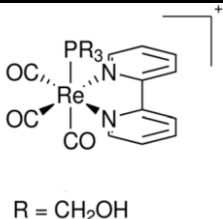
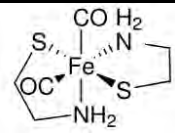
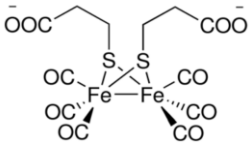
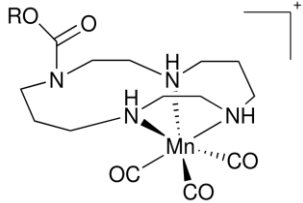
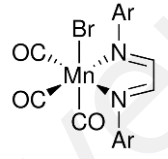
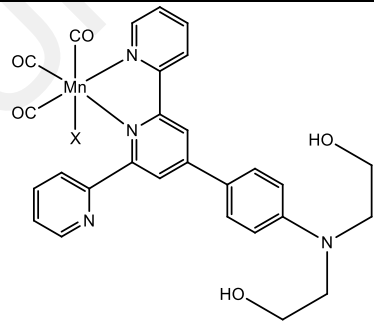
PhotoCORMs	Half-life, activation wavelength	Biological properties
	$t_{1/2} = 24$ mins, UV (365 nm)	As a potential CORM peptide nucleic acids (PNA) bioconjugates (Bischof et al., 2013).
 <p>R = CH₂OH</p>	$t_{1/2} = 24$ mins, UV (<400 nm)	Displayed low cytotoxicity against human prostatic carcinoma PPC-1 and the compound displayed luminescence properties in cells as an <i>in vitro</i> marker (Pierri et al., 2012).
	$t_{1/2} = \text{n.d.},$ Visible (>400 nm)	Photo-activation of the CO-dependent BK type human ion channel (Kretschmer et al., 2011).

Table 2.3, Continued.

PhotoCORMs	Half-life, activation wavelength	Biological properties
	$t_{1/2} = \text{n.d.},$ Visible ($>400 \text{ nm}$)	Displayed minimum cytotoxicity against normal mammary epithelial cells (MCF- 10A) (Poh et al., 2014).
 <p>R = Cyanocobalamin derivatives</p>	$t_{1/2} = \text{n.d.},$ Visible (470 nm)	Promoted cytoprotective effects on 3T3 fibroblasts upon visible light illumination (Zobi et al., 2013).
 <p>Ar = 2,6-(<i>i</i>Pr)₂C₆H₃</p>	$t_{1/2} = \sim 35$ mins, Visible (560 nm) (Mansour, 2017)	n.d.
 <p>X = F₃CO₂SO</p>	$t_{1/2} = \text{n.d.},$ near-infrared (800 nm) (Nagel et al., 2014)	n.d.

*n.d. indicates that the study was not conducted. Mins = minutes, Secs = seconds

2.4 Schiff base ligands and its photoCORMs.

Schiff bases (*N*-substituted imine) are compounds consist of azomethine functional group, -RHC=N-R' (where R and R' \neq H), as a result of condensation reaction between primary amine and carbonyl (aldehydes and ketones) compounds (Cordes & Jencks, 1962). It was first developed by a German chemist, Hugo Schiff, in 1864, since then Schiff bases have been widely used as synthetic intermediate in organic and inorganic (coordination) chemistry (Tidwell, 2008). Besides, Schiff base compounds containing fluorene, 2-hydroxynaphthalene, and 2-hydroxy-3-methoxybenzene as part of the structures are known to have anticancer and antimicrobial properties (Bahron et al., 2019; Cheng et al., 2009; Hussein et al., 2021; Ishak et al., 2019; Rodríguez et al., 2019; Sari et al., 2021; Wang et al., 2020).

Schiff base synthesis allows scientist to create new ligands with high double bond conjugations and this property is especially useful for the development of photoCORMs as it grants the photo-activation properties for the photoCORMs (Chakraborty et al., 2014). Besides that, Schiff base ligand also confer potential therapeutic properties to the synthesized photoCORMs such as antimicrobial and anticancer properties. The example of Schiff base photoCORMs and their biological properties are shown in Table 2.4.

Table 2.4: PhotoCORMs containing Schiff base ligand and potential biological properties.

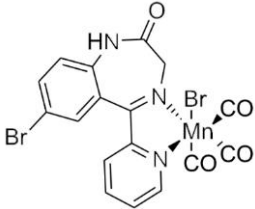
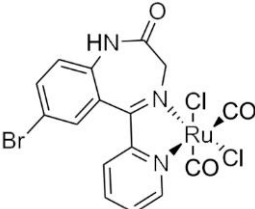
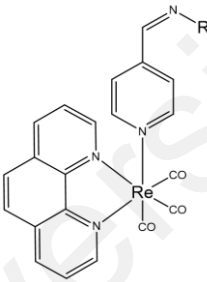
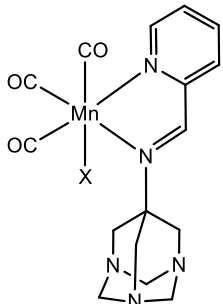
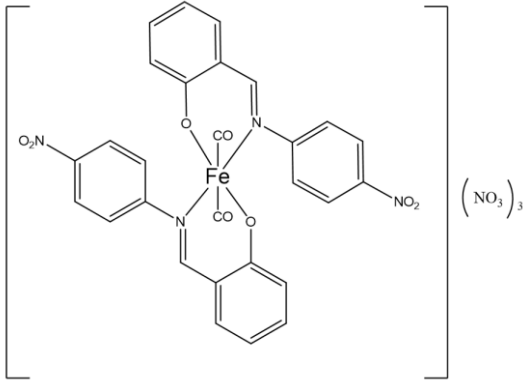
Schiff base PhotoCORMs	Biological properties
	<p>Displayed antimicrobial activity against Gram positive and negative bacteria (Mansour, 2017).</p>
	<p>Displayed antimicrobial activity against Gram positive and negative bacteria (Mansour, 2017).</p>
 <p>R = Carboxymethyl Chitosan (CMC)</p>	<p>Displayed significant photo-induced cytotoxicity against human colorectal adenocarcinoma, HT-29 cell lines (Chakraborty et al., 2017).</p>
	<p>Potential cellular internalization due to the water solubility which may improves the cytotoxicity against malignant cells (Jimenez et al., 2016).</p>

Table 2.4, Continued.

Schiff base PhotoCORMs	Biological properties
	<p>Displayed profound antibacterial properties and cytotoxicity against breast cancer cell line, MCF-7 (Kupwade & Sawant, 2020).</p>

CHAPTER 3: METHODOLOGY

3.1 Materials and solutions

All photoCORMs were synthesized by using standard Schlenk line techniques in the absence of light under purified argon gas and were chromatographed in vacuum atmosphere Dribox. Solvents used for photoCORMs synthesis and chromatography were distilled using sodium/benzophenone prior to usage. Silica gel (Merck Kieselgel 60, 230–400 mesh) and Celite (Fluka AG) were heated and activated at 140 °C for 24 hours before chromatographic use. The chemicals for synthesis (1,10-phenanthroline-5-amine, fluorene-2-carboxaldehyde, 2-hydroxy-1-naphthaldehyde, 2-hydroxy-3-methoxy benzaldehyde, terephthalaldehyde, chromium hexacarbonyl, molybdenum hexacarbonyl, tungsten hexacarbonyl, and trimethylamine-*N*-oxide dihydrate (TMNO)) were purchased from Sigma-Aldrich, Germany and Alfa Aesar, England. Myoglobin assays were performed using the myoglobin extracted from equine skeletal muscle (95–100%) purchased from Sigma, Germany. The reagents for antimicrobial and MTT cytotoxic assays were purchased from Sigma-Aldrich (St. Louis, MO, USA), including accutase, cell culture media, cisplatin, DMSO, fetal bovine serum (FBS), phosphate-buffered saline (PBS), trypan blue solution, and 3-(4,5-dimethylthiazol-2-yl)-2,5-diphenyltetrazolium bromide (MTT). The human-derived colorectal adenocarcinoma HT-29 (ATCC[®] HTB-38[™]), colorectal carcinoma HCT 116 (ATCC[®] CCL-247[™]), and normal colon fibroblast CCD-18Co (ATCC[®] CRL-1459[™]) cell lines were purchased from American Type Culture Collection (ATCC, USA).

3.2 Physical measurements

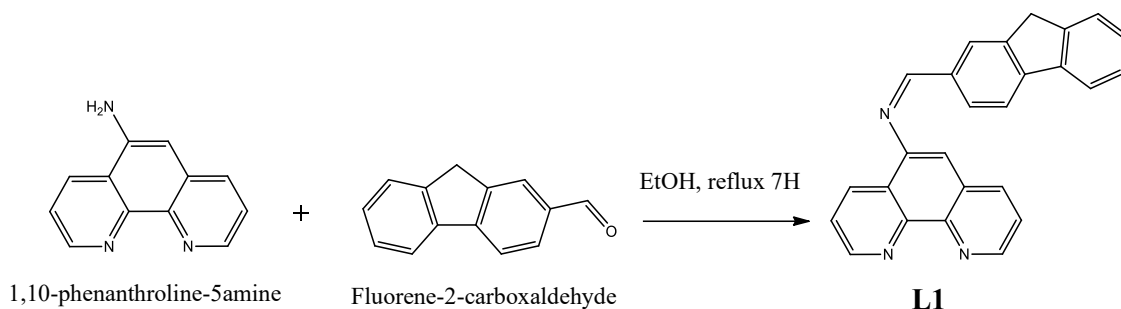
The IR spectra of all compounds were recorded in the range of 4000 – 450 cm^{-1} on a PerkinElmer Spectrum RX-1 spectrometer. ^1H and ^{13}C -NMR (proton decoupled) spectra of all compounds were determined using a Bruker Avance III 400 Spectrometer. Electronic absorption spectra of all compounds were studied using a Shimadzu UV-2600 spectrophotometer. The percentage of carbon, hydrogen, and nitrogen of all compounds were determined on a Thermo Finnigan Eager 300 CHN elemental analyser. The crystal structures of 12 compounds were acquired on a Rigaku Oxford (formerly Agilent Technologies) Super Nova Dual diffractometer.

3.3 Syntheses

3.3.1 Synthesis of Schiff base ligands

Synthesis of (((1,10-phenanthroline-5-yl)imino)methyl)N-(2-fluorenylmethylene) (L1)

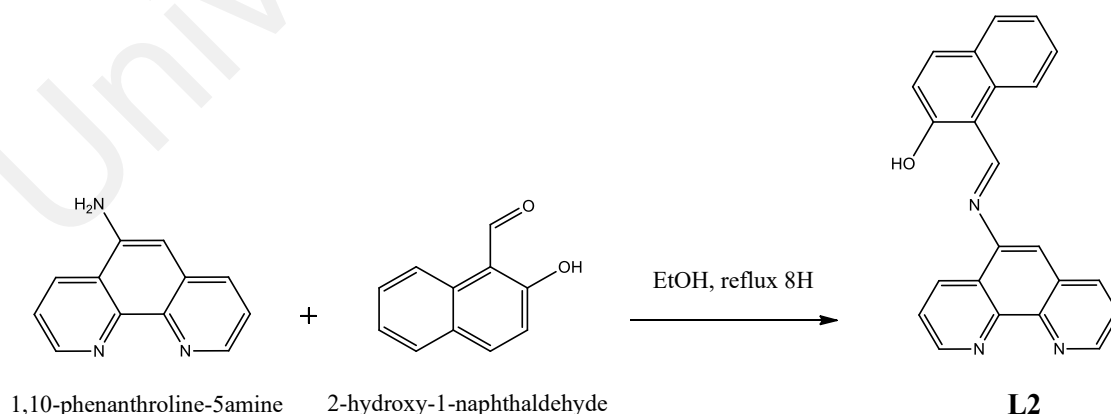
L1 was prepared by refluxing 1,10-phenanthroline-5-amine (0.3904 g, 2 mmol) and fluorene-2-carboxaldehyde (0.3885 g, 2 mmol) in absolute ethanol for 7 hours and the reaction mechanism is shown in Scheme 3.1. The yellow-colored solution formed was filtered and cooled to obtain fine yellow crystals. The crystals were then filtered and recrystallized from methanol. Yield: 0.5749 g, 77.4 %. M.P.: 177-180 °C. Anal. Calc. for $\text{C}_{26}\text{H}_{17}\text{N}_3$: C, 84.07; H, 4.61; N, 11.31%. Found: C, 84.42; H, 4.19; N, 11.23%.



Scheme 3.1: Schematic representation of the formation of L1.

Synthesis of (((1,10-phenanthroline-5-yl)imino)methyl)naphthalen-2-ol (L2)

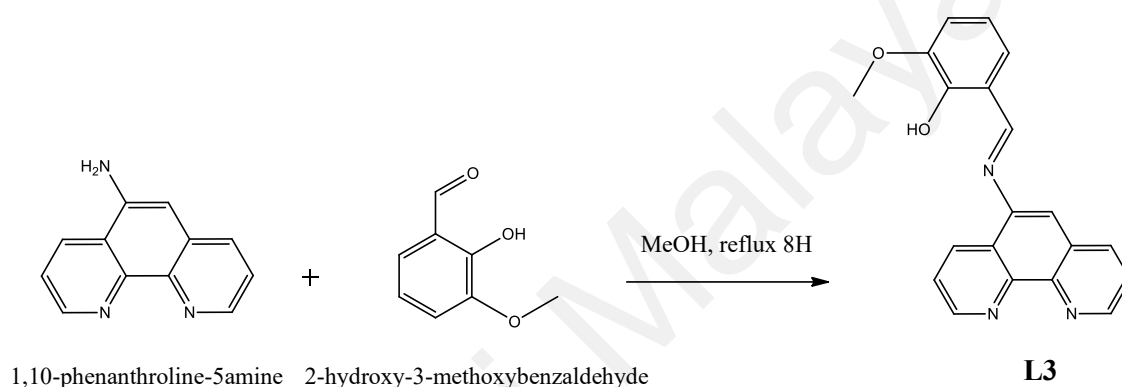
The preparation of **L2** was based on previously reported method by refluxing 1,10-phenanthroline-5-amine (0.3904 g, 2 mmol) and 2-hydroxy-1-naphthaldehyde (0.3444 g, 2 mmol) in absolute ethanol for 8 hours and the reaction mechanism is shown in Scheme 3.2 (Alreja & Kaur, 2019). The brown-colored solution formed were filtered and cooled to obtain brown precipitates. The precipitates were dissolved and crystallized in acetone upon slow evaporation to obtain orange-colored crystals. Yield: 0.4015 g, 57.5%. M.P.: 185-189 °C. Anal. Calc. for $\text{C}_{23}\text{H}_{15}\text{N}_3\text{O}$: C, 79.07; H, 4.33; N, 12.03%. Found: C, 79.33; H, 4.71; N, 12.39%.



Scheme 3.2: Schematic representation of the formation of L2.

Synthesis of (((1,10-phenanthroline-5-yl)imino)methyl)-6-methoxyphenol (L3)

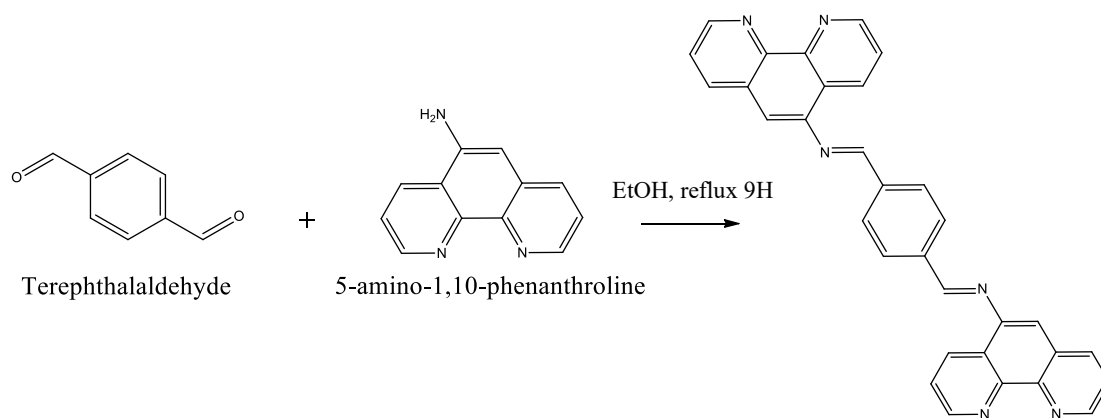
L3 was prepared by refluxing 1,10-phenanthroline-5-amine (0.3904 g, 2 mmol) and 2-hydroxy-3-methoxybenzaldehyde (0.3034 g, 2 mmol) in 15 mL of methanol for 7 hours and the reaction mechanism is shown in Scheme 3.3. The orange-colored solution was filtered and cooled to obtain fine orange needle-like crystals. The crystals were filtered and recrystallized in methanol. Yield: 0.4713 g, 68.7%. M.P.: 162-163 °C. Anal. Calc. for $C_{20}H_{15}N_3O_2$: C, 72.94; H, 4.59; N, 12.76%. Found: C, 72.57; H, 4.83; N, 12.63%.



Scheme 3.3: Schematic representation of the formation of L3.

Synthesis of bis(((1,10-phenanthroline-5-yl)imino)-1,4-phenylene (L4)

L4 was prepared by refluxing 1,10-phenanthroline-5-amine (0.8589 g, 4.4 mmol) and terephthalaldehyde (0.2682 g, 2 mmol) in 20 mL of ethanol for 9 hours and the reaction mechanism is shown in Scheme 3.4. The yellow-colored solution formed was filtered and cooled to obtain fine yellow powder. The powder was filtered and redissolved in ethanol and yellow-colored crystals were formed upon slow evaporation. Yield: 0.6213 g, 63.6%. M.P.: 189-192 °C. Anal. Calc. for $C_{32}H_{20}N_6$: C, 78.67; H, 4.13; N, 17.20%. Found: C, 78.95; H, 4.57; N, 17.55%.



Scheme 3.4: Schematic representation of the formation of L4.

3.3.2 Synthesis of photoCORMs

Synthesis of (L1)Cr(CO)₄ (C1)

C1 was prepared based on the previously described method (Hor, 1987). Trimethylamine-*N*-oxide dihydrate (TMNO) (0.244 g, 2.2 mmol) and chromium hexacarbonyl (0.2200 g, 1 mmol) were added to 15 ml of toluene in a Schlenk flask and stirred for 15 minutes until the solution turned yellow, followed by the addition of **L1** (0.2973 g, 0.8 mmol) and the solution was stirred for 18 hours in the absence of light to obtain a mixture with purplish-red precipitate. The reaction mechanism is shown in Scheme 3.5. The precipitate was collected and chromatographed in THF and toluene mixture in a ratio of 1:1 to obtain a purplish-red solution. Red needle-like crystals were formed upon cooling the solution. Yield: 0.2212 g, 51.6 %. D.P.: 192 °C. Anal. Calc. for C₃₀H₁₇N₃O₄Cr: C, 67.29; H, 3.20; N, 7.85%. Found: C, 67.74; H, 3.56; N, 8.24%.

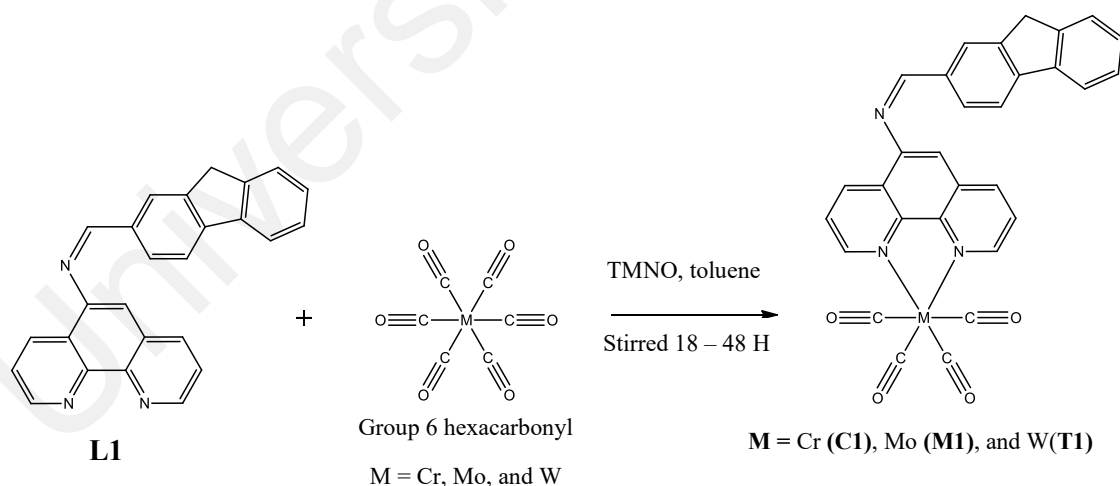
Synthesis of (L1)Mo(CO)₄ (M1)

The synthesis of **M1** was similar to **C1** by using molybdenum hexacarbonyl (0.2640 g, 1 mmol). The mixture was stirred for 24 hours to obtain a mixture with dark red

precipitate. The precipitate was collected and chromatographed in THF and toluene mixture in a ratio of 1:1 to obtain a red-colored solution. Red needle-like crystals were formed upon vacuum drying the solution. Yield: 0.1961 g, 42.3 %. D.P.: 211 °C. Anal. Calc. for $C_{30}H_{17}N_3O_4Mo$: C, 62.19; H, 2.96; N, 7.25%. Found: C, 62.51; H, 3.43; N, 7.59%.

Synthesis of (L1)W(CO)₄ (T1)

The synthesis of **T1** was similar to **C1** by using tungsten hexacarbonyl (0.3519 g, 1 mmol). The mixture was stirred for 48 hours to obtain a mixture with dark red precipitate. The precipitate was collected and chromatographed in THF and toluene mixture in a ratio of 1:1 to obtain a red-colored solution. Red needle-like crystals were formed upon vacuum drying the solution. Yield: 0.2742 g, 51.3 %. D.P.: 224 °C. Anal. Calc. for $C_{30}H_{17}N_3O_4W$: C, 54.00; H, 2.57; N, 6.30%. Found: C, 54.53; H, 2.89; N, 6.72%.



Scheme 3.5: Schematic representation of the synthesis of C1, M1, and T1.

Synthesis of (L2)Cr(CO)₄ (C2)

C2 was prepared based on the previously described method (Hor, 1987). TMNO (0.244 g, 2.2 mmol) and chromium hexacarbonyl (0.2200 g, 1 mmol) were added to 15 ml of toluene in a Schlenk flask and stirred for 15 minutes until the solution turned yellow, followed by the addition of **L2** (0.2792 g, 0.8 mmol) and the solution was stirred for 18 hours in the absence of light to obtain a mixture with orange-red precipitate. The reaction mechanism is shown in Scheme 3.6. The precipitate was collected and chromatographed in THF and toluene mixture in a ratio of 1:1 to obtain an orange-red solution. Orange-red colour rod-shaped crystals were formed upon cooling the solution. Yield: 0.1933 g, 47.1%. D.P.: 182 °C. Anal. Calc. for C₂₇H₁₅CrN₃O₅: C, 63.16; H, 2.94; N, 8.18%. Found: C, 63.57; H, 3.06 N, 8.33%

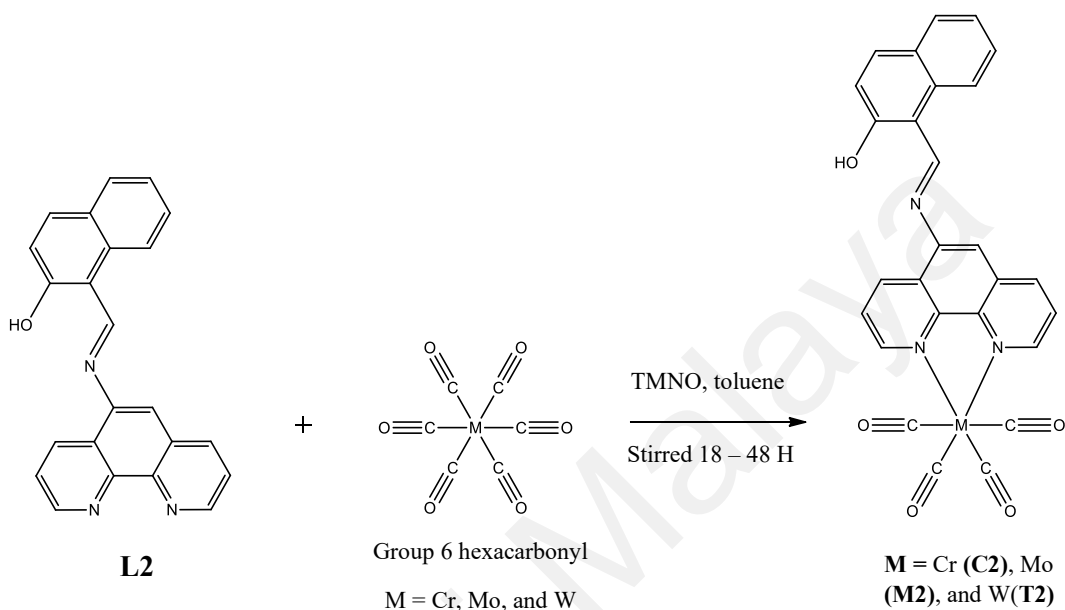
Synthesis of (L2)Mo(CO)₄ (M2)

The synthesis of **M2** was similar to **C2** by using molybdenum hexacarbonyl (0.2640 g, 1 mmol). The mixture was stirred for 24 hours to obtain a mixture with orange-colored precipitate. The precipitate was collected and chromatographed in THF and toluene mixture in a ratio of 1:1 to obtain a red-colored solution. Red colour rod-shaped crystals were formed upon cooling the solution. Yield: 0.2209 g, 49.4%. D.P.: 189 °C. Anal. Calc. for C₂₇H₁₅MoN₃O₅: C, 58.18; H, 2.71; N, 7.54%. Found: C, 58.02; H, 3.12 N, 7.86%.

Synthesis of (L2)W(CO)₄ (T2)

The synthesis of **T2** was similar to **C2** by using tungsten hexacarbonyl (0.3519 g, 1 mmol). The mixture was stirred for 48 hours to obtain a mixture with orange-colored precipitate. The precipitate was collected and chromatographed in THF and toluene

mixture in a ratio of 1:1 to obtain a dark orange-colored solution. Dark orange-colored rod-shaped crystals were formed upon cooling the solution. Yield: 0.2668 g, 51.6%. D.P.: 197 °C. Anal. Calc. for $C_{27}H_{15}WN_3O_5$: C, 50.26; H, 2.34; N, 6.51%. Found: C, 50.58; H, 2.74 N, 6.83%.



Scheme 3.6: Schematic representation of the synthesis of C2, M2, and T2.

Synthesis of (L3)Cr(CO)₄ (C3)

C3 was prepared based on the previously described method (Hor, 1987). TMNO (0.244 g, 2.2 mmol) and chromium hexacarbonyl (0.2200 g, 1 mmol) were added to 15 ml of toluene in a Schlenk flask and stirred for 15 minutes until the solution turned yellow, followed by the addition of **L3** (0.2633 g, 0.8 mmol) and the solution was stirred for 18 hours in the absence of light to obtain a mixture with orange-red precipitate. The reaction mechanism is shown in Scheme 3.7. The precipitate was collected and chromatographed in THF and toluene mixture in a ratio of 1:1 to obtain an orange-red solution. Fine needle-like orange-colored crystals were formed upon vacuum drying the solution. Yield: 0.1912

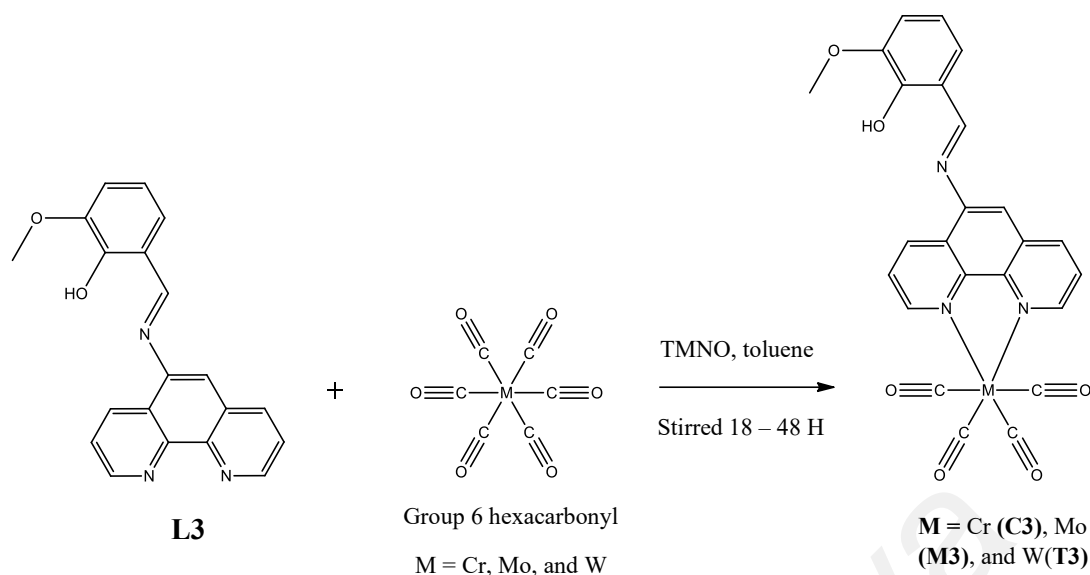
g, 48.5 %. D.P.: 185 °C. Anal. Calc. for $C_{24}H_{15}CrN_3O_6$: C, 58.42; H, 3.06; N, 8.52. Found: C, 58.81; H, 3.42; N, 8.87%.

Synthesis of (L3)Mo(CO)₄ (M3)

The synthesis of **M3** was similar to **C3** by using molybdenum hexacarbonyl (0.2640 g, 1 mmol). The reaction mixture was stirred for 24 hours in the dark to obtain a mixture with bright-red precipitates. The precipitate was filtered and chromatographed using THF and toluene solution mixture with the ratio of 1:1 to obtain a bright-red solution. Dark orange-colored needle-like crystals were obtained upon vacuum drying the solution. Yield: 0.2134 g, 49.4 %. D.P.: 196 °C. Anal. Calc. for $C_{24}H_{15}MoN_3O_6$: C, 53.64; H, 2.81; N, 7.82. Found: C, 54.02; H, 3.26; N, 7.92%.

Synthesis of (L3)W(CO)₄ (T3)

The synthesis of **T1** was similar to **C1** by reacting with tungsten hexacarbonyl (0.3519 g, 1 mmol). The reaction mixture was stirred for 48 hours in the dark to obtain a mixture with red precipitates. The precipitate was filtered and chromatographed using THF and toluene solution mixture with the ratio of 1:1 to obtain a bright-red solution. Light orange-colored fine needle-like crystals were obtained upon vacuum drying the solution. Yield: 0.2872 g, 55.6 %. D.P.: 201 °C. Anal. Calc. for $C_{24}H_{15}WN_3O_6$: C, 46.10; H, 2.42; N, 6.72. Found: C, 46.08; H, 2.76; N, 7.07%.



Scheme 3.7: Schematic representation of the synthesis of C3, M3, and T3.

Synthesis of (L4)Cr₂(CO)₈ (C4)

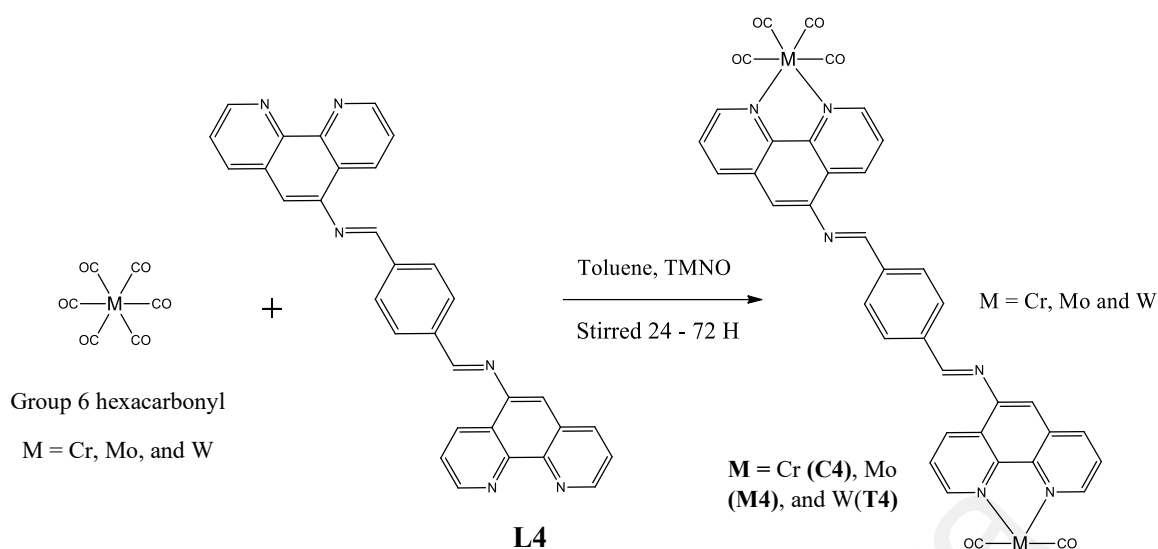
C4 was prepared based on the previously described method (Hor, 1987). TMNO (0.4884 g, 4.4 mmol) and chromium hexacarbonyl (0.4840 g, 2.0 mmol) were added to 15 ml of toluene in a Schlenk flask and stirred for 15 minutes until the solution turned yellow, followed by the addition of **L4** (0.3907 g, 0.8 mmol) and the solution was stirred for 24 hours in the absence of light to obtain a mixture with dark red precipitate. The reaction mechanism is shown in Scheme 3.8. The precipitate was collected and chromatographed in THF to obtain dark red solution. Fine red-colored crystals were formed upon vacuum drying the solution. Yield: 0.3134 g, 48.0 %. D.P.: 213 °C. Anal. Calc. for C₄₀H₂₀Cr₂N₆O₈: C, 58.83; H, 2.47; N, 10.29%. Found: C, 58.58; H, 2.72; N, 10.03%.

Synthesis of (L4)Mo₂(CO)₈ (M4)

The synthesis of **M4** was similar to **C4** by using molybdenum hexacarbonyl (0.5280 g, 2 mmol). The reaction mixture was stirred for 48 hours in the dark to obtain a mixture with bright-red precipitates. The precipitate was filtered and chromatographed using THF to obtain a bright-red solution. Dark, red-colored crystals were obtained upon vacuum drying the solution. Yield: 0.3723 g, 51.3 %. D.P: 226 °C. Anal. Calc. for C₄₀H₂₀Mo₂N₆O₈: C, 53.11; H, 2.23; N, 9.29. Found: C, 53.39; H, 2.16; N, 9.42%.

Synthesis of (L4)W₂(CO)₈ (T4)

The synthesis of **T4** was similar to **C4** by using molybdenum hexacarbonyl (0.7038 g, 2 mmol). The reaction mixture was stirred for 72 hours in the dark to obtain a mixture with reddish-brown precipitates. The precipitate was filtered and chromatographed using THF to obtain a reddish-brown solution. Reddish-brown fine crystals were obtained upon vacuum drying the solution. Yield: 0.4237 g, 49.1 %. D.P.: 232 °C Anal. Calc. for C₄₀H₂₀W₂N₆O₈: C, 44.47; H, 1.87; N, 7.78. Found: C, 44.83; H, 2.12; N, 7.92%.



Scheme 3.8: Schematic representation of the synthesis of bimetallic photoCORMs C4, M4, and T4.

3.4 Myoglobin assay

The half-life and amount of CO released from all photoCORMs were studied using a modified version of standard myoglobin (Mb) assay (Atkin et al., 2011). The assay was performed in the absence of light. The Mb stock solution (66 μM) (132 μM for **C4**, **M4**, and **T4**) was first prepared and the UV-Vis absorbance (500–600 nm) of the Mb solution was measured by adding 2 mL of the stock solution into a cuvette. The carboxymyoglobin (MbCO) absorbance was obtained by purging the 2 mL Mb solution with CO gas in the cuvette. To measure the half-life and CO released by the photoCORMs, a three-layered solution method was employed and depicted in Figure 3.1. Chloroform (0.5 ml) was added into a quartz cuvette and chloroform solution of the photoCORMs were added into the chloroform layer in the cuvette to produce concentrations of 20, 40, and 60 μM . The Mb stock solution prepared earlier was added immediately onto the chloroform layer. Few drops of vegetable oil were then added on top of the solution as an oxygen barrier to prevent oxygen from reacting with the myoglobin. The chloroform layer was illuminated

at the distance of 2 cm with UV light (365 nm) at constant intervals. The absorbance were measured and the rate and amount of CO released were determined by taking the absorbance at 540 nm. The cuvette was swirled lightly before each measurement to allow homogeneous Mb and MbCO mixture.

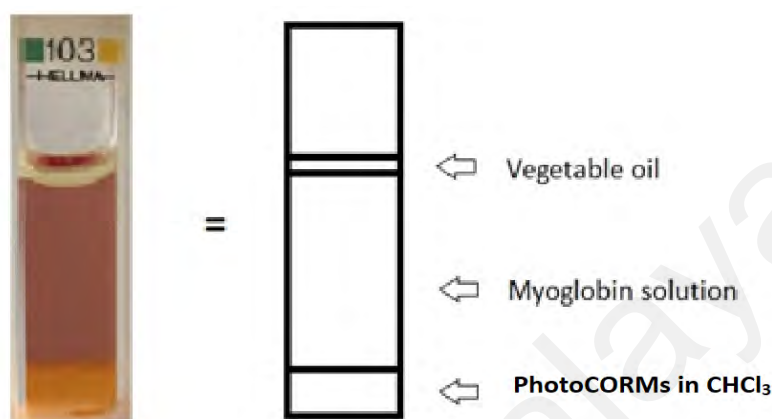


Figure 3.1: Three-layered myoglobin solution.

3.5 PhotoCORMs dark stability test

The stability of the photoCORMs in the absence of light in 10% DMSO-PBS buffer solution at 24 and 48 hours were determined using UV-Vis and ATR-IR based on previously described methods (Lakshman et al., 2019; Rimmer et al., 2010). The photoCORMs were first dissolved in 100 mL of 10% DMSO-PBS buffer to produce a concentration of 60 μ M and placed in a dark environment with temperature maintained at 37.5 °C. The initial UV-Vis absorbance was measured at 300 – 900 nm by adding 2 mL of the solution into a cuvette. The absorbance of the solution after 24 and 48 hours were then measured to determine the changes in the spectra. The IR spectrum of the solutions after 24 and 48 hours were also recorded on an ATR-IR by vacuum drying the solution at high temperature to obtain the residues.

3.6 Cytotoxicity evaluation

3.6.1 Cell culture

The human-derived colorectal adenocarcinoma HT-29 (ATCC[®] HTB-38[™]), colorectal carcinoma HCT 116 (ATCC[®] CCL-247[™]), and normal colon fibroblast CCD-18Co (ATCC[®] CRL-1459[™]) cell lines were used in the cytotoxicity study. Cells were cultured using McCoy's 5A Medium (HT-29 and HCT 116) or EMEM (CCD-18Co), supplemented with 10% FBS and incubated at 37 °C in a humidified CO₂ incubator. Cells were sub-cultured upon reaching 70–80% confluency and maintained at low-passage number with their morphology observed from time to time to avoid genetic drift.

3.6.2 MTT cytotoxicity assay

The growth inhibitory effect of all compounds against the HT-29, HCT 116, and CCD-18Co cell lines was tested using MTT cytotoxicity assay as described previously with slight modifications (Heng et al., 2020). In general, 4.5×10^3 (HT-29 and HCT 116) or 1.2×10^4 (CCD-18Co) cells per well were seeded into a 96-well microplate, incubated overnight, and treated with various concentrations (0–100 µM) of all compounds for 48 hours. Another set of experiment was conducted to determine the UV-triggered *in situ* CO release of the photoCORMs against the treated cell lines to examine the potential photo-induced cytotoxicity. The treated cells were illuminated with UV light (365 nm) using a UV hand lamp for 20 minutes prior to 48 hours of incubation. Cisplatin was used as the positive control. The MTT (5 mg/ml) was then added into each well and incubated for another 3 hours before the addition of DMSO. The absorbance of each well was measured using a Tecan M200 Infinite Pro microplate reader at 570 and 650 nm as reference wavelength. The IC₅₀ values were determined by plotting percentage of viability against the concentration of treatment on a logarithmic scale using a GraphPad

Prism 7 software (CA, USA). Selectivity index (SI) was calculated to determine the degree of selectivity of the compounds according to the Equation 3.1 (Desai et al., 2020a).

$$SI = IC_{50} \text{ in normal colon fibroblast} / IC_{50} \text{ in colorectal cancer cells}$$

Where $SI > 2$ indicates non-toxicity of a compound (Desai et al., 2020a). (3.1)

3.7 Antimicrobial study

The assay was conducted using 96-well microtiter plates according to the standard protocol suggested by the Clinical and Laboratory Standards Institute with slight modifications. All compounds were prepared in 10% DMSO in PBS solution in a dark environment. A series of bacteria and fungi were cultured for 24 hours in a Mueller-Hinton broth (MHB) and were adjusted to match the 0.5 McFarland Standard and diluted to 1:100 in MHB. All compounds were two-fold serially diluted with MHB across the microtiter plate to obtain final concentrations between 0.10 mg/mL and 0.39 μ g/mL. Prior to incubation at 37 °C for 24 hours, 100 μ L of 1:100 diluted cell suspension was added into each well. After the incubation, the well with the lowest concentration of tested compound that showed no observable growth is determined as the minimum inhibitory concentration (MIC). The content of clear wells was then smeared on a Mueller-Hinton Agar (MHA) and incubated overnight. The inoculum from the MHB containing the lowest concentration of tested compound that inhibited cell growth on the MHA was determined as the minimum bactericidal concentration (MBC). The experiment was performed in triplicate (Choo et al., 2018). Another set of experiment was conducted with similar procedure but each 96-well microtiter plates were illuminated with UV light (365nm) using a UV handlamp for 20 minutes prior to incubation.

CHAPTER 4: RESULTS AND DISCUSSION

4.1 Structural Elucidations

4.1.1 Infra-Red Spectroscopy

The selected IR stretching of the first, second, third, and fourth series compounds are shown in Table 4.1, Table 4.2, Table 4.3, and Table 4.4, respectively. All compounds showed aromatic and imine stretching peaks in the region of 2850 – 3100 and 1500 – 1620 cm^{-1} which correspond to the presence of aromatic rings (from phenanthroline, fluorene, 2-hydroxynaphthalene, 2-hydroxy-3-methoxybenzene, and diphenanthroline) and imine bonds present in the structures (Savir et al., 2020). All complexes also showed weak metal-to-nitrogen (M–N) bond stretching peaks in the region of 1000 – 1100 cm^{-1} which arise from the bondings between phenanthroline nitrogens and metal center (chromium, molybdenum, and tungsten).

The second and third series compounds (**L2**, **C2**, **M2**, **T2**, **L3**, **C3**, **M3**, and **T3**) showed prominent phenolic–OH (Ph–OH) stretching peaks (broad peaks) in the region of 3100 – 3450 cm^{-1} . This is due to the presence of hydroxyl group in the naphthalene structure for second series compounds (**L2**, **C2**, **M2**, and **T2**) and benzene group for third series compounds (**L3**, **C3**, **M3**, and **T3**). Besides, third series compounds also showed prominent ether (O–CH₃) stretching peaks in the region of 1200 – 1300 cm^{-1} which can be attributed to the presence of 3-methoxy group in the benzene ring which bonded to the phenanthroline group through the imine bond.

The complexes (photoCORMs) from all four series displayed significant carbon monoxide (carbonyl, C≡O) stretching peaks in the region of 1800 – 2050 cm^{-1} . The first and third series photoCORMs (**C1**, **M1**, **T1**, **C2**, **M2**, and **T2**) showed four prominent

carbonyl peaks which correspond to the four non-equivalent $\text{C}\equiv\text{O}$ bonded to the metal center (Cr, Mo, and W) arranged in octahedral geometry. However, second and fourth series photoCORMs (**C2**, **M2**, **T2**, **M4**, and **T4**) showed only three carbonyl stretching peaks due to the overlapping of two carbonyl peaks near 1850 cm^{-1} which suggest that two of the carbonyls are equivalent to each other with similar stretching frequencies.

Table 4.1: Selected infrared frequencies for L1, C1, M1, and T1.

Compound	Imine, $\text{C}=\text{N}$ (cm^{-1})	Aromatic, $\text{C}-\text{H}$ (cm^{-1})	Carbonyl, $\text{C}\equiv\text{O}$ (cm^{-1})	Metal, $\text{M}-\text{N}$ (cm^{-1})
L1	1562	3026	-	-
C1	1587	2920	1998, 1872, 1865, 1811	1045
M1	1590	2914	2008, 1866, 1854, 1821	1047
T1	1588	2913	2001, 1879, 1869, 1813	1049

Table 4.2: Selected infrared frequencies for L2, C2, M2, and T2.

Compound	Imine, $\text{C}=\text{N}$ (cm^{-1})	Aromatic, $\text{C}-\text{H}$ (cm^{-1})	Phenolic, $\text{Ph}-\text{OH}$ (cm^{-1})	Carbonyl, $\text{C}\equiv\text{O}$ (cm^{-1})	Metal, $\text{M}-\text{N}$ (cm^{-1})
L2	1573	3050, 3027	3313	-	-
C2	1600	3061, 2931	3344	2001, 1861, 1822	1035
M2	1603	3063, 2919	3292	2009, 1856, 1817	1073
T2	1603	2973, 2868	3050	2000, 1845, 1812	1093

Table 4.3: Selected infrared frequencies for L3, C3, M3, and T3.

Compound	Imine, C=N (cm ⁻¹)	Aromatic, C-H, (cm ⁻¹)	Phenolic, Ph-Oh (cm ⁻¹)	Ether, O-CH ₃ (cm ⁻¹)	Carbonyl, C≡O (cm ⁻¹)	Metal, M-N (cm ⁻¹)
L3	1611	3052, 2907	3481	1245	-	
C3	1590	3060, 2946	3409	1247	2003, 1879, 1865, 1810	1069
M3	1607	3067, 2972	3413	1250	2002, 1880, 1861, 1818	1083
T3	1608	3077, 2973	3421	1252	1995, 1869, 1853, 1813	1085

Table 4.4: Selected infrared frequencies for L4, C4, M4, and T4.

Compound	Imine, C=N (cm ⁻¹)	Aromatic, C-H (cm ⁻¹)	Carbonyl, C≡O (cm ⁻¹)	Metal, M-N (cm ⁻¹)
L4	1595	3010, 2972	-	-
C4	1592	2981, 2883	2002, 1888, 1835, 1809	1068
M4	1590	3056, 2972	2008, 1895, 1828	1046
T4	1588	3071, 2980	1999, 1842, 1801	1036

4.1.2 ^1H -NMR Spectroscopy

The ^1H -NMR shifting of first, second, third, and fourth series compounds are shown in Table 4.5, Table 4.6, Table 4.7, and Table 4.8, respectively. All compounds showed aromatic hydrogen shifting peaks (one proton) in 9.70 – 6.90 ppm (singlets and doublets) which can be attributed to the aromatic hydrogens present in the phenanthrolines, fluorene, 2-hydroxynaphthalene, and 2-hydroxy-3-methoxybenzene. Other than that, all compounds also displayed imine hydrogen shifting peak in 8.90 – 8.00 ppm due to the presence of imine bond in the ligands' structures. However, the aromatic and imine hydrogen shifting for fourth series compounds (**L4**, **C4**, **M4**, and **T4**) are in two protons equivalent due to the C_2 symmetrical nature of the compounds. In general, the ^1H -NMR of the complexes (photoCORMs) showed downfield shifting as compared to the ligands due to the deshielding effect imposed by the metal center (Kleinpeter et al., 2007).

The phenolic OH (Ph–OH) shifting were observed in second and third series compounds **L2**, **C2**, **M2**, **T2**, **L3**, **C3**, **M3**, and **T3** in the region of 13.50 – 10.00 ppm due to the presence of hydroxyl (OH) group in the naphthalene for second series compounds (**L2**, **C2**, **M2**, and **T2**) and benzene for third series compounds (**L3**, **C3**, **M3**, and **T3**). Besides, the first series compounds (**L1**, **C1**, **M1**, and **T1**) showed fluorene-CH₂ proton shifting (two protons) in the region of 4.10 – 3.90 ppm due to the presence of sp³ hybridized carbon in the fluorene structure and the protons are highly deshielded because the carbon is directly bonded to two aromatic rings. Other than that, the third series compounds (**L3**, **C3**, **M3**, and **T3**) also displayed ether (O–CH₃) proton shifting in the region of 4.00 – 3.00 ppm due to the presence of methoxy group in the benzene ring (Contreras et al., 1993).

Table 4.5: ^1H -NMR shifting of L1, C1, M1, and T1.

Compound	HC=N (δ , ppm)	Aromatic (δ , ppm)	Fluorene- CH ₂ (δ , ppm)
L1	8.22 (s, 1H)	9.19 (s, 1H), 9.08 (s, 1H), 8.79 (d, 1H, J = 8.04), 8.69 (s, 1H), 8.18 (d, 1H, J = 7.84 Hz), 7.95 (d, 1H, J = 8.42 Hz), 7.89 (d, 1H, J = 8.17 Hz), 7.84 (d, 1H, J = 7.12 Hz), 7.63 (d, 1H, J = 3.64 Hz), 7.56 (s, 2H), 7.39 (s, 1H), 7.37 (d, 1H, J = 5.36 Hz), 7.22 (s, 1H).	3.98 (s, 2H)
C1	8.75 (s, 1H)	9.60 (d, 1H, J = 3.72 Hz), 9.48 (d, 1H, J = 3.64 Hz), 8.87 (d, 1H, J = 7.36 Hz), 8.30 (s, 2H), 8.04 (d, 1H, J = 6.56 Hz), 7.97 (d, 1H, J = 7.16 Hz), 7.92 (d, 1H, J = 7.12 Hz), 7.83 (d, 1H, J = 7.04 Hz), 7.74 (s, 1H), 7.68 (s, 1H), 7.65 (d, 1H, J = 7.48 Hz), 7.47 (d, 1H, J = 10.96 Hz), 7.41 (s, 1H).	4.06 (s, 2H)

Table 4.5, Continued.

Compound	HC=N (δ , ppm)	Aromatic (δ , ppm)	Fluorene- CH ₂ (δ , ppm)
M1	8.77 (s, 1H)	9.51 (s, 1H), 9.40 (d, 1H, $J = 3.84$ Hz), 8.97 (d, 1H, $J = 8.00$ Hz), 8.77 (s, 1H, HC=N), 8.39 (d, 1H, $J = 7.64$ Hz), 8.31 (s, 1H), 8.07 (d, 1H, $J = 8.2$ Hz), 7.98 (d, 1H, $J = 7.36$ Hz), 7.91 (s, 1H), 7.82 (d, 1H, $J = 7.36$ Hz), 7.79 (d, 1H, $J = 7.76$ Hz), 7.75 (s, 1H), 7.63 (s, 1H), 7.45 (s, 1H).	4.05 (s, 2H)
T1	8.78 (s, 1H)	9.64 (d, 1H, $J = 4.52$ Hz), 9.52 (d, 1H, J $= 4.60$ Hz), 8.99 (d, 1H, $J = 8.00$ Hz), 8.42 (d, 1H, $J = 7.92$ Hz), 8.31 (s, 1H), 8.06 (d, 1H, $J = 7.96$ Hz), 7.98 (d, 1H, J $= 7.80$ Hz), 7.93 (d, 1H, $J = 7.36$ Hz), 7.80 (s, 1H), 7.79 (d, 1H, $J = 2.96$ Hz), 7.73 (d, 1H, $J = 2.92$ Hz), 7.48 (s, 1H), 7.45 (d, 1H, $J = 7.76$ Hz).	4.06 (s, 2H)

Table 4.6: ^1H -NMR shifting of L2, C2, M2, and T2.

Compound	HC=N (δ , ppm)	Aromatic (δ , ppm)	Ph-OH (δ , ppm)
L2	8.24 (s, 1H)	9.65 (s, 1H), 9.21 (s, 1H), 9.12 (s, 1H), 8.70 (d, 1H, $J = 8.20$ Hz), 8.20 (d, 1H, $J = 8.28$ Hz), 7.89 (d, 1H, $J = 9.04$ Hz), 7.77 (d, 1H, $J = 8.04$ Hz), 7.68 (d, 1H, $J = 8.08$ Hz), 7.62 (s, 1H), 7.60 (s, 1H), 7.55 (s, 1H), 7.50 (s, 1H), 7.38 (s, 1H).	10.02 (s, 1H)
C2	8.23 (s, 1H)	9.85 (s, 1H), 9.48 (d, 1H, $J = 5.2$ Hz), 9.34 (d, 1H, $J = 4.4$ Hz), 8.92 (d, 1H, $J = 8.72$ Hz), 8.87 (s, 1H), 8.73 (d, 1H, $J = 8.16$ Hz), 8.68 (s, 1H), 8.04 (d, 1H, $J = 4.92$ Hz), 7.98 (s, 1H), 7.95 (d, 1H, $J = 5.08$ Hz), 7.82 (d, 1H, $J = 8.12$ Hz), 7.72 (s, 1H), 7.61 (s, 1H).	10.48 (s, 1H)
M2	8.36 (s, 1H)	9.99 (s, 1H), 9.48 (d, 1H, $J = 4.28$ Hz), 9.35 (d, 1H, $J = 4.52$ Hz), 8.95 (d, 1H, $J = 8.12$ Hz), 8.81 (d, 1H, $J = 7.88$ Hz), 8.36 (s, 1H), 8.16 (d, 1H, $J = 8.48$ Hz), 8.04 (s, 1H), 8.01 (d, 1H, $J = 5.08$ Hz), 7.96 (d, 1H, $J = 7.56$ Hz), 7.91 (s, 1H), 7.75 (s, 1H), 7.55 (s, 1H).	10.77 (s, 1H)

Table 4.6, Continued.

Compound	HC=N (δ , ppm)	Aromatic (δ , ppm)	Ph-OH (δ , ppm)
T2	8.33 (s, 1H)	9.99 (s, 1H), 9.59 (s, 1H), 9.44 (d, 1H, J = 4.36 Hz), 9.02 (d, 1H, J = 8.68 Hz), 8.98 (s, 1H), 8.84 (d, 1H, J = 8.20 Hz), 8.79 (s, 1H), 8.14 (d, 1H, J = 4.92 Hz), 8.08 (s, 1H), 8.05 (d, 1H, J = 5.08 Hz), 8.03 (d, 1H, J = 5.24 Hz), 7.92 (d, 1H, J = 8.12 Hz), 7.76 (s, 1H).	10.59 (s, 1H)

Table 4.7: ¹H-NMR shifting of L3, C3, M3, and T3.

Compound	HC=N (δ, ppm)	Aromatic (δ, ppm)	Ph-OH (δ, ppm)	O-CH ₃ (δ, ppm)
L3	8.86 (s, 1H)	9.25 (s, 1H), 9.16 (s, 1H), 8.69 (d, 1H, <i>J</i> = 8.08 Hz), 8.26 (d, 1H, <i>J</i> = 7.72 Hz), 7.69 (d, 1H, <i>J</i> = 3.36 Hz), 7.64 (s, 1H), 7.46 (s, 1H), 7.26 (s, 1H), 7.14 (d, 1H, <i>J</i> = 7.44 Hz), 7.09 (d, 1H, <i>J</i> = 7.60 Hz), 6.99 (d, 1H, <i>J</i> = 7.76 Hz), 6.95 (s, 1H).	13.34 (s, 1H)	3.08 (s, 3H)
C3	8.89 (s, 1H)	9.54 (d, 1H, <i>J</i> = 4.80 Hz), 9.43 (d, 1H, <i>J</i> = 4.72 Hz), 8.81 (d, 1H, <i>J</i> = 8.36 Hz), 8.44 (d, 1H, <i>J</i> = 8.16 Hz), 7.78 (d, 1H, <i>J</i> = 8.16 Hz), 7.61 (s, 1H), 7.58 (s, 1H), 7.48 (d, 1H, <i>J</i> = 7.64 Hz), 7.16 (s, 1H), 7.11 (s, 1H).	12.84 (s, 1H)	3.99 (s, 3H)

Table 4.7, Continued.

Compound	HC=N (δ , ppm)	Aromatic (δ , ppm)	Ph-OH (δ , ppm)	O-CH ₃ (δ , ppm)
M3	8.82 (s, 1H)	9.47 (d, 1H, $J = 4.08$ Hz), 9.37 (d, 1H, $J = 4.24$ Hz), 8.73 (d, 1H, $J = 9.00$ Hz), 8.35 (d, 1H, $J = 7.64$ Hz), 7.71 (d, 1H, $J = 3.36$ Hz), 7.19 (d, 1H, $J = 9.6$ Hz), 7.09 (d, 1H, $J = 7.12$ Hz), 7.05 (s, 1H), 6.97 (d, 1H, $J = 7.92$ Hz), 6.92 (s, 1H).	12.84 (s, 1H)	3.93 (s, 3H)
T3	8.91 (s, 1H)	9.67 (d, 1H, $J = 4.88$ Hz), 9.57 (d, 1H, $J = 4.76$ Hz), 8.84 (d, 1H, $J = 8.36$ Hz), 8.45 (d, 1H, $J = 8.12$ Hz), 7.83 (d, 1H, $J = 7.24$ Hz), 7.79 (s, 1H), 7.77 (d, 1H, $J =$ 2.94 Hz), 7.62 (d, 1H, $J =$ 7.20 Hz), 7.49 (d, 1H, $J =$ 7.64 Hz), 7.19 (s, 1H).	12.87 (s, 1H)	4.01 (s, 3H)

Table 4.8: ^1H -NMR shifting of L4, C4, M4, and T4.

Compound	HC=N (δ , ppm)	Aromatic (δ , ppm)
L4	8.84 (s, 2H)	9.28 (d, 1H, $J = 8.08$ Hz), 9.17 (d, 2H, $J = 7.72$ Hz), 8.85 (s, 2H), 8.29 (s, 2H), 8.25 (s, 2H), 7.74 (d, 2H, $J =$ 4.36 Hz), 7.72 (d, 2H, $J = 4.35$ Hz), 7.68 (d, 2H, $J =$ 4.42 Hz), 7.65 (d, 2H, $J = 4.32$ Hz).
C4	8.81 (s, 2H)	9.27 (d, 2H, $J = 7.83$ Hz), 9.43 (d, 2H, $J = 7.73$ Hz), 8.83 (d, 2H, $J = 4.16$ Hz), 8.79 (s, 2H), 8.28 (d, 2H, $J =$ 4.67 Hz), 8.25 (s, 2H), 7.67 (d, 2H, $J = 4.26$ Hz), 7.65 (d, 2H, $J = 4.45$ Hz), 7.40 (s, 2H).
M4	8.86 (s, 2H)	9.30 (d, 2H, $J = 7.62$ Hz), 9.20 (d, 2H, $J = 7.71$ Hz), 8.87 (d, 2H, $J = 4.26$ Hz), 8.84 (s, 2H), 8.31 (d, 2H, $J =$ 4.84 Hz), 8.28 (s, 2H), 7.70 (d, 2H, $J = 4.32$ Hz), 7.67 (d, 2H, $J = 4.35$ Hz), 7.43 (s, 2H).
T4	8.88 (s, 2H)	9.31 (d, 2H, $J = 7.72$ Hz), 9.21 (d, 2H, $J = 7.67$ Hz), 8.88 (d, 2H, $J = 4.15$ Hz), 8.86 (s, 2H), 8.33 (d, 2H, $J =$ 4.64 Hz), 8.30 (s, 2H), 7.77 (d, 2H, $J = 4.44$ Hz), 7.68 (d, 2H, $J = 4.33$ Hz), 7.44 (s, 2H).

4.1.3 ^{13}C -NMR spectroscopy

The ^{13}C -NMR shifting of first, second, third, and fourth series compounds are shown in Table 4.9, Table 4.10, Table 4.11, and Table 4.12, respectively. The ^{13}C -NMR shifting of all compounds showed aromatic carbon shifting in the region of 170.00 – 100.00 ppm which arise from the presence of aromatic carbons (phenanthroline, fluorene, 2-hydroxynaphthalene, 2-hydroxy-3-methoxybenzene, and bisphenanthroline) in the structures. Besides, all compounds also displayed imine carbon shifting in 171.00 – 159.00 ppm due to the imine bonds in the ligands and complexes. In general, the aromatic and imine carbon shifting of complexes are higher compared to their corresponding ligands due to the deshielding effect imposed by the chromium, molybdenum, and tungsten metal centers (Gordon et al., 2019).

The phenolic carbon shiftings were observed in second and third series compounds **L2**, **C2**, **M2**, **T2**, **L3**, **C3**, **M3**, and **T3** in the region of 180.00 – 158.00 ppm. The compounds from these two series contain phenolic group in their structure (2-hydroxynaphthalene for second series and 2-hydroxy-3-methoxy for third series) in which the electron density of the phenolic carbons were shifted towards the electron withdrawing OH group causing the downfield shift in the ^{13}C -NMR. The first series compounds (**L1**, **C1**, **M1**, and **T1**) also showed unusual downfield shift in the sp^3 carbon in the 40.00 – 30.00 ppm region which can be assigned to the sp^3 carbon from the fluorene moiety in which the carbon is bonded directly to two sp^2 carbons (neighboring aromatic rings) that are highly deshielded. Other than that, ether carbon shiftings were also observed in third series compounds **L3**, **C3**, **M3**, and **T3** due to the presence of methoxy group in the benzene ring (Contreras et al., 1993).

All four series of complexes (photoCORMs) showed carbon monoxides (carbonyls) shifting in the 230.00 – 190.00 ppm region due to the presence of carbonyls in their structures. However, only two carbonyl carbon peaks were observed which due to the fact that the compounds have octahedral structure. From the result it showed that the two carbonyls at the axial positions are equivalent to each other and so is the two equatorial carbonyls, hence only two carbonyl peaks were observed in the NMR instead of four peaks (Cano et al., 1993).

Table 4.9: ^{13}C -NMR shifting of L1, C1, M1, and T1.

Compound	C=N (δ , ppm)	Aromatic (δ , ppm)	Fluorene- CH ₂ (δ , ppm)	C≡O (δ , ppm)
L1	161.91	150.83, 149.37, 148.21, 146.50, 145.90, 145.36, 144.45, 144.04, 140.92, 135.84, 134.65, 133.02, 129.24, 128.08, 127.29, 126.42, 125.46, 123.44, 123.05, 120.91, 120.37, 110.76	37.05	-

Table 4.9, Continued.

Compound	C=N (δ , ppm)	Aromatic (δ , ppm)	Fluorene– CH ₂ (δ , ppm)	C≡O (δ , ppm)
C1	163.08	153.30, 151.68, 148.86, 146.99, 146.34, 145.54, 144.36, 143.97, 140.62, 134.85, 134.03 132.71, 129.74, 129.04, 128.23, 128.15, 127.27, 125.54, 124.16, 123.79, 120.87, 110.34	36.89	229.35, 213.98
M1	163.40	153.41, 151.70, 148.99, 146.43, 145.10, 144.48, 144.04, 135.78, 133.64, 132.58, 130.27, 129.56, 129.11, 127.77, 127.26, 125.95, 125.37, 124.44, 124.03, 120.93, 120.31, 110.62	36.77	223.19, 205.07
T1	164.86	153.93, 152.34, 148.50, 146.88, 145.88, 145.27, 144.77, 144.20, 134.64, 133.17, 131.11, 130.07, 129.85, 128.67, 128.28, 127.56, 126.57, 126.35, 126.08, 125.88, 121.97, 112.29	36.90	215.21, 202.24

Table 4.10: ^{13}C -NMR shifting of L2, C2, M2, and T2.

Compound	C=N (δ , ppm)	Aromatic (δ , ppm)	Ph-OH (δ , ppm)	C \equiv O (δ , ppm)
L2	165.6	151.19, 150.07, 146.66, 145.55, 144.51, 136.71, 135.99, 133.06, 132.16, 129.71, 128.85, 128.56, 128.07, 125.30, 124.21, 123.73, 123.57, 120.39, 119.51, 113.07, 109.97	159.94	-
C2	167.37	166.20, 165.42, 153.73, 152.36, 151.39, 145.93, 143.40, 138.73, 137.95, 137.17, 135.02, 132.88, 129.96, 129.18, 128.20, 125.28, 124.31, 119.63, 118.85, 113.01, 110.28	177.89	229.13, 213.93
M2	170.01	163.13, 154.21, 152.54, 142.14, 139.16, 137.68, 136.38, 133.96, 133.22, 132.29, 130.99, 130.25, 129.13, 128.02, 125.60, 124.86, 123.00, 120.21, 119.10, 112.97, 111.85	164.25	196.02, 193.60

Table 4.10, Continued.

Compound	C=N (δ , ppm)	Aromatic (δ , ppm)	Ph-OH (δ , ppm)	C \equiv O (δ , ppm)
T2	170.78	157.86, 156.32, 146.69, 145.16, 144.06, 138.59, 135.74, 131.58, 130.71, 129.83, 127.21, 125.08, 122.73, 121.86, 120.73, 118.29, 116.98, 112.63, 112.11, 105.67, 102.45	159.39	222.23, 206.46

Table 4.11: ^{13}C -NMR shifting of L3, C3, M3, and T3.

Compound	C=N (δ , ppm)	Aromatic (δ , ppm)	Ph-OH (δ , ppm)	O-CH ₃ (δ , ppm)	C \equiv O (δ , ppm)
L3	164.88	150.96, 149.92, 148.58, 146.39, 145.47, 144.71, 135.86, 131.99, 128.53, 125.24, 124.08, 123.47, 123.32, 119.16, 115.53, 112.54	151.44	56.26	-

Table 4.11, Continued.

Compound	C=N (δ , ppm)	Aromatic (δ , ppm)	Ph-OH (δ , ppm)	O-CH ₃ (δ , ppm)	C=O (δ , ppm)
C3	167.12	153.13, 152.34, 150.76, 149.58, 148.20, 146.42, 136.57, 133.22, 130.46, 129.48, 128.49, 126.13, 124.35, 120.21, 116.67, 113.32	154.31	68.97	205.55, 198.06
M3	166.27	152.21, 151.49, 148.66, 146.79, 145.74, 135.93, 132.64, 129.81, 129.04, 128.23, 125.30, 124.58, 124.43, 119.54, 116.16, 112.70	153.40	67.98	218.98, 204.87
T3	167.56	153.54, 152.34, 148.94, 146.74, 145.74, 137.25, 133.73, 132.32, 128.88, 128.15, 125.73, 123.92, 121.71, 119.51, 116.71, 113.71	163.56	55.97	201.99, 198.19

Table 4.12: ^{13}C -NMR shifting of L4, C4, M4, and T4.

Compound	C=N (δ , ppm)	Aromatic (δ , ppm)	C \equiv O (δ , ppm)
L4	160.53	150.86, 149.58, 147.52, 146.39, 145.45, 138.83, 135.83, 132.73, 130.20, 129.71, 128.86, 126.08, 123.40, 122.99, 110.77	-
C4	164.52	154.85, 153.56, 151.51, 150.38, 149.44, 142.81, 139.82, 136.72, 134.18, 133.72, 132.84, 130.07, 127.38, 126.98, 114.76	200.11, 198.69
M4	162.51	152.88, 151.51, 149.50, 148.27, 147.40, 140.79, 137.82, 134.72, 132.07, 131.72, 130.79, 128.08, 125.29, 124.90, 112.75	204.94, 203.44
T4	159.29	159.29, 148.33, 146.28, 145.15, 144.21, 137.59, 135.98, 131.49, 128.95, 128.49, 127.62, 124.84, 122.16, 121.75, 109.53	205.90, 202.51

4.1.4 UV-Vis Spectroscopy

The UV-Vis spectra of the first, second, third, and fourth series compounds in 10% DMSO-H₂O solution are shown in Figure 4.1, Figure 4.2, Figure 4.3, and Figure 4.4, respectively.

The ligands (**L1**, **L2**, **L3**, and **L4**) showed strong absorption in the range of 300 – 600 nm (one peak for **L1** and **L4**, two peaks for **L2** and **L3**). The photoCORMs on the other hand also demonstrated strong absorption in the range of 300 – 600 nm (two peaks for first, third, and fourth series, three peaks for second series photoCORMs) region in which the peaks can be attributed to the d–d metal-to-ligand charge transfer (MLCT) and the metal→ π^* [CO] absorptions (overlapped by the absorption of the MLCT band) which explained their UV activated CO-releasing properties (Berends & Kurz, 2012; Kubeil et al., 2017). The binding of the ligands to Cr, Mo, and W metal centers had labialized the metal-to-CO back bondings due to the presence of high number of double bond conjugations in the ligand structures which weaken the M–CO bonds in all the photoCORMs. Consequently, the UV light illumination (365 nm) will cause the breaking of M-CO bonds and the COs will therefore be released from the metal centers. (Chakraborty et al., 2014). Besides, hypsochromic shifts were observed in the order of Cr, Mo, and W (down the group 6) for all series photoCORMs (Elschenbroich et al., 1998).

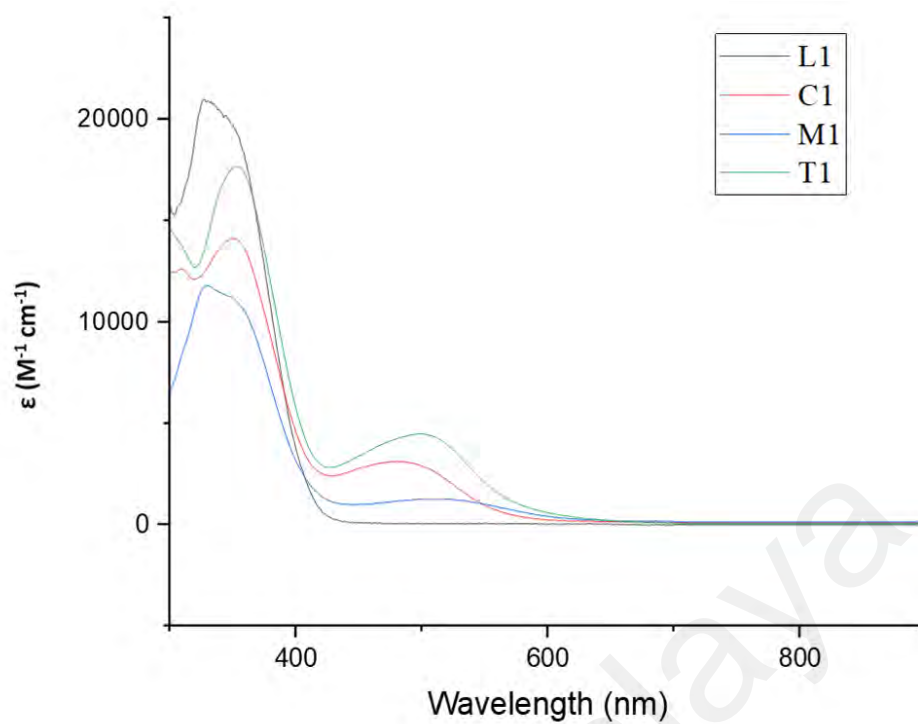


Figure 4.1: UV-Vis spectra of L1, C1, M1, and T1 at 60 μ M in 10% DMSO-H₂O.

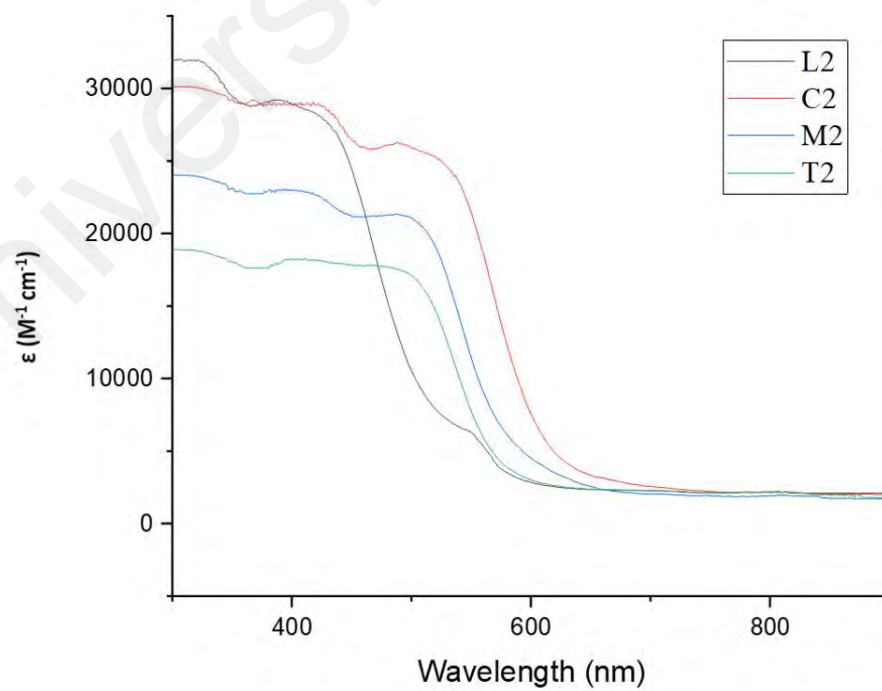


Figure 4.2: UV-Vis spectra of L2, C2, M2, and T2 at 60 μ M in 10% DMSO-H₂O.

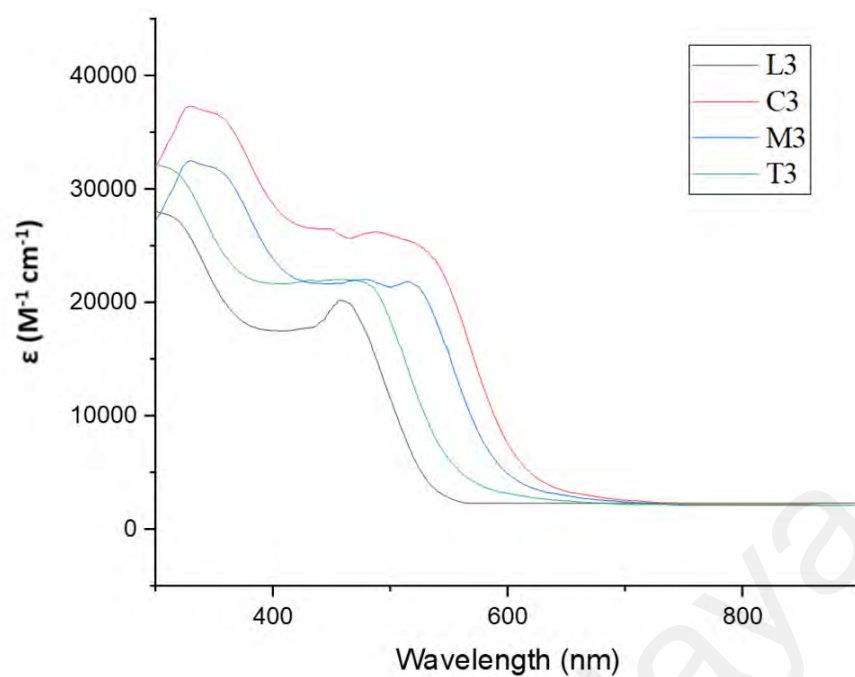


Figure 4.3: UV-Vis spectra of L3, C3, M3, and T3 at 60 μ M in 10% DMSO-H₂O.

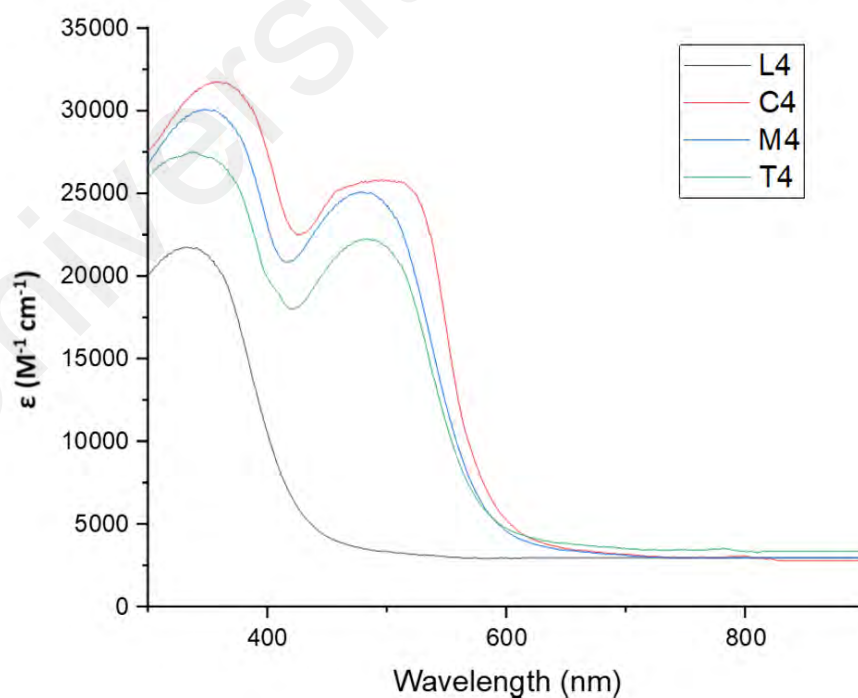


Figure 4.4: UV-Vis spectra of L4, C4, M4, and T4 at 60 μ M in 10% DMSO-H₂O.

4.1.5 X-ray Crystallography

A total of 12 crystal structures were obtained from the 16 synthesized compounds. The crystal data and structural refinement parameters for the first series compounds, **L1**, **C1**, **M1**, and **T1** are shown in Table 4.13. The selected bond length and bond angle of **L1**, **C1**, **M1**, and **T1** are shown in Appendix B. The crystal structure and unit cell packing of **L1** and **C1** are shown in Figure 4.5 and Figure 4.6, respectively, whereas **M1** and **T1** are shown in Appendix A.

All the first series compounds crystallized in a monoclinic system. Compound **L1** crystallized in $P2_1$ space group whereas **C1**, **M1**, and **T1** crystallized in $P2_1/c$ space group. Compounds **C1**, **M1**, and **T1** showed distorted yet stable octahedral structures as predicted by using 18 electron rules (6 electrons from metal centers, 8 electrons from the COs, and 4 electrons from the phenanthroline nitrogen). Despite losing two COs during the reaction process the compounds were quickly stabilized by the binding of two phenanthroline nitrogens hence retaining their stable 18 electrons state and structures (Brathwaite et al., 2014). The angles of N1–Cr1–N2, N1–Cr1–C29, N1–Mo1–N2, N1–Mo1–C27, N2–W1–N3, and N2–W1–C30 are deviated from the ideal 90° due to the steric hindrance imposed by the ligand **L1** (Cotton et al., 1982). The metal carbonyl (M–CO) bond lengths around the metals are different in all compounds, whereby the two equatorial M–CO bond lengths are slightly shorter than those at axial position, despite less obvious in Cr–CO compared to Mo–CO and W–CO. Regardless of the position of CO, the overall M–CO bond length increases in the order of **C1** < **T1** < **M1** which correspond to Cr < W < Mo. The crystal packings of **C1**, **M1**, and **T1** are similar to each other, in which the aromatic rings are stacked in a herringbone fashion as viewed along the c-axis (Lee et al., 2014). Besides, the molecules also displayed Van der Waals and hydrogen bond interactions with each other due to the presence of dipoles induced by the COs in the structures (Moondra et al., 2018).

Table 4.13: Crystallographic data summary for L1, C1, M1, and T1.

Compound	L1	C1	M1	T1
Empirical formula	C ₂₆ H ₁₇ N ₃	C ₃₀ H ₁₇ N ₃ O ₄ Cr	C ₃₀ H ₁₇ N ₃ O ₄ Mo	C ₃₀ H ₁₇ N ₃ O ₄ W
Formula weight	371.42	534.46	578.40	664.29
Crystal system	Monoclinic	Monoclinic	Monoclinic	Monoclinic
Space group	P2 ₁	P2 ₁ /c	P2 ₁ /c	P2 ₁ /c
Unit cell dimensions				
<i>a</i> (Å)	4.0562(6)	8.7127(18)	8.6948(2)	8.6988(2)
<i>b</i> (Å)	15.9054(19)	13.8448(4)	13.9270 (4)	13.9133(3)
<i>c</i> (Å)	15.335(13)	20.6444(5)	20.8599(6)	20.7991(4)
β (°)	93.374(13)	89.734(2)	90.287(2)	90.258(2)
<i>V</i> (Å ³)	987.7(2)	2490.21(10)	2525.95(11)	2514.85(9)
<i>Z</i>	2	4	4	4
<i>F</i> (000)	388.0	1092.0	1164.0	1284.0
ρ_{calc} (mg m ⁻³)	1.249	1.426	1.521	1.755
Absorption coefficient, μ (mm ⁻¹)	0.581	4.135	4.599	8.866
<i>T</i> (K)	293	293	293	293
Crystal size (mm)	0.2 × 0.1 × 0.05	0.3 × 0.1 × 0.1	0.25 × 0.1 × 0.1	0.2 × 0.1 × 0.1
Reflections collected	5505	14478	13559	13393
Independent reflections (<i>R</i> _{int})	3352	4990	5025	4473
Data/restraints/parameters	3352/1/262	4990/0/343	5025/0/343	4473/0/343
Goodness-of-fit on, <i>F</i> ²	1.026	1.012	1.198	0.915
<i>R</i> ₁	0.0526	0.083	0.0629	0.0630
<i>wR</i> ₂	0.1273	0.2110	0.1687	0.1448

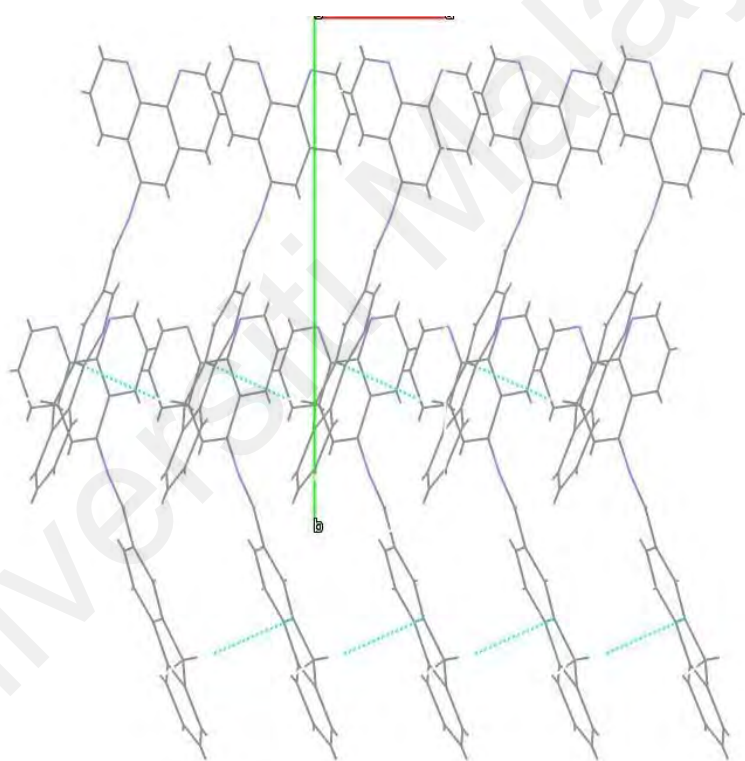
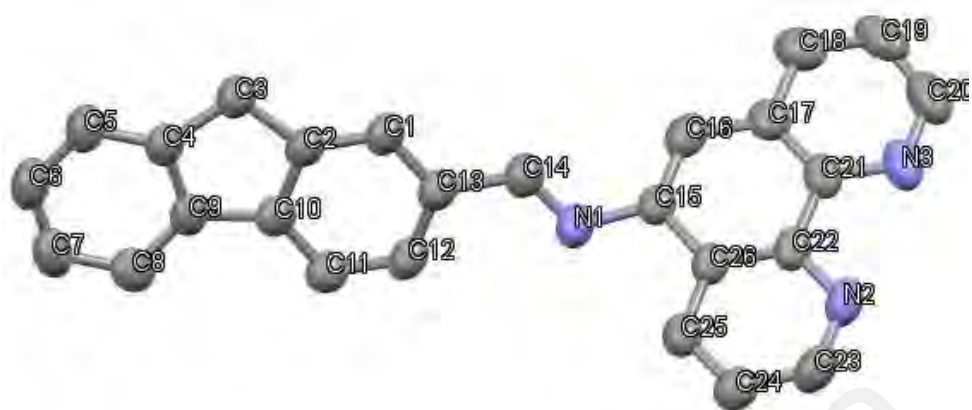


Figure 4.5: Crystal structure and crystal packing viewed along c-axis of L1.

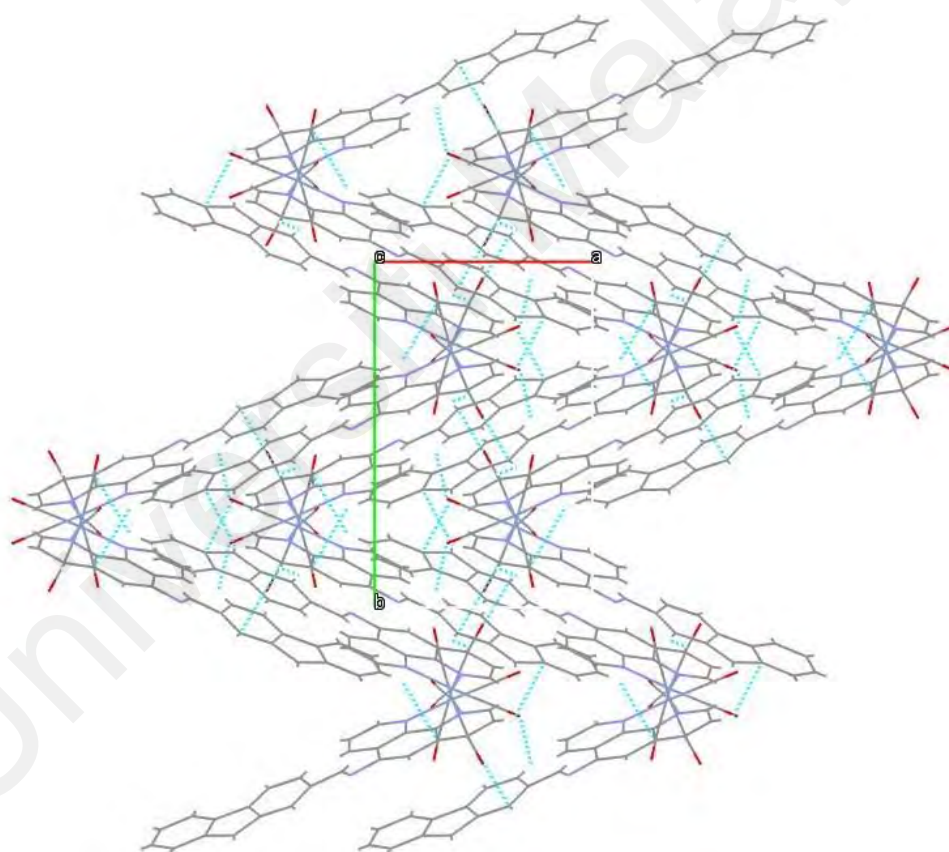
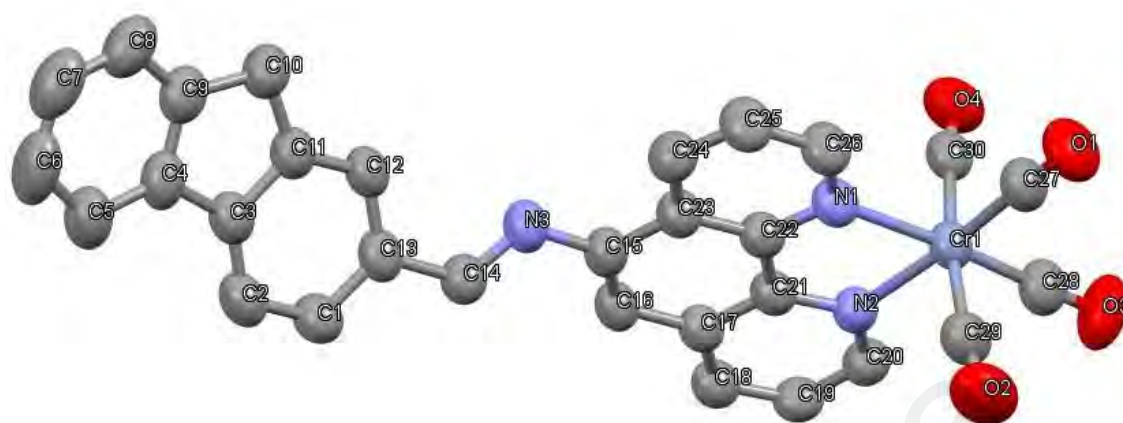


Figure 4.6: Crystal structure and crystal packing viewed along c-axis of C1.

The crystal data and structural refinement parameters for the second series compounds, **L2**, **C2**, **M2**, and **T2** are shown in Table 4.14. The selected bond length and bond angle of **L2**, **C2**, **M2**, and **T2** are shown in Appendix B, respectively. The crystal structures and unit cell packings of **L2** and **C2**, are shown in Figure 4.7 and Figure 4.8, respectively, whereas **M2**, and **T2** are shown in Appendix A.

Compounds **L2** and **C2** crystallized in a monoclinic crystal system with space groups of $P2_1/c$ and $P2_1/n$ respectively, whereas **M2** and **T2** crystallized in orthorhombic crystal system and with the same space group of $Pca2_1$. Compounds **C2**, **M2**, and **T2** displayed distorted octahedral structures with axial and equatorial OC–M–CO bonds deviated from the ideal 180° and 90° bond angles respectively. From the crystal data the angles of axial OC–M–CO bonds of **C2**, **M2**, and **T2** are 169.8° , 169.5° and 168.0° , respectively, whereas the equatorial OC–M–CO of **C2**, **M2**, and **T2** are 91.1° , 91.3° and 90.7° . The slight deviations in the bond angles are due to the possible steric hindrance imposed by the binding of ligand **L2** to the metal center. Similarly, the two phenanthroline nitrogen to metal center bond, N–M–N bond angles of **C2**, **M2**, and **T2** showed deviation from the ideal 90° bond angle with 77.1° , 74.0° and 73.2° , respectively (Cotton et al., 1982). Besides bond angles, the metal to carbonyl, M–CO bond lengths are different for axial and equatorial CO. Generally, the axial M–CO bond length are slightly longer than the equatorial M–CO bond for **2**, **3** and **4** which agree with the data of IR and ^{13}C NMR showing the possible existence of non-equivalent CO. The overall M–CO bond length increases in the order of **C2** < **M2** < **T2**, which correspond to $\text{Cr} < \text{Mo} < \text{W}$ regardless of the position of CO.

The crystal packing of **L2** and **C2** showed that the compounds are stacked together in a herringbone fashion as observed along the c-axis (Lee et al., 2014). The crystal packing of **M2** and **T2** showed that two molecules attracted to one another at the metal centre to form a dimer and were arranged and stacked in a wave-like pattern viewed along the c-axis.

Universiti Malaya

Table 4.14: Crystallographic data summary for L2, C2, M2, and T2.

Compound	L2	C2	M2	T2
Empirical formula	C ₂₃ H ₁₅ N ₃ O	C ₃₁ H ₂₃ N ₃ O ₆ Cr	C ₂₇ H ₁₅ N ₃ O ₅ Mo	C ₃₁ H ₂₃ N ₃ O ₆ W
Formula weight	349.38	585.52	556.88	717.37
Crystal system	Monoclinic	Monoclinic	Orthorhombic	Orthorhombic
Space group	P2 ₁ /c	P2 ₁ /n	Pca2 ₁	Pca2 ₁
Unit cell dimensions				
a (Å)	12.197(2)	14.3348(4)	28.1312(12)	27.9919(7)
b (Å)	12.047(2)	7.2523(2)	7.3153(3)	7.3043(3)
c (Å)	12.829(3)	26.0260(8)	26.6497(13)	26.6570(7)
α (°)	90	90	90	90
β (°)	112.20(2)	95.580(2)	90	90
γ (°)	90	90	90	90
V (Å ³)	1745.4(6)	2692.85(13)	5484.2(4)	5450.3(3)
Z	4	4	8	8
F(000)	728.0	1208.0	2238.0	2816.0
ρ _{calc} (mg m ⁻³)	1.330	1.444	1.349	1.748
Absorption coefficient, μ (mm ⁻¹)	0.665	3.928	4.223	8.285
T (K)	293(2)	293(2)	293(2)	293(2)
Crystal size (mm)	0.3 × 0.2 × 0.2	0.2 × 0.1 × 0.1	0.1 × 0.1 × 0.1	0.2 × 0.1 × 0.1
Reflections collected	5559	7744	9955	31280
Independent reflections (R _{int})	3348	4741	6240	10596
Data/restraints/parameters	3348/0/245	4741/396/3 75	6240/7/653	10596/1749/74 2
Goodness-of-fit on F ²	1.044	1.050	0.976	1.016
R ₁	0.1065	0.0718	0.0563	0.0617
wR ₂	0.2774	0.1577	0.1354	0.1358

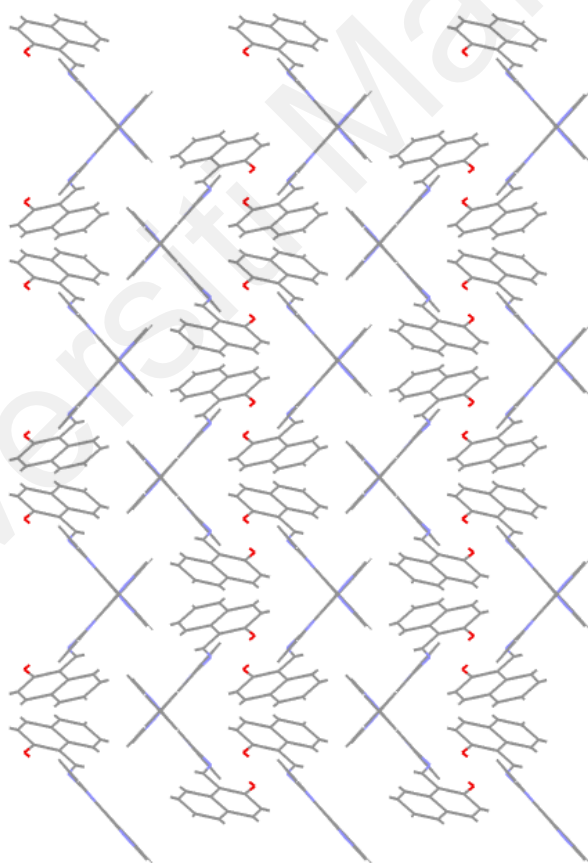
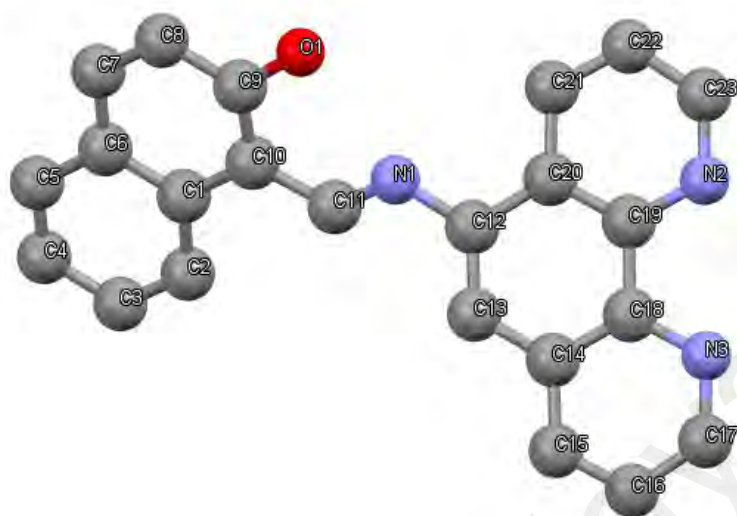


Figure 4.7: Crystal structure and crystal packing viewed along c-axis of L2.

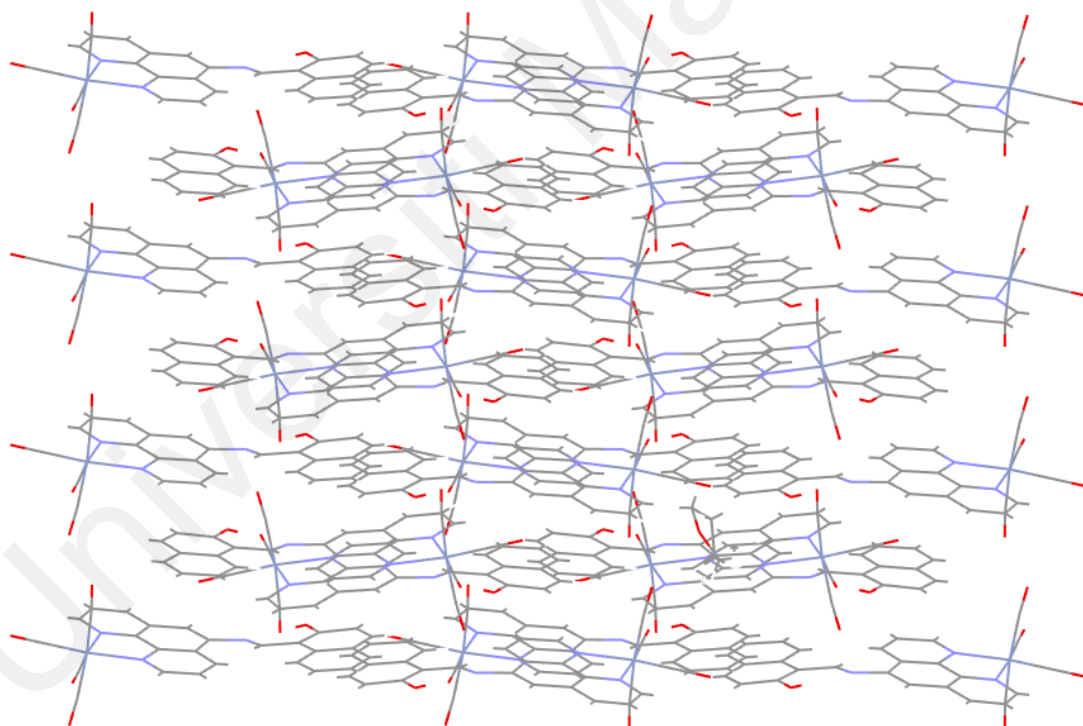
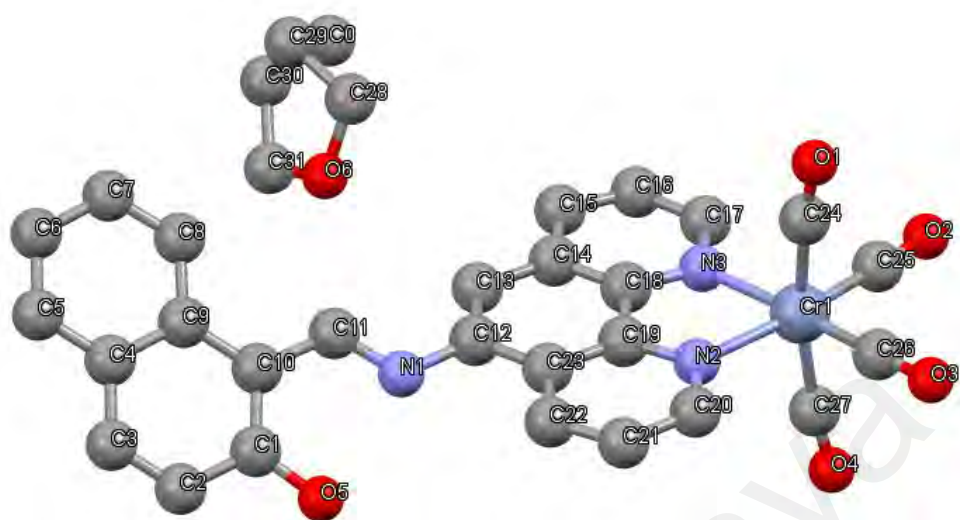


Figure 4.8: Crystal structure and crystal packing viewed along c-axis of C2.

The crystal data and structural refinement parameters for the third series compounds, **L3** and **M3** are shown in Table 4.15. The selected bond length and bond angle of **L3** and **M3** are shown in Appendix B. The crystal structure and unit cell packing of **L3** and **M3** are shown in Figure 4.9 and Figure 4.10, respectively.

Compound **L3** crystallized in triclinic system with P-1 space group, which contained methanol as part of the crystal system. All the C–C–C bond angles in **L3** are near 120° angles, similarly for the non C–C–C bonds such as C1–O1–C3, C7–C8–N1, C8–N1–C9, C14–N3–C15, and C16–N2–C17. The crystal packing of **L3** showed that two molecules of **L3** were stacked together at the phenanthroline site and the dimers were arranged in a herringbone fashion as viewed along the b-axis (Lee et al., 2014). Compound **M3** crystallized in an orthorhombic system with Fdd2 space group and showed a distorted octahedral structure. The C2–Mo1–C3, C2–Mo1–C4, and N2–Mo1–N3 angles collectively showed slight deviations from the expected 90° bond angle. Furthermore, the two axial COs to Mo bond angle, C1–Mo1–C4 is reported to be 172.4°, which also showed deviation from the expected 180° angle. These phenomena can be attributed to the steric hindrance that is possibly caused by the bonding of **L3** to the Mo center. The bond lengths between two axial COs to Mo (1.990 and 1.963 Å) are slightly shorter than those at the equatorial position (2.000 and 2.020 Å). The crystal packing of **M3** showed that two molecules of **M3** were stacked together via the 2-hydroxy-3-methoxy benzene and the phenanthroline benzene, whereby the dimers were arranged in a herringbone fashion similar to **L3** as viewed along the c-axis (Lee et al., 2014).

Table 4.15: Crystallographic data summary for L3 and M3.

Compound	L3	M3
Empirical formula	C ₂₁ H ₁₉ N ₃ O ₃	C ₂₄ H ₁₆ N ₃ O ₆ Mo
Formula weight	361.39	538.34
Crystal system	Triclinic	Orthorhombic
Space group	P-1	Fdd2
Unit cell dimensions		
<i>a</i> (Å)	6.9237(7)	58.939(3)
<i>b</i> (Å)	10.076(2)	26.089(2)
<i>c</i> (Å)	26.9748(18)	7.2828(7)
β (°)	85.358(7)	90
<i>V</i> (Å ³)	1824.0(5)	11198.3(16)
<i>Z</i>	4	16
<i>F</i> (000)	760.0	4336.0
ρ_{calc} (mg m ⁻³)	1.316	1.277
Absorption coefficient, μ (mm ⁻¹)	0.731	4.159
<i>T</i> (K)	291	300
Crystal size (mm)	0.4 × 0.2 × 0.1	0.2 × 0.1 × 0.05
Reflections collected	10693	5610
Independent reflections (<i>R</i> _{int})	6936	3767
Data/restraints/ parameters	6936/0/495	3767/322/308
Goodness-of-fit on <i>F</i> ²	1.061	1.130
<i>R</i> ₁	0.1262	0.0698
<i>wR</i> ₂	0.3743	0.1862

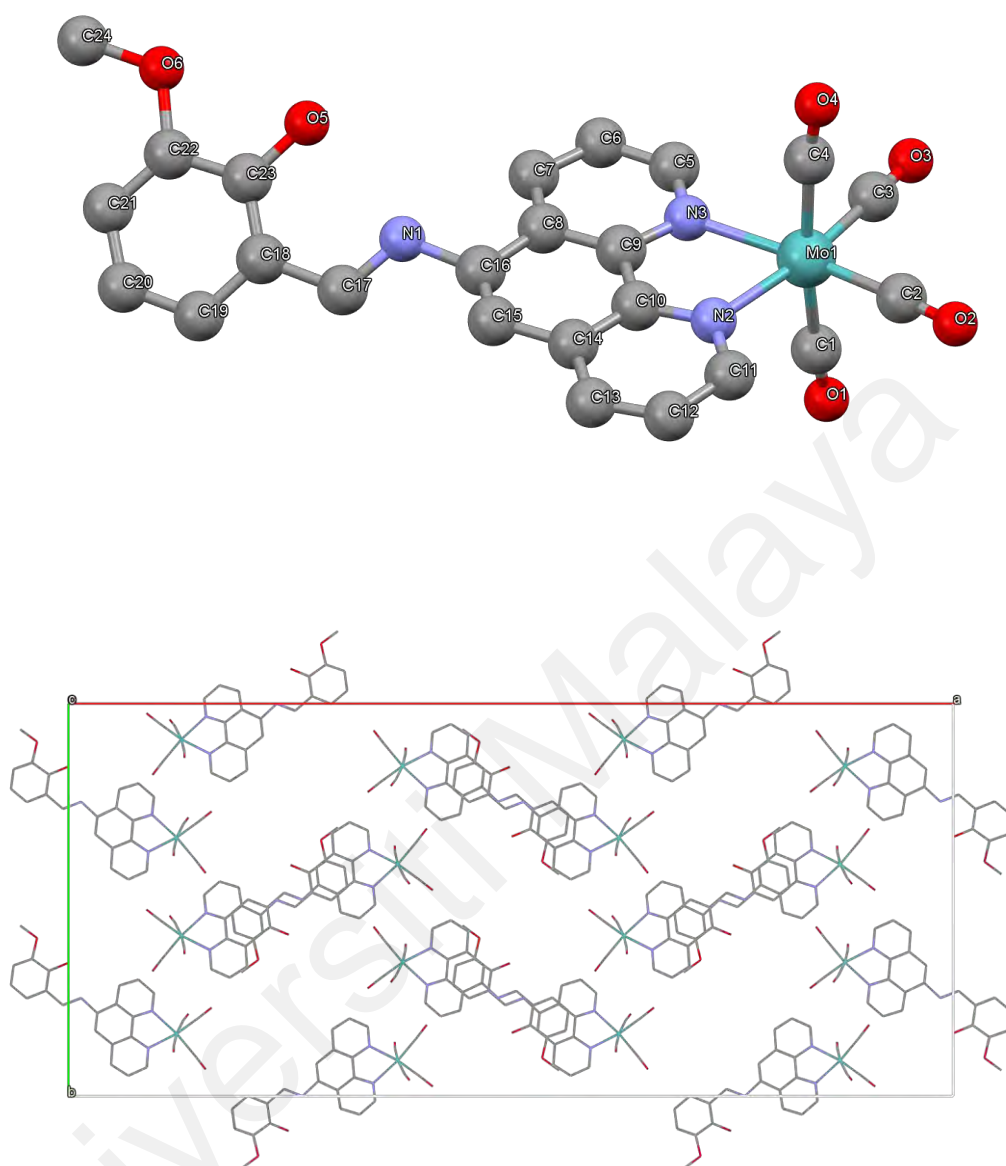


Figure 4.10: Crystal structure and crystal packing viewed along c-axis of M3.

The crystal data and structural refinement parameters for the fourth series compounds, **L4** and **M4** are shown in Table 4.16. The selected bond length and bond angle of **L4** and **M4** are shown in Appendix B. The crystal structure and unit cell packing of **L4** and **M4** are shown in Figure 4.11 and Figure 4.12, respectively.

The crystal structure of compound **L4** has a C_2 symmetrical bisphenanthroline moiety which crystallized in triclinic system with P-1 space group, which contained water as part of the crystal system. All the C–C–C bond angles in **L4** are near 120° angles, similarly for the non C–C–C bonds such as C1–N1–C5, C6–N2–C7 and C12–N3–C13. The crystal packing of **L4** showed that the molecules were stacked together end-to-end at the phenanthroline sites and the molecules were arranged in a stair-like manner as viewed along the b-axis. The crystal structure of compound **M4** is a symmetrical bimetallic complex with eight COs which crystallized in a triclinic system with P-1 space group similar to **L4** and showed a distorted octahedral structure. The C1–Mo1–C3, C1–Mo1–C4, and N1–Mo1–N2 angles collectively showed slight deviations from the expected 90° bond angle. Furthermore, the axial CO to Mo bond angle, C2–Mo1–C4 is reported to be 169.2° , which also showed deviation from the expected 180° angle. These phenomena can be attributed to the steric hindrance imposed by the bonding of **L4** to the two Mo center (Cotton et al., 1982). The bond lengths of one of the axial CO to Mo, C2–Mo1 (2.026 Å) is unusually longer than the rest of the Mo–CO bonds (1.975, 1.936, and 1.913 Å). The crystal packing of **M4** is similar to its ligand **L4**, in which the **M4** were stacked together end-to-end at the phenanthroline sites and the molecules were arranged in a stair-like manner as viewed along the b-axis.

Table 4.16: Crystallographic data summary for L4 and M4.

Compound	L4	M4
Empirical formula	C ₃₂ H ₂₂ N ₆ O ₂	C ₂₄ H ₁₈ N ₃ O ₅ Mo
Formula weight	522.55	524.35
Crystal system	Triclinic	Triclinic
Space group	P-1	P-1
Unit cell dimensions		
<i>a</i> (Å)	7.5474(14)	10.032(5)
<i>b</i> (Å)	9.5446(14)	10.551(6)
<i>c</i> (Å)	9.9941(8)	12.000(6)
β (°)	110.260(13)	105.94(4)
<i>V</i> (Å ³)	636.55(17)	1106.1(11)
<i>Z</i>	1	2
<i>F</i> (000)	272.0	530.0
ρ_{calc} (mg m ⁻³)	1.363	1.574
Absorption coefficient, μ (mm ⁻¹)	0.713	0.634
<i>T</i> (K)	293	295
Crystal size (mm)	0.5 × 0.3 × 0.1	0.1 × 0.05 × 0.05
Reflections collected	3168	7840
Independent reflections (<i>R</i> _{int})	2093	7840
Data/restraints/ parameters	2093/0/184	7840/340/303
Goodness-of-fit on <i>F</i> ²	0.914	0.641
<i>R</i> ₁	0.0920	0.0931
<i>wR</i> ₂	0.2314	0.1296

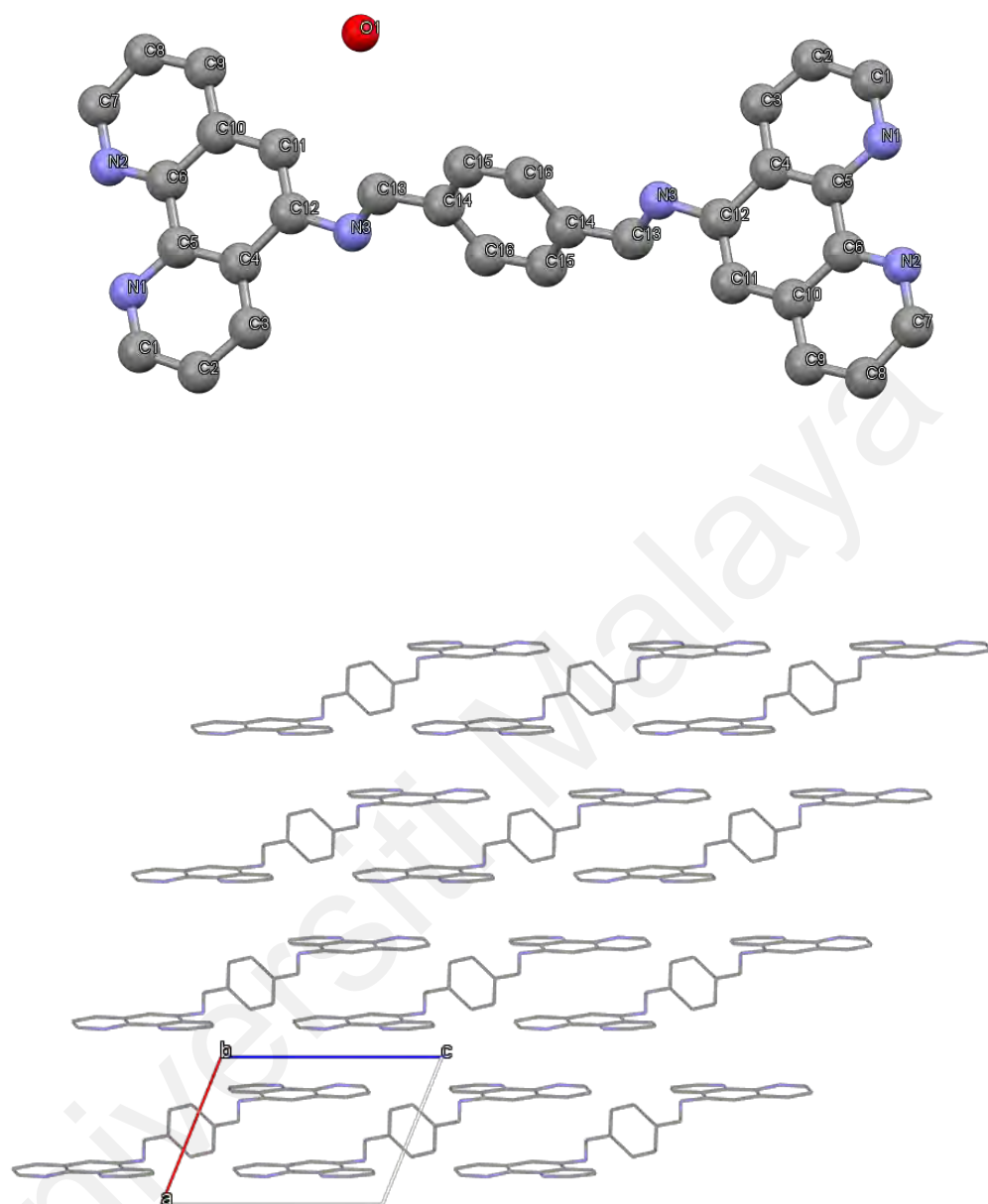


Figure 4.11: Crystal structure and crystal packing viewed along b-axis of L4.

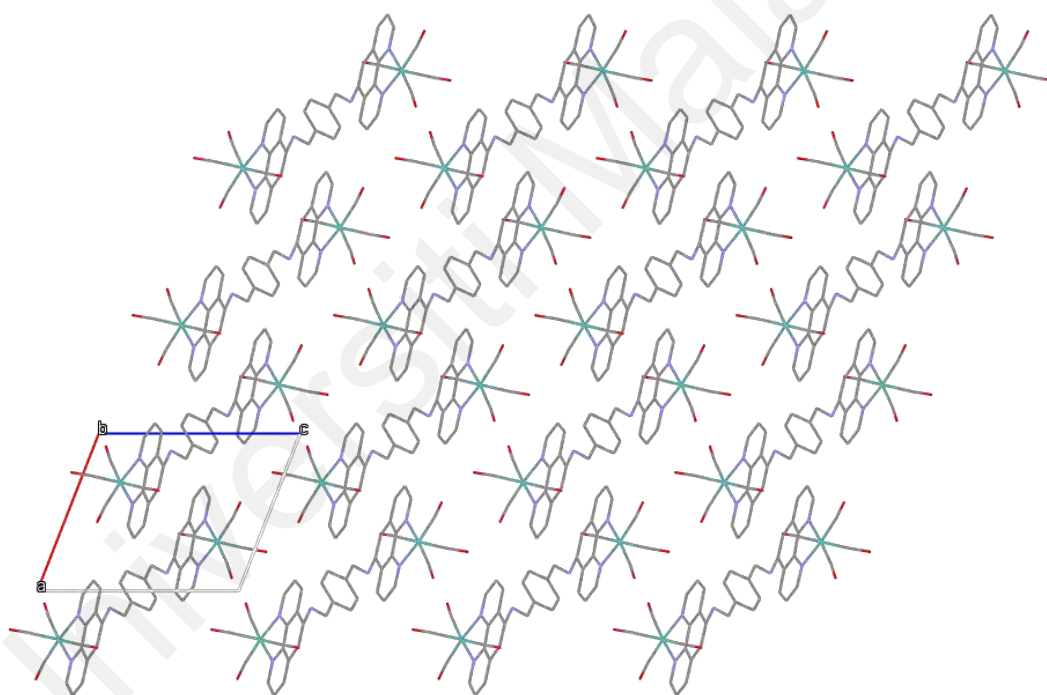
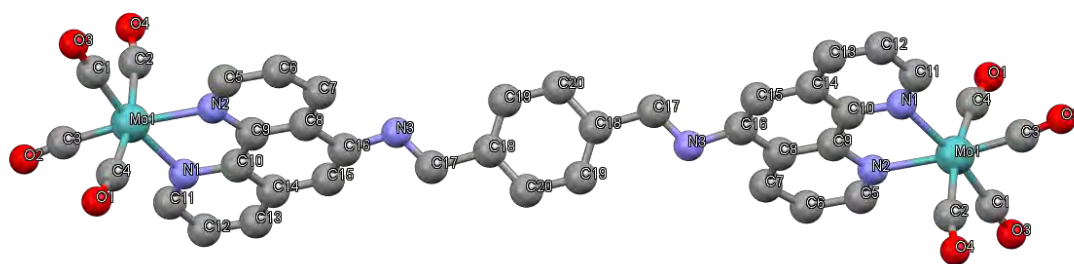


Figure 4.12: Crystal structure and crystal packing viewed along b-axis of M4.

4.2 Myoglobin Assays

4.2.1 Three-Layered Myoglobin solution

The example of UV spectra of **M1** (60 μ M) conducted using the standard version of myoglobin assay is shown in Figure 4.13. It showed that the Mb/MbCO UV absorbance experienced substantial shifting as the assay progressed. Such observation could be attributed to the poor aqueous solubility of inactive CORMs (iCORMs) in the myoglobin solution, especially the first and fourth series compounds after the photoCORMs being dissolved in DMSO and illuminated by UV, thereby increasing the turbidity of the solution and giving rise to inaccurate and shifted absorbance (Atkin et al., 2011). Moreover, such issue could also be encountered when the photoCORM itself is a strong UV absorber in the 500 – 600 nm region such as second, third and fourth series photoCORMs which may interfere with the absorbance of the Mb solution. Furthermore, a number of studies showed that the heme and sodium dithionite in the myoglobin solution will induce the CO release in CORMs, whereby they potentially act as CO extractor and catalyze the CO release from the CORMs, leading to an inaccurate CO releasing half-life (Klein et al., 2014; McLean et al., 2012; Santos-Silva et al., 2011).

Therefore, in this study a modified version of myoglobin assay which is called three-layered myoglobin solution method based on the standard myoglobin assay was developed and employed (Atkin et al., 2011). The experimental setup is shown in Figure 4.14. Given the fact that chloroform (containing the photoCORMs) forms an immiscible layer under the myoglobin solution, the CO released by the tested photoCORMs upon UV light (365 nm) illumination on the chloroform layer are immediately captured by the myoglobin solution above. Thus, all the above-mentioned problems are resolved because the photoCORMs in the chloroform layer are completely separated from myoglobin solution, minimizing the contact of sodium dithionite with photoCORMs. In addition,

turbidity could be avoided as all the insoluble iCORMs remained in the chloroform layer, therefore the UV absorbance of the photoCORMs will not interrupt with the absorbance of the myoglobin solution. The example of UV spectra of **M1** (60 μM) conducted using three-layered myoglobin solution is shown in Figure 4.15 which gives a more accurate result/spectra with less shifting in the absorbance.

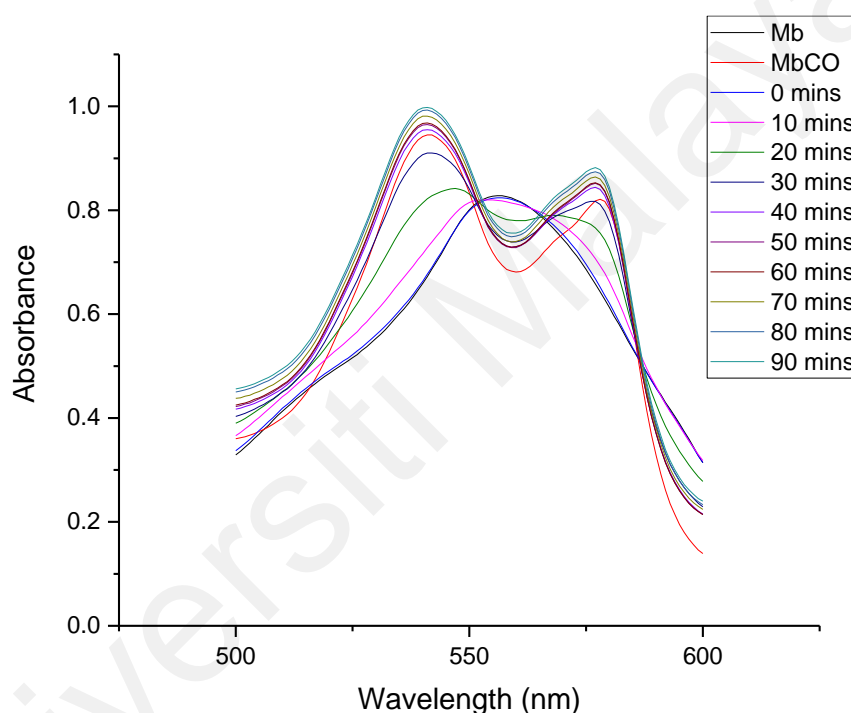


Figure 4.13: UV-Vis spectrum of conventional myoglobin assay of M1 (60 μM) showed deviations in the absorbance.

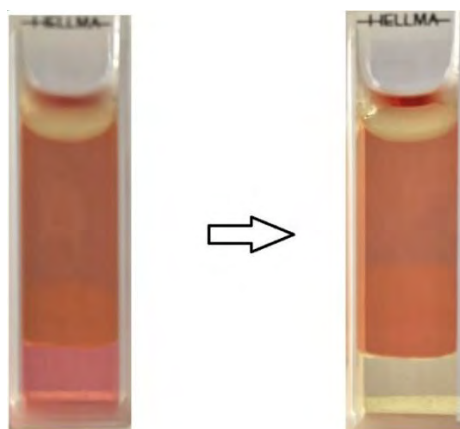


Figure 4.14: Cuvette before UV irradiation (left). After UV irradiation at 365 nm, the CO released were captured by the myoglobin solution on top, all the insoluble iCORM remained at the bottom layer (right).

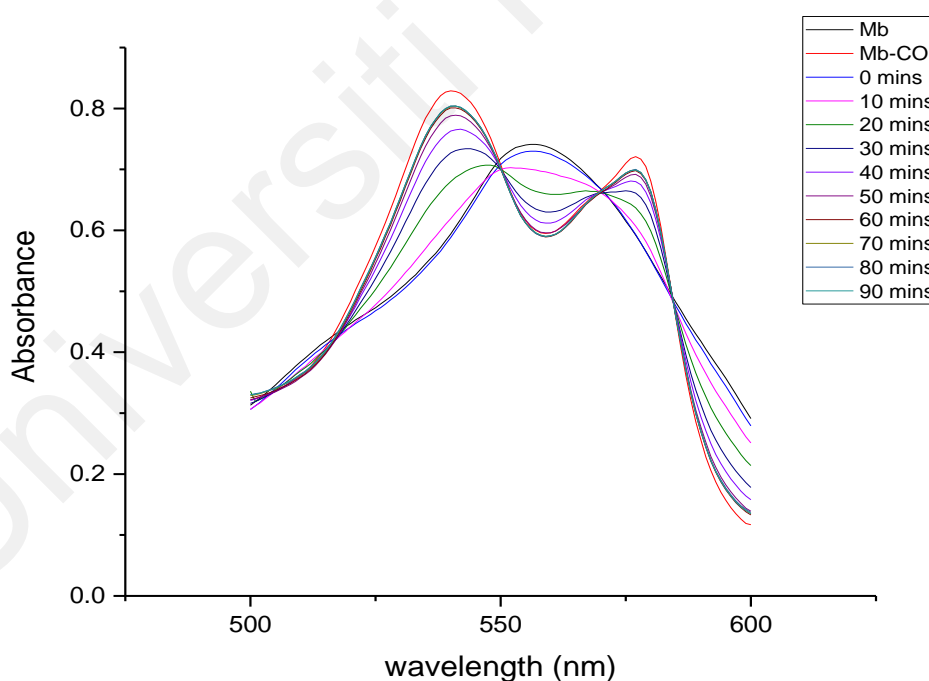


Figure 4.15: UV-Vis spectrum of myoglobin assay of M1 (60 μ M) conducted using three-layered myoglobin solution.

4.2.2 Half-life of PhotoCORMs **C1**, **M1**, and **T1**

The half-life of photoCORMs is defined as the time taken to produce Mb-CO solution with a concentration that is half of the photoCORMs' initial concentration (Meyer et al., 2015). In our case, it is the time taken for 60 μM of photoCORMs to produce 30 μM of Mb-CO solution (and so forth). Three different photoCORMs concentrations, 20, 40, and 60 μM were used in this study. The half-life and number of CO released from all photoCORMs were measured using the three layered myoglobin solution.

The half-life and the number of CO released from first series photoCORMs, namely **C1**, **M1**, and **T1** are shown in Table 4.17 and Table 4.18, respectively. Generally, the compounds showed a decreasing half-life with an increasing concentration, tentatively suggesting that the CO releasing mechanism is not a first order rate of reaction where several intermediates could be involved in the photolysis reaction (Atkin et al., 2011). Compound **C1** showed the highest CO-releasing rate at 60 μM with a half-life of 12.5 ± 2.9 seconds, whereas **M1** and **T1** were 28.4 ± 0.5 and 31.8 ± 0.4 minutes, respectively. Both **M1** and **T1** showed similar half-life at different concentrations.

Table 4.17: Half-life ($t_{1/2}$) of C1, M1, and T1 at different concentrations.

Compound	Half-life ($t_{1/2}$)		
	20 (μ M)	40 (μ M)	60 (μ M)
C1	14.8 \pm 0.5 mins*	23.9 \pm 3.5 secs*	12.5 \pm 2.9 secs
M1	59.7 \pm 0.3 mins	40.9 \pm 0.3 mins	28.4 \pm 0.5 mins
T1	52.10 \pm 0.4 mins	33.9 \pm 0.3 mins	31.8 \pm 0.4 mins

*secs = seconds, mins = minutes

Table 4.18: Number of CO released per molecule of C1, M1, and T1.

Compound	No. of CO released per mol
C1	3.74 \pm 0.21
M1	3.05 \pm 0.37
T1	3.73 \pm 0.19

4.2.3 Half-life of PhotoCORMs C2, M2, and T2

The half-life and the number of CO released of second series photoCORMs, namely **C2**, **M2**, and **T2** are shown in Table 4.19 and Table 4.20, respectively. All compounds demonstrated decreasing half-life with increasing concentration which is similar to the first series photoCORMs. From Table 31, half-life of **C2**, **M2** and **T2** at 60 μM are notably shorter compared to 20 μM . Compounds **C2** displayed the shortest half-life of 7.1 seconds at 60 μM , compared to **M2** and **T2** with half-life of 15.3 and 22.5 minutes respectively. At 20 μM however, compound **T2** presented the longest half-life of 33.7 minutes in contrast to compound **C2** and **M2** with half-life of 8.8 seconds and 19.7 minutes. It is interesting to note that the half-life of the compounds increased down the group 6 in the order of $\text{Cr} < \text{Mo} < \text{W}$ which correlates to the trend in the increasing in M-CO bond length down the group shown in the crystallographic data.

Table 4.19: Half-life ($t_{1/2}$) of C2, M2, and T2 at different concentrations.

Compound	Half-life ($t_{1/2}$)		
	20 (μM)	40 (μM)	60 (μM)
C2	8.8 ± 0.3 secs	8.4 ± 0.7 secs	7.1 ± 0.5 secs
M2	19.7 ± 1.3 mins	17.6 ± 1.0 mins	15.3 ± 0.6 mins
T2	33.7 ± 2.7 mins	25.59 ± 1.5 mins	22.5 ± 1.1 mins

Table 4.20: Number of CO released per molecule of C2, M2, and T2.

Compound	No. of CO released per mol
C2	3.65 ± 0.11
M2	3.61 ± 0.10
T2	3.64 ± 0.13

4.2.4 Half-life of PhotoCORMs C3, M3, and T3

The half-life and number of CO released of third series photoCORMs, namely **C3**, **M3**, and **T3** are shown in Table 4.21 and Table 4.22, respectively. Similar to the first and second series photoCORMs, the compounds displayed a decreasing half-life with an increasing compound concentration, this again suggest that the rate of CO release is not a first order reaction. The half-lives of **C3**, **M3**, and **T3** at 60 μM are significantly shorter compared to those at 20 μM . Particularly, **C3** at 60 μM has a shorter half-life (7.4 seconds) than **M3** and **T3** with 17.9 and 20.4 minutes, respectively. The short half-life of **C3** could be advantageous as it could provide a surge of CO within a short time frame. Similar to the first and second series photoCORMs, the half-life of the third series compounds increased in the order of $\text{Cr} < \text{Mo} < \text{W}$.

Table 4.21: Half-life ($t_{1/2}$) of C3, M3, and T3 at different concentrations.

Compound	Half-life ($t_{1/2}$)		
	20 (μM)	40 (μM)	60 (μM)
C3	9.1 ± 0.9 secs	8.1 ± 0.7 secs	7.4 ± 0.6 secs
M3	22.1 ± 0.6 mins	19.4 ± 1.5 mins	17.9 ± 0.5 mins
T3	28.2 ± 1.2 mins	25.0 ± 0.6 mins	20.4 ± 1.1 mins

Table 4.22: Number of CO released per molecule of C3, M3, and T3.

Compound	No. of CO released per mol
C3	3.65 ± 0.11
M3	3.71 ± 0.12
T3	3.61 ± 0.09

4.2.5 Half-life of PhotoCORMs C4, M4, and T4

The half-life and number of CO released of the fourth series photoCORMs, namely **C4**, **M4**, and **T4** are shown in Table 4.23 and Table 4.24, respectively. The fourth series photoCORMs are different compared to the aforementioned three series' compounds due to the bimetallic nature of the compounds and the compounds contain eight CO per molecule. The concentration of myoglobin solution used for the fourth series photoCORMs was twice the concentration of the aforementioned series. The compounds displayed an increasing half-life with an increasing compound concentration, which is unusual when compared to the compounds from other series. The half-lives of **C4**, **M4**,

and **T4** at 60 μM are longer than those at 20 μM . Compound **C4** at 20 μM has the shortest half-life (7.4 seconds) compared to **M4** and **T4** with 9.0 and 9.2 minutes, respectively. Both **M4** and **C4** had similar half-life across the three tested concentrations.

Table 4.23: Half-life ($t_{1/2}$) of C4, M4, and T4 at different concentrations.

Compound	Half-life ($t_{1/2}$)		
	20 (μM)	40 (μM)	60 (μM)
C4	10.4 ± 1.2 secs	25.1 ± 1.7 secs	27.8 ± 1.39 secs
M4	9.0 ± 1.2 mins	12.3 ± 0.7 mins	15.8 ± 1.8 mins
T4	9.2 ± 1.4 mins	12.5 ± 0.7 mins	14.9 ± 0.9 mins

Table 4.24: Number of CO released per molecule of C4, M4, and T4.

Compound	No. of CO released per mol
C4	6.47 ± 0.24
M4	6.81 ± 0.17
T4	6.79 ± 0.12

4.2.6 Overall half-life of PhotoCORMs

Overall, **C2** and **C3** in general have the shortest half-life (7.1 ± 0.5 and 7.4 ± 0.6 seconds at $60 \mu\text{M}$ respectively) among all the synthesized photoCORMs, in which both of them (**C2** and **C3**) contained phenolic OH group and chromium metal center. Whereas **M1** and **T1** have the longest half-life (59.7 ± 0.3 and 52.1 ± 0.4 minutes at $20 \mu\text{M}$ respectively). Among all the chromium photoCORMs, **C2** has the shortest half-life whereas **C4** has the longest at $60 \mu\text{M}$. On the other hand, **M2** is the fastest CO-releasing molecule among the molybdenum photoCORMs at $60 \mu\text{M}$, however, at $20 \mu\text{M}$ **M4** has the shortest half-life. Besides that, **T4** is the fastest CO-releasing tungsten photoCORMs among the four series at both 20 and $60 \mu\text{M}$ whereas **T1** is the slowest at $20 \mu\text{M}$. The results suggest that the half-life is more dependent to the type of metal centre for both the mononuclear and binuclear photoCORMs compared with the substituent in the ligand. As for the ligand effect, it seems that ligand **L2** always gives the lowest half-life when the metal centre is fixed at chromium or molybdenum but not for tungsten.

4.3 Dark stability of photoCORMs

The qualitative stability of the photoCORMs were determined using UV-Vis spectrophotometer and ATR-IR. All molybdenum and tungsten photoCORMs, namely **M1**, **T1**, **M2**, **T2**, **M3**, **T3**, **M4**, and **T4** (60 μ M) are stable in 10% DMSO-PBS buffer solution in the dark at 37.5 °C for at least 48 hours. No observable changes were observed in the UV-Vis and IR spectrum within the period of 48 hours. The results were in accordance to the previous studies which suggested that molybdenum and tungsten CORMs are generally stable in aqueous or buffered solution (Pfeiffer et al., 2013; Rimmer et al., 2010).

However, all chromium photoCORMs, namely **C1**, **C2**, **C3**, and **C4** (60 μ M) are not stable in 10% DMSO-PBS buffer solution in the dark at 37.5 °C for 48 hours and the changes in UV-Vis and IR spectra over the period of 48 hours are shown in Figure 4.16, Figure 4.17, Figure 4.18, and Figure 4.19, respectively. The UV-Vis spectra showed that the molar absorptivity of the chromium photoCORMs decreased over the period of 24 and 48 hours which suggest that the compounds slowly degraded in the buffered solution even in the absence of light. The ATR-IR spectra of the chromium photoCORMs showed that the CO stretching peaks in the 1700 – 2100 cm^{-1} region shortened over the period of 24 and 48 hours which suggest that the compounds slowly degraded and released some of the attached COs into the solution. Hence, the results suggest that all chromium photoCORMs regardless of the attached ligands are unstable in the buffered solution in the absence of light.

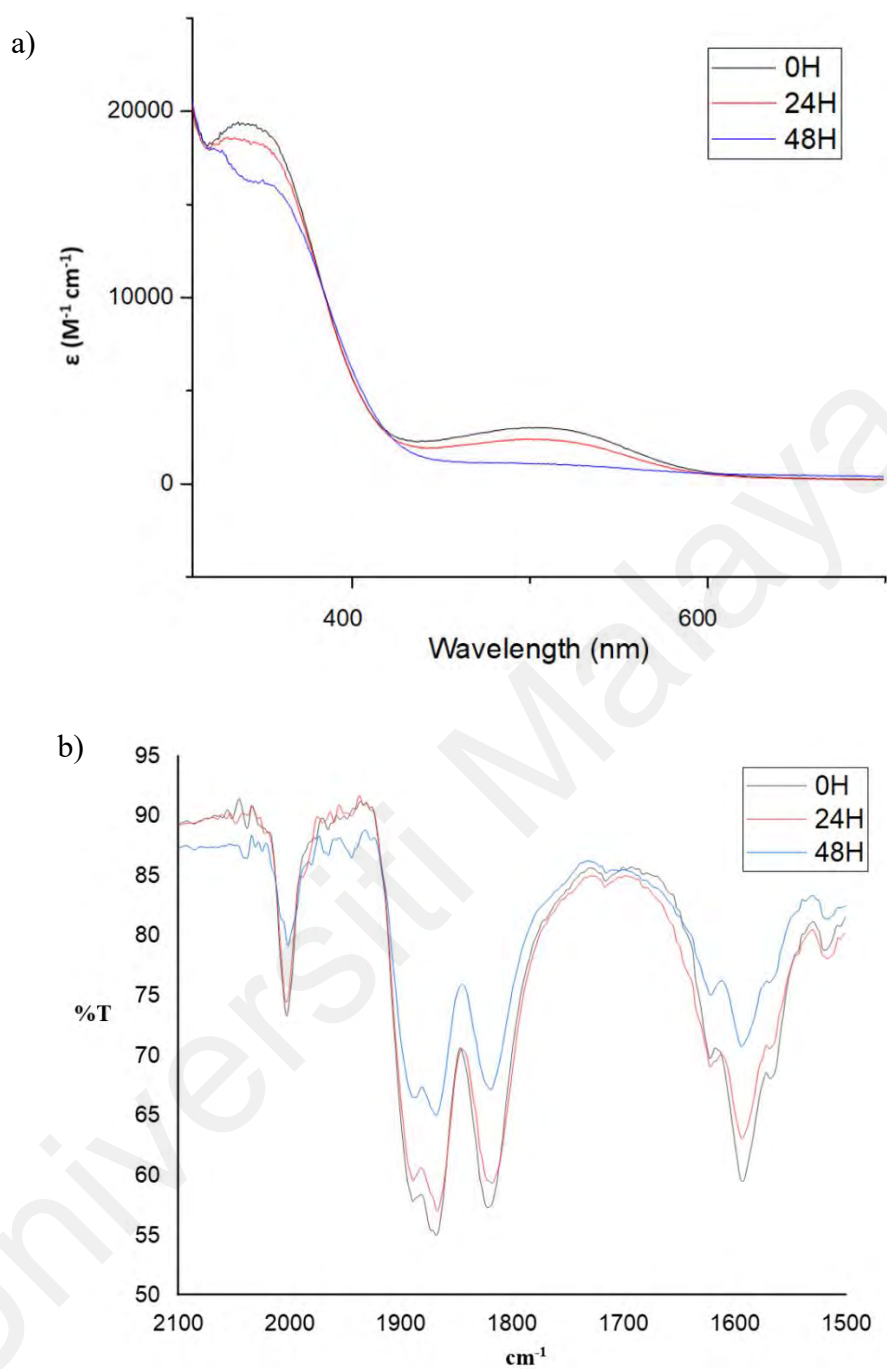


Figure 4.16: a) UV-Vis and b) ATR-IR spectra of C1 (60 μM) in 10% DMSO-PBS buffered solution at 24 and 48 hours.

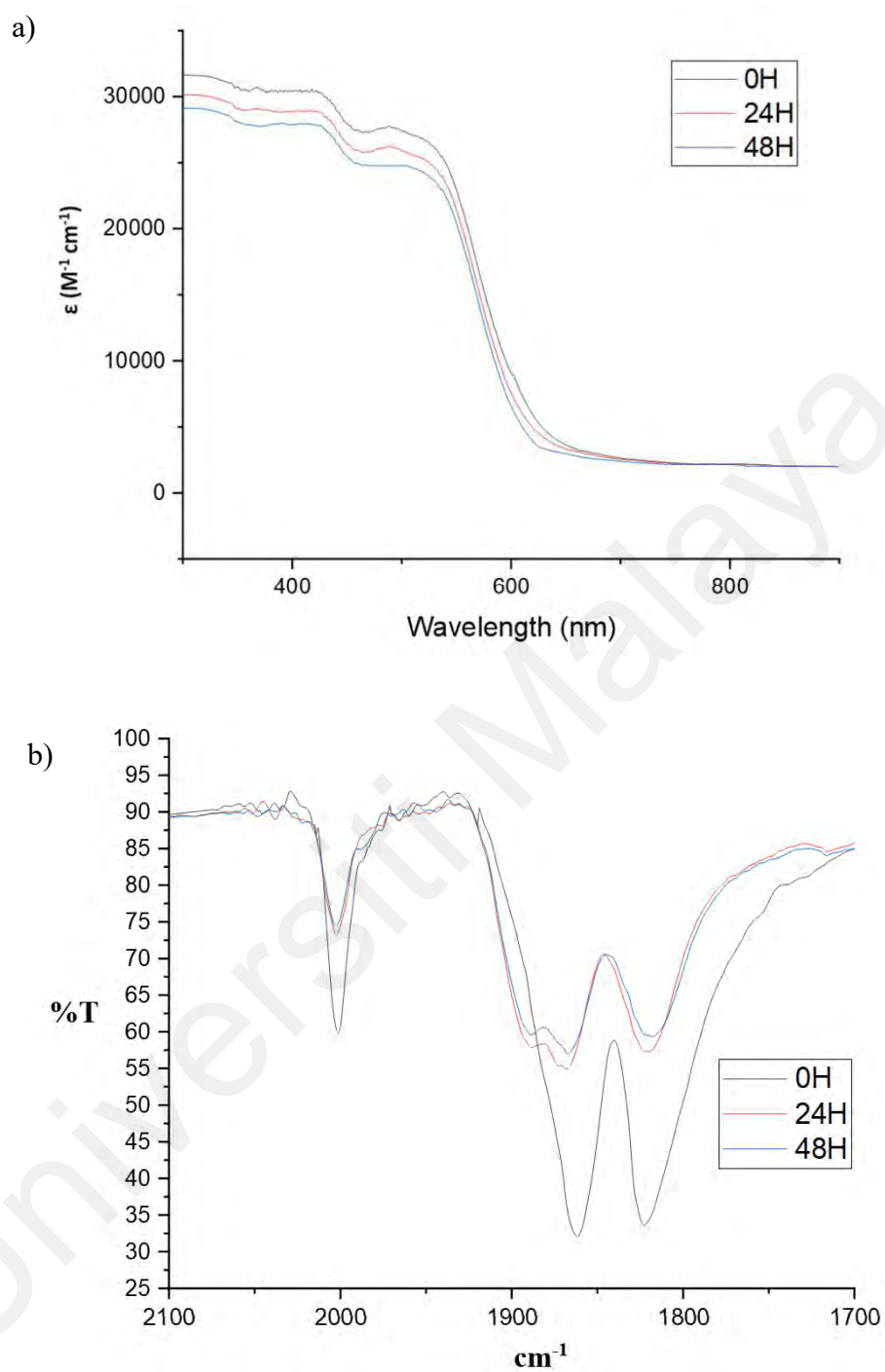


Figure 4.17: a) UV-Vis and b) ATR-IR spectra of C2 (60 μM) in 10% DMSO-PBS buffered solution at 24 and 48 hours.

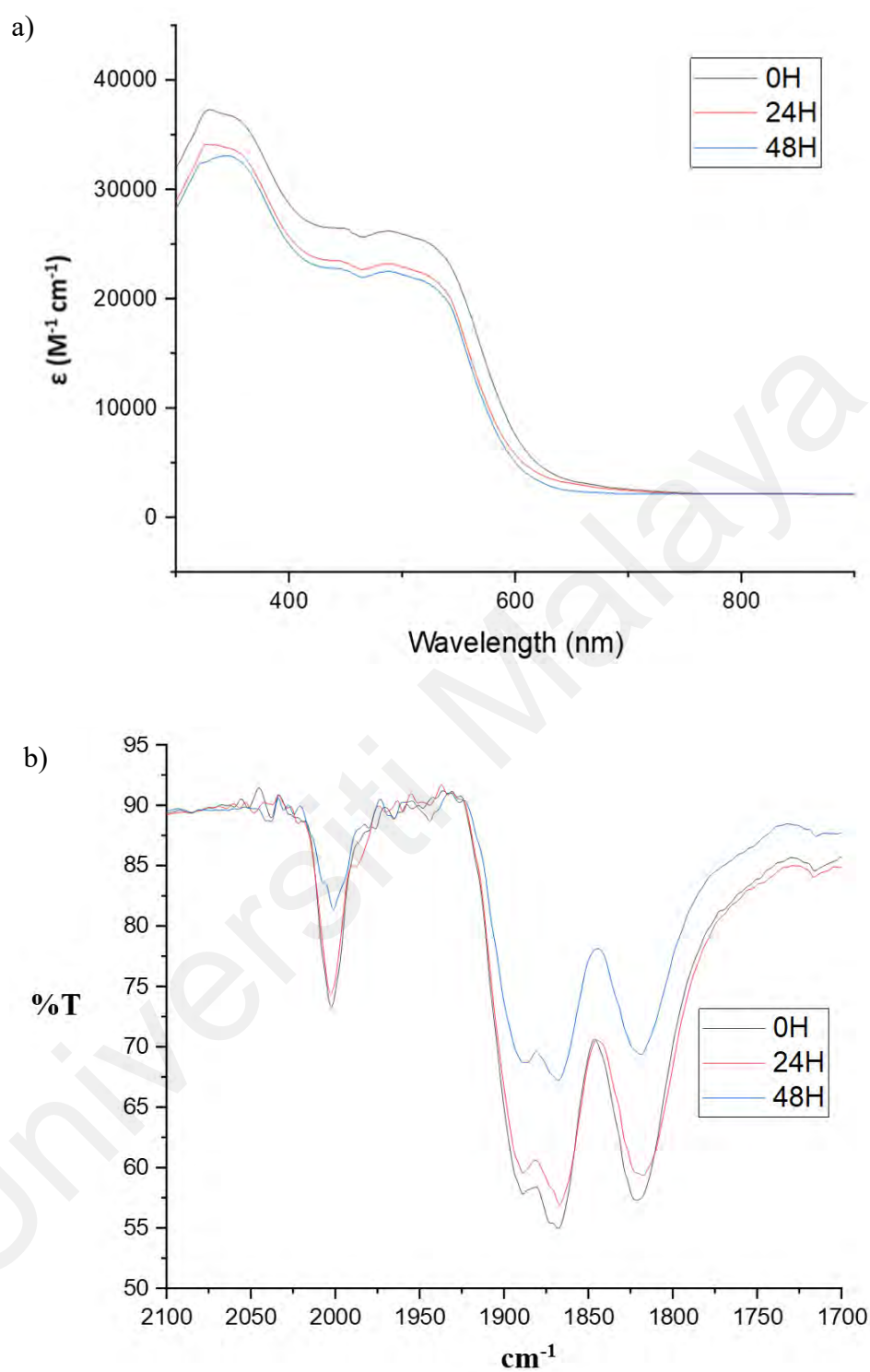


Figure 4.18: a) UV-Vis and b) ATR-IR spectra of C3 (60 μM) in 10% DMSO-PBS buffered solution at 24 and 48 hours.

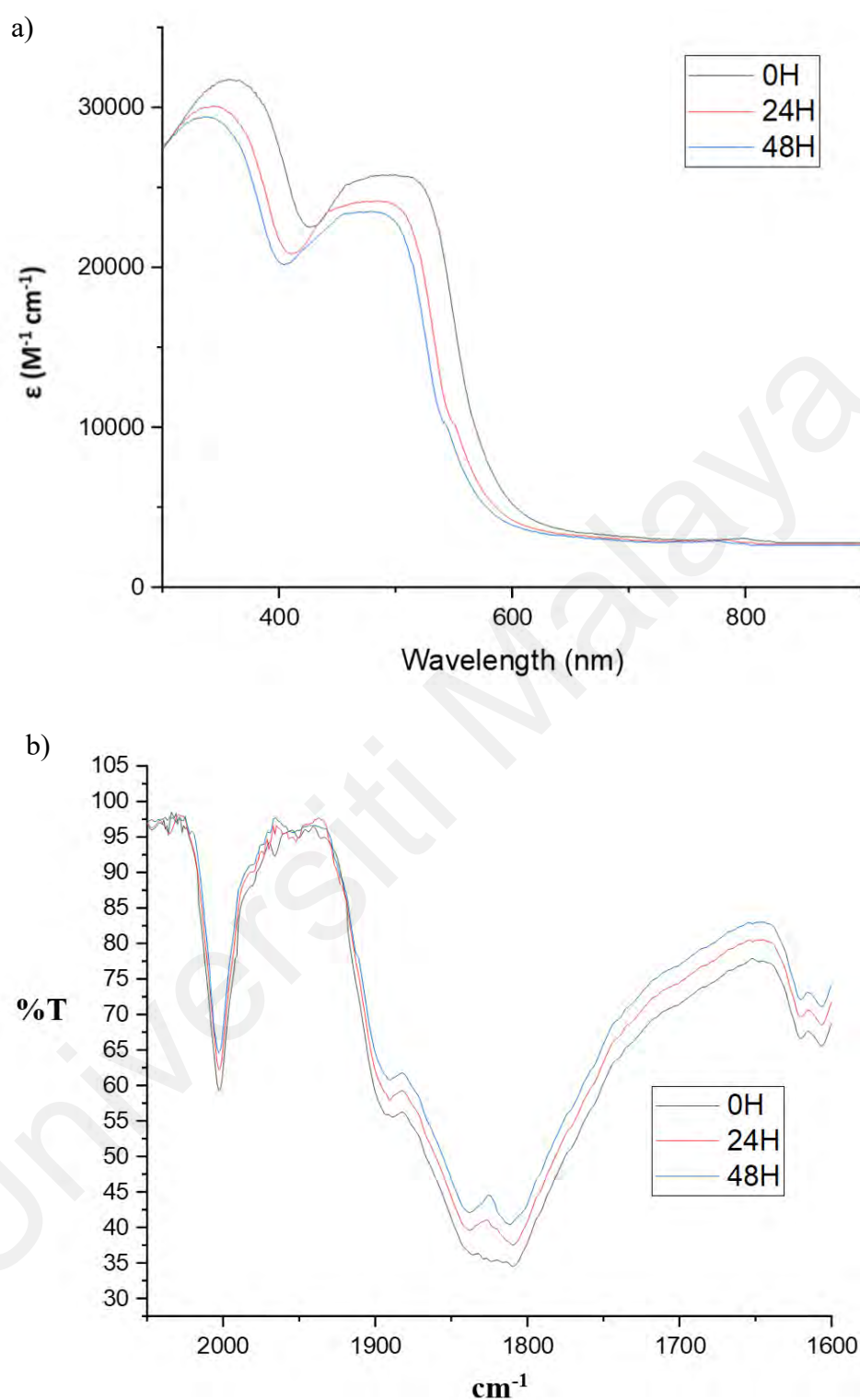


Figure 4.19: a) UV-Vis and b) ATR-IR spectra of C4 (60 μM) in 10% DMSO-PBS buffered solution at 24 and 48 hours.

4.4 Cytotoxic Evaluation

4.4.1 Cytotoxic Evaluation of L1, C1, M1, and T1

The cytotoxicity of the first series compounds, namely **L1**, **C1**, **M1**, and **T1** were evaluated against human colorectal adenocarcinoma (HT-29) and carcinoma (HCT 116) using MTT assay, and the results are shown in Table 4.25. Upon 48 hours of treatment in the absence of UV light illumination, **L1** exhibited pronounced growth inhibitory effect against HT-29 and HCT 116, with IC_{50} of 9.06 and 3.69 μ M, respectively. In contrast, the photoCORMs, **C1**, **M1**, and **T1** exhibited less potent cytotoxicity against both cancer cell lines compared to **L1**, probably due to the larger molecular size of the metal complexes that resulted in a reduction of the cellular uptake. The order of cytotoxicity of the metal complexes against HT-29 was **M1** (15.00 μ M) > **T1** (17.65 μ M) > **C1** (28.36 μ M), with all significantly stronger than cisplatin (IC_{50} 42.55 μ M). The cytotoxicity of the photoCORMs against HCT 116 showed the following order: **M1** (12.68 μ M) > **C1** (17.65 μ M) > **T1** (> 100 μ M), with only **M1** being more cytotoxic than cisplatin (IC_{50} 16.40 μ M). The observation that **M1** has the highest dark toxicity is in accordance with several studies that the molybdenum complexes are naturally cytotoxic towards cancer cells (Hussein et al., 2015; Kirakci et al., 2019).

The MTT assay was repeated by illuminating the treated cell lines with UV light (365 nm) to induce *in situ* CO release, **L1** being a non-photoreactive ligand showed insignificant photo-induced cytotoxicity against HT-29 (IC_{50} 8.64 μ M) and HCT 116 (IC_{50} 2.97 μ M). On the other hand, the photoCORMs, **C1**, **M1**, and **T1** demonstrated remarkable photo-induced cytotoxicity in which the IC_{50} values improved drastically after the UV light illumination. In HT-29, the growth inhibition of **C1**, **M1**, and **T1** had been drastically elevated with IC_{50} values of 18.77 (1.5-fold), 9.18 (1.6-fold), and 12.56 μ M (1.4-fold), respectively. Similarly, the IC_{50} values of the photoCORMs against HCT 116

also greatly enhanced to 12.94 μM (1.4-fold), 5.25 (2.4-fold), and 13.70 (> 7.3 -fold), respectively. Compound **T1** in particular demonstrated the most drastic improvement in the cytotoxicity against HCT 116 after the UV light illumination, i.e., from being inactive ($\text{IC}_{50} > 100 \mu\text{M}$) to become more cytotoxic than cisplatin (IC_{50} 17.78 μM), suggesting that CO release plays a pivotal role in the anti-cancer properties of **T1**.

The effectiveness of chemotherapy is often impeded by various dose-limiting adverse effects due to the lack of selectivity of the chemotherapeutic agents against normal cells, such as cisplatin (Karges et al., 2021). The toxicity of **L1**, **C1**, **M1**, and **T1** were therefore tested against the human normal colon fibroblast CCD18-Co to determine the selectivity of the compounds. From Table 4.25, **L1** showed appreciable cytotoxicity against CCD18-Co (IC_{50} 21.45 μM). On the contrary, **C1** and **T1** were non-cytotoxic ($> 100 \mu\text{M}$), while **M1** showed slight growth-inhibitory against CCD18-Co (IC_{50} 61.67 μM). The exposure of **C1**, **M1**, and **T1** to UV light clearly enhanced the cytotoxicity of **M1** and **T1** with IC_{50} values of 27.48 (2.2-fold) and 79.59 μM (> 1.3 -fold), respectively, while **C1** remained non-cytotoxic ($\text{IC}_{50} > 100 \mu\text{M}$). The calculation of SI provided preliminary insight into the safety of the tested compounds and the results are shown in Table 4.26. Satisfactorily, all non-illuminated and illuminated compounds are classified as highly selective ($\text{SI} > 2$), with all the compounds being more selective than the cisplatin when compared among the same cell line. Generally, the metal complexation has enhanced the selectivity of **C1**, **M1**, and **T1** in HT-29, while the opposite has been observed in HCT 116, indicating that the effect of the metal complexation on the selectivity is dependent on the type of cell line. In the presence of UV light, the selectivity of **C1** and **T1** in HT-29; **C1** and **M1** in HCT 116 were substantially enhanced.

Table 4.25: IC₅₀ value of L1, C1, M1, and T1 against HT-29, HCT 116 and CCD18-Co in the presence and absence of UV light illumination.

IC ₅₀ ± SD (μM)*						
Compound	HT-29		HCT 116		CCD18-Co	
	UV-	UV+	UV-	UV+	UV-	UV+
L1	9.06 ± 0.25	8.64 ± 0.43	3.69 ± 0.24	2.97 ± 0.22	21.45 ± 1.65	20.75 ± 0.47
C1	28.36 ± 0.92	18.77 ± 1.63	17.65 ± 0.86	12.94 ± 1.25	> 100	> 100
M1	15.00 ± 0.41	9.18 ± 0.12	12.68 ± 0.90	5.25 ± 0.28	61.67 ± 1.68	27.48 ± 1.83
T1	17.65 ± 0.01	12.56 ± 0.07	> 100	13.70 ± 0.68	> 100	79.59 ± 2.76
Cisplatin	42.55 ± 0.28	38.91 ± 0.75	16.40 ± 1.33	17.78 ± 1.48	57.94 ± 3.73	60.95 ± 3.19

* Data expressed as mean ± standard deviation of three independent experiments

Table 4.26: Selectivity Index (SI) of L1, C1, M1, and T1 against HT-29, HCT 116 and CCD18-Co in the presence and absence of UV light illumination.

Selectivity Index (SI)				
Compound	HT-29		HCT-116	
	UV-	UV+	UV-	UV+
L1	2.37	2.40	5.81	6.99
C1	3.53	5.33	5.67	7.73
M1	4.11	2.99	4.86	5.23
T1	5.67	6.34	*n.d.	5.81
Cisplatin	1.36	1.57	3.53	3.43

*n.d. indicates that the value was not determined.

4.4.2 Cytotoxic Evaluation of L2, C2, M2, and T2

The cytotoxicity of the second series compounds, namely **L2**, **C2**, **M2**, and **T2** were investigated against two colorectal cancer cell lines (HCT 116 and HT-29) using MTT cytotoxicity assay, and the results are expressed as IC_{50} shown in Table 4.27. After 48 h of treatment in the dark, **L2** potently inhibited the growth of HT-29 at IC_{50} 2.01 μ M. The metal complexation of **L2** to group 6 metal carbonyl to form **M2** considerably decreased the cytotoxicity to 10.37 μ M, while **C2** and **T2** became inactive ($IC_{50} > 100 \mu$ M). Ligand **L2** was also cytotoxic against HCT 116 with an IC_{50} of 3.84 μ M, whereas its metal complexes exhibited a relatively lower growth inhibitory effect. The order of potency of the metal complexes against HCT 116 was **M2** (23.42 μ M) > **T2** (44.91 μ M) > **C2** (51.00 μ M). In both cell lines, **M2** exhibited the highest cytotoxicity among the three complexes.

The observation that **M2** has the highest toxicity without UV correlated well to previous reports that the molybdenum complexes are cytotoxic (Hussein et al., 2015; Kirakci et al., 2019).

The assay was repeated by illuminating the treated cells with UV (365nm) for 20 min to trigger CO releases prior to the incubation for 48 h. The non-UV active **L2** demonstrated insignificant elevation of cytotoxicity against both cell lines (HT-29, 1.55 μM ; HCT 116, 3.27 μM). In contrast, the growth inhibitory activity of the photoCORMs **C2**, **M2** and **T2** against HT-29 and HCT 116 has been substantially enhanced after being exposed to UV during the treatment. Particularly, the cytotoxicity of **C2**, **M2** and **T2** against HT-29 has been increased for at least 3.8-, 1.2-, and 2.6-fold, respectively. In HCT 116, the IC_{50} values of **C2**, **M2** and **T2** were reduced for about 1.6-, 1.9-, and 1.2-fold, respectively, with the cytotoxicity of **M2** (IC_{50} 12.18 μM) being higher than cisplatin (IC_{50} 14.39 μM). The cytotoxicity of these photoCORMs were clearly mediated by the combination of the ligand moiety and the CO released when triggered by UV.

The toxicity of the tested compounds was evaluated using the same assay inclusive of human normal colon fibroblast CCD-18Co. The ligand **L2** was cytotoxic against CCD-18Co (IC_{50} 15.11 μM), while all metal complexes were inactive ($\text{IC}_{50} > 100 \mu\text{M}$). After the UV illumination, only **M2** demonstrated an improvement in cytotoxicity (IC_{50} 79.53 μM). The calculation of selectivity index (SI) implied that all tested compounds are classified as high selectivity ($\text{SI} > 2$), both with and without UV illumination and the values are shown in Table 4.28. Notably, the addition of metals into the ligand has resulted in a higher selectivity, accomplishing our intention of designing the metal complexes with the ability to specifically deliver CO to cancer cells. Lastly, we suggested that the in-depth anti-cancer study on **M2** could be worthwhile as it exhibited the most pronounced cytotoxicity in both colorectal cancer cell lines with the highest selectivity among the other tested compounds, as well as cisplatin.

Table 4.27: IC₅₀ value of L2, C2, M2, and T2 against HT-29, HCT 116 and CCD18-Co in the presence and absence of UV light illumination.

IC ₅₀ ± SD (μM)*						
Compound	HT-29		HCT 116		CCD18-Co	
	UV-	UV+	UV-	UV+	UV-	UV+
L2	3.84 ± 0.19	3.27 ± 0.20	2.01 ± 0.15	1.85 ± 0.06	15.11 ± 0.82	12.80 ± 1.21
C2	51.00 ± 1.55	31.43 ± 0.63	> 100	26.03 ± 2.44	> 100	> 100
M2	23.42 ± 1.86	12.18 ± 0.43	10.37 ± 0.47	8.94 ± 0.42	> 100	79.53 ± 3.34
T2	44.91 ± 1.90	37.00 ± 2.03	> 100	38.03 ± 1.88	> 100	> 100
Cisplatin	14.02 ± 0.25	14.39 ± 0.42	38.91 ± 0.75	44.13 ± 2.04	60.56 ± 7.22	62.63 ± 2.55

* Data expressed as mean ± standard deviation of three independent experiments

Table 4.28: Selectivity Index (SI) of L2, C2, M2, and T2 against HT-29, HCT 116 and CCD18-Co in the presence and absence of UV light illumination.

Selectivity Index (SI)				
Compound	HT-29		HCT-116	
	UV-	UV+	UV-	UV+
L2	3.93	3.91	7.52	8.26
C2	1.96	3.18	1.00	3.84
M2	4.27	6.53	9.64	8.90
T2	2.23	2.70	*n.d.	2.63
Cisplatin	7.13	4.53	2.57	1.42

*n.d. indicates that the value was not determined.

4.4.3 Cytotoxic Evaluation of L3, C3, M3, and T3

The cytotoxicity of the third series compounds, namely **L3**, **C3**, **M3**, and **T3** tested against two colorectal cancer cell lines (HCT 116 and HT-29) are shown in Table 4.29. Similar to the first and second series ligands, **L3** demonstrated appreciable cytotoxicity against HT-29 with an IC_{50} of 16.48 μ M after 48 hours of treatment. However, **M3** showed higher cytotoxicity against HT-29 compared to **L3** with IC_{50} of 12.95 μ M but **T3** showed similar cytotoxicity with **L3** and **C3** showed no cytotoxicity at all. Ligand **L3** was also cytotoxic against HCT 116 with an IC_{50} of 11.01 μ M, whereas its metal complexes exhibited a stronger growth inhibitory effect. The order of potency of the metal complexes against HCT 116 was **T2** (5.49 μ M) > **M2** (7.77 μ M) > **C2** (9.98 μ M). The compounds were also tested against normal human colon fibroblast CCD-18Co in which all photoCORMs

showed no toxicity against the cell line and **L3** showed slight cytotoxicity with an IC_{50} of 91.58 μ M.

Another set of experiment was conducted by illuminating the 96-well microplates using UV handlamp (365 nm) for 20 minutes during the treatment, before incubation for 48 h to determine the potential photo-induced cytotoxicity of **C3**, **M3** and **T3** against HCT 116 and HT-29. The cytotoxicity of non-UV active **L3** did not show significant improvement against HCT 116 and HT-29 with IC_{50} of 12.32 and 14.98 μ M, respectively. The cytotoxicity of photoCORMs against HCT 116 were substantially elevated after exposure to UV, particularly evident in **C3** (from IC_{50} 9.98 to 1.24 μ M, 8.1 fold). The strongest growth inhibitory effect of **C3** observed was in agreement with its shortest CO-releasing half-life among the three photoCORMs. However, the photoCORMs showed no improvement in the cytotoxicity against HT-29 cell line particularly in **C3** which it showed no cytotoxicity at all. The compounds were then tested against normal human colon fibroblast CCD-18Co and the results showed that **M3** exhibited weak cytotoxicity with IC_{50} 67.87 μ M after UV illumination, while the others were non-toxic ($IC_{50} > 100$ μ M). Lastly, the selectivity index (SI) was calculated and shown in Table 4.30 to provide preliminary insight into the cancer cell selectivity of all compounds. The results showed that **C3**, **M3**, and **T3** were selective ($SI > 2$) and the ensuing UV exposure has significantly improved the selectivity against HCT 116 but not for HT-29, indicative of their potential high safety profiles. Generally, **C3** has demonstrated the highest cytotoxicity and selectivity ($SI = 80.65$) towards HCT 116 after UV illumination. Besides, from the stability test demonstrated that **C3** may slowly release CO to the solution in the absent of light and the rate of CO release can be significantly accelerated in the present of UV suggesting that it could be a potential candidate for further anti-cancer investigation.

Table 4.29: IC₅₀ value of L3, C3, M3, and T3 against HT-29, HCT 116 and CCD18-Co in the presence and absence of UV light illumination.

IC ₅₀ ± SD (μM)*						
Compound	HT-29		HCT 116		CCD18-Co	
	UV-	UV+	UV-	UV+	UV-	UV+
L3	16.48 ± 1.41	14.89 ± 0.86	11.01 ± 0.97	12.32 ± 0.63	91.58 ± 6.51	92.7 ± 1.35
C3	> 100	> 100	9.98 ± 0.56	1.24 ± 0.06	> 100	> 100
M3	12.95 ± 0.89	14.52 ± 1.00	7.77 ± 0.20	3.58 ± 0.21	> 100	67.87 ± 3.41
T3	16.56 ± 1.32	22.00 ± 1.33	5.49 ± 0.37	4.39 ± 0.22	> 100	> 100
Cisplatin	48.96 ± 3.58	54.21 ± 3.38	20.56 ± 1.95	20.12 ± 1.03	71.51 ± 3.57	78.46 ± 3.24

* Data expressed as mean ± standard deviation of three independent experiments

Table 4.30: Selectivity Index (SI) of L3, C3, M3, and T3 against HT-29, HCT 116 and CCD18-Co in the presence and absence of UV light illumination.

Selectivity Index (SI)				
Compound	HT-29		HCT-116	
	UV-	UV+	UV-	UV+
L3	5.56	6.23	8.32	7.52
C3	*n.d.	n.d.	10.02	80.65
M3	7.72	4.67	12.87	18.96
T3	6.04	4.55	18.21	22.78
Cisplatin	1.46	1.45	3.48	3.90

*n.d. indicates that the value was not determined.

4.4.4 Cytotoxic Evaluation of L4, C4, M4, and T4

The cytotoxicity of the fourth series compounds were tested against human colorectal adenocarcinoma HT-29 and carcinoma HCT 116, and the results are shown in Table 4.31. In the absence of light, **L4** is moderately active against both HT-29 and HCT 116 cells after 48 h of treatment, with IC_{50} values of 56.80 and 53.08 μ M, respectively. The order of dark cytotoxicity of the photoCORMs was **T4** > **M4** > **C4**, with **T4** being the most cytotoxic against HT-29 and HCT 116 with IC_{50} = 26.68 μ M and 24.03 μ M, respectively, while **C4** was non-cytotoxic in both cell lines.

In a parallel experiment, cells were treated with the same compounds and illuminated with UV light at 365 nm for 20 minutes prior to 48 hours of incubation. The exposure of the photoCORMs to UV light has substantially enhanced their cytotoxicity against both

cell lines. The order of photocytotoxicity of the photoCORMs was identical to that without UV illumination, with **T4** also being the most cytotoxic against HT-29 and HCT 116 with IC_{50} 7.02 μ M and 3.75 μ M, respectively. Moreover, **T4** has shown the most improvement in cytotoxicity, with \sim 4-fold in HT-29 and \sim 7-fold in HCT 116 despite being the slowest CO releasing compound in the series. These results suggested that the inhibition of cancer cell growth was a direct consequence of exposure of the cells to the photoCORMs in the presence of UV light.

The toxicity of the compounds were tested against normal human colon fibroblast CCD18-Co to provide an insight into their cancer cell selectivity profile. Aside from **T4**, which is weakly cytotoxic with $IC_{50} > 90$ μ M, the others are generally non-cytotoxic with $IC_{50} > 100$ μ M in the absence and presence of UV. Since a tested compound is considered selective when $SI > 2$, the fourth series photoCORMs are therefore characterized by appreciable selectivity and the SI values are shown in Table 4.32 (Desai et al., 2020b). Lastly, it is noteworthy that the UV illumination on **T4** has tremendously improved its selectivity against HT-29 and HCT 116 with $SI = 13.44$ and 25.16 , respectively. In general, **T4** can be considered as a potential photochemotherapeutic candidate for further anti-cancer studies, due to its potent cytotoxicity and high selectivity after exposure to UV light.

Table 4.31: IC₅₀ value of L4, C4, M4, and T4 against HT-29, HCT 116 and CCD18-Co in the presence and absence of UV light illumination.

IC ₅₀ ± SD (μM)*						
Compound	HT-29		HCT 116		CCD18-Co	
	UV-	UV+	UV-	UV+	UV-	UV+
L4	56.80 ± 5.47	56.58 ± 4.39	53.08 ± 2.92	58.56 ± 4.10	> 100	> 100
C4	> 100	46.44 ± 1.93	> 100	44.79 ± 3.97	> 100	> 100
M4	39.08 ± 1.10	15.38 ± 0.47	38.48 ± 1.90	11.18 ± 0.79	> 100	> 100
T4	26.68 ± 0.79	7.02 ± 0.20	24.03 ± 2.46	3.75 ± 0.07	93.85 ± 0.37	94.36 ± 0.15
Cisplatin	41.44 ± 0.98	39.50 ± 2.91	22.08 ± 1.69	23.79 ± 0.80	68.89 ± 5.88	72.50 ± 3.11

* Data expressed as mean ± standard deviation of three independent experiments

Table 4.32: Selectivity Index (SI) of L4, C4, M4, and T4 against HT-29, HCT 116 and CCD18-Co in the presence and absence of UV.

Selectivity Index (SI)				
Compound	HT-29		HCT 116	
	UV-	UV+	UV-	UV+
L4	1.76	2.90	1.88	1.71
C4	*n.d.	2.15	n.d.	2.23
M4	2.56	6.50	2.60	8.94
T4	3.52	13.44	3.91	25.16
Cisplatin	1.66	1.84	3.12	3.05

*n.d. indicates that the value was not determined.

4.4.5 Overall Cytotoxic Result

The overall MTT result suggests that third series compounds, namely **L3**, **C3**, **M3**, and **T3** are the most cytotoxic series against HCT 116 cell lines in the absence and presence of UV light. Whereas the first series compounds namely **L1**, **C1**, **M1**, and **T1** are the most cytotoxic series against HT-29 cell line in the absence and presence of UV light. Among all the ligands, the second series ligand, **L2** is the most cytotoxic against HCT 116 and HT-29 cell lines where as **L4** is the least cytotoxic with cytotoxicity increase in the order of **L4** < **L3** < **L1** < **L2**. As for the photoCORMS, in the presence of UV light, **C3** is the most cytotoxic against HCT 116 cell line and **M1** is the most cytotoxic against HT-29.

In terms of the chromium photoCORMs, **C3** is the most cytotoxic compound against HCT 116 cell line in the absence and presence of UV. Whereas **C1** is the most cytotoxic compound against HT-29 cell line in the absence and presence of UV. Among the four molybdenum photoCORMs, **M3** is the most cytotoxic compound against HCT 116 cell line in both conditions, whereas **M1** is the most cytotoxic compound against HT-29. Lastly, among the tungsten photoCORMs **T3** has the highest cytotoxicity against HCT 116 cell line and **T1** has the highest cytotoxicity against HT-29 cell lines in the absence and presence of UV.

Taken together, the results imply that complexation can bestowed the photoCORMs with superior antiproliferative activities. On top of that, it is noteworthy that the most potent photoCORMs (**M1 and C3**) are not derived from the most potent ligand, **L2**. Although the fourth series photoCORMs, namely **C4, M4 and T4** are able to release twice the amount of CO compared to rest of the series, but the ability has no impact on the cytotoxicity against the tested cancer cells due to the fact that CO alone is not an anticancer agent and instead it only enhances the cancer cells' sensitivity towards the anticancer compounds (Kawahara et al., 2020).

4.5 Antimicrobial Study

4.5.1 Antimicrobial activity of L1, C1, M1, and T1

The antimicrobial activity of the first series compounds, namely **L1**, **C1**, **M1**, and **T1** were evaluated against 15 different strains of bacteria and fungi, and the results were expressed in MIC and MBC values (Table 4.33 and Table 4.34). Under the dark condition, the results showed that the tested compounds were generally inactive against most of the bacteria and fungi (MIC and MBC > 100 mg/ml). Only **C1** exhibited pronounced antifungal activity (MIC = 25 mg/ml) against the clinical isolate of *C. albicans* and *C. tropicalis*, while a relatively weak antibacterial activity (MIC = 100 mg/ml) was found when tested against *B. cereus*, *B. subtilis*, methicillin-resistant *S. aureus* (ATCC 43300 and 33519), and *E. coli*. Compound **M1**, however, was weakly inhibiting the growth of *B. cereus*, with a MIC of 100 mg/ml. In addition, only compound **C1** demonstrated marginal fungicidal effect against *C. albicans* and *C. tropicalis* isolates (MBC = 50 mg/ml), and weak bactericidal activity against *B. cereus* (MBC = 100 mg/ml). The assays were repeated by illuminating the treated microbes with UV light (365nm) for 20 minutes using UV handlamp before the incubation period. The results obtained were identical to those without UV illumination, indicating that the CO released -by the photoactivation did not contribute significantly to the antimicrobial activity of the first series compounds.

The first series photoCORMs generally showed no antimicrobial activity except for **C1**. The possible explanation to the slight antimicrobial activity of **C1** could be due to the lower molecular weight that facilitate the penetration across the cell membrane, causing higher intoxication within the cells regardless of the presence of CO (Matuszewska et al., 2018). Although the molecular weight of **L1** is lower than **C1**, the former was inactive towards all microbes tested, probably due to its insolubility in aqueous media (Aiassa et al., 2016). Besides molecular weight, both Mo and W are essential elements for the

survival of microorganisms especially bacteria, the high MIC and MBC value of **M1** and **T1** could be due to the beneficial effects of Mo and W surpassing the toxicity of CO at the concentrations used in this experiment (Mendel, 2005; Romão, 2009).

Table 4.33 : MIC value for L1, C1, M1, and T1 against a series of microbes.

Microbes	MIC (mg/mL)			
	L1	C1	M1	T1
<i>Bacillus cereus</i> ATCC 14579	>100	100	100	>100
<i>Bacillus subtilis</i> ATCC 8188	>100	100	>100	>100
<i>Enterococcus faecalis</i> ATCC 29212	>100	>100	>100	>100
VRE ATCC 700802	>100	>100	>100	>100
Methicillin-sensitive <i>S. aureus</i> ATCC 29213	>100	>100	>100	>100
Methicillin-sensitive <i>S. aureus</i> ATCC 33591	>100	>100	>100	>100
Methicillin-resistant <i>S. aureus</i> ATCC 43300	>100	100	>100	>100
Methicillin-resistant <i>S. aureus</i> ATCC 33519	>100	100	>100	>100
<i>Escherichia coli</i> ATCC 25922	>100	100	>100	>100
<i>Pseudomonas aeruginosa</i> ATCC 10145	>100	>100	>100	>100
<i>Klebsiella pneumoniae</i> ATCC 10031	>100	>100	>100	>100
<i>Shigella flexneri</i> ATCC 12022	>100	>100	>100	>100
<i>Candida albicans</i> IMR	>100	>100	>100	>100
<i>Candida albicans</i> clinical isolate	>100	25	>100	>100
<i>Candida tropicalis</i> clinical isolate	>100	25	>100	>100

Table 4.34: MBC value for L1, C1, M1, and T1 against a series of microbes.

Microbes	MBC (mg/mL)			
	L1	C1	M1	T1
<i>Bacillus cereus</i> ATCC 14579	>100	100	>100	>100
<i>Bacillus subtilis</i> ATCC 8188	>100	>100	>100	>100
<i>Enterococcus faecalis</i> ATCC 29212	>100	>100	>100	>100
VRE ATCC 700802	>100	>100	>100	>100
Methicillin-sensitive <i>S. aureus</i> ATCC 29213	>100	>100	>100	>100
Methicillin-sensitive <i>S. aureus</i> ATCC 33591	>100	>100	>100	>100
Methicillin-resistant <i>S. aureus</i> ATCC 43300	>100	>100	>100	>100
Methicillin-resistant <i>S. aureus</i> ATCC 33519	>100	>100	>100	>100
<i>Escherichia coli</i> ATCC 25922	>100	>100	>100	>100
<i>Pseudomonas aeruginosa</i> ATCC 10145	>100	>100	>100	>100
<i>Klebsiella pneumoniae</i> ATCC 10031	>100	>100	>100	>100
<i>Shigella flexneri</i> ATCC 12022	>100	>100	>100	>100
<i>Candida albicans</i> IMR	>100	>100	>100	>100
<i>Candida albicans</i> clinical isolate	>100	50	>100	>100
<i>Candida tropicalis</i> clinical isolate	>100	50	>100	>100

4.5.2 Antimicrobial activity of L2, C2, M2, and T2

The antimicrobial activity of second series compounds, namely **L2**, **C2**, **M2**, and **T2** were evaluated against 15 different strains of bacteria and fungi. The results reported were expressed in minimum inhibitory concentration (MIC) and minimum bactericidal concentration (MBC) values in the absence and presence of UV light (365 nm) illumination. The MIC value of the compounds in the absence and presence of UV are shown in Table 4.35 and Table 4.36, respectively. Similarly, the MBC value of the compounds in the absence and presence of UV are shown in Table 4.37 and Table 4.38, respectively.

In the absence of UV light, most of the compounds were inactive in inhibiting the growth of the bacteria and fungi except for the ligand, **L2**. Compound **L2** showed exceptional growth inhibition activity against *B. cereus*, *B. subtilis*, *E. coli*, *K. pneumoniae*, and Methicillin-sensitive *S. aureus* (ATCC 29213, ATCC 33591, ATCC 43300, and ATCC 33519) with MIC value of 3.13, 6.25, 25, 12.50, 6.25, 25, 6.25, and 6.25 mg/ml, respectively. In terms of bactericidal activity, the photoCORMs **C2**, **M2**, and **T2** were inactive against all of the tested bacteria and fungi strains when UV light is absent. However, **L2** demonstrated strong bactericidal activity against *B. cereus*, *B. subtilis*, *E. faecalis*, and Methicillin-sensitive *S. aureus* (ATCC 29213, ATCC 33591, ATCC 43300, and ATCC 33519) with MBC value of 25, 25, 25, 25, 50, 25 and 12.50 mg/ml, respectively.

In the presence of UV light illumination, the growth inhibition and bactericidal activity of ligand **L2** remained unchanged. However, photoCORMs **C2**, **M2**, and **T2** showed improvements in the growth inhibition activity against *B. cereus*, *B. subtilis*, *E. coli*, *K. pneumoniae* Methicillin-sensitive *S. aureus* (ATCC 29213, ATCC 33591, ATCC 43300, and ATCC 33519), and *S. flexneri* with **C2** demonstrated the strongest improvement

among the three photoCORMs possibly due to its short half-life which allow **C2** to release a surge of CO in a short period of time. In contrast, only slight improvement was observed in the bactericidal activity of **C2**, **M2**, and **T2** against *K. pneumoniae* and Methicillin-sensitive *S. aureus* (ATCC 29213, ATCC 33591, ATCC 43300, and ATCC 33519). From the results, the ligand **L2** is the better antimicrobial agent, however the complexation of **L2** to chromium, molybdenum and tungsten carbonyl significantly reduced its efficacy against the tested bacteria and fungi and the CO releasing ability of **C2**, **M2**, and **T2** are insufficient to compensate for the loss of activity.

Table 4.35: MIC value for L2, C2, M2, and T2 against a series of microbes in the absence of UV light.

Microbes	MIC (mg/mL)			
	L2	C2	M2	T2
<i>Bacillus cereus</i> ATCC 14579	3.13	>100	>100	>100
<i>Bacillus subtilis</i> ATCC 8188	6.25	>100	>100	>100
<i>Enterococcus faecalis</i> ATCC 29212	50	>100	>100	>100
VRE ATCC 700802	50	>100	>100	>100
Methicillin-sensitive <i>S. aureus</i> ATCC 29213	6.25	>100	>100	>100
Methicillin-sensitive <i>S. aureus</i> ATCC 33591	25	>100	>100	>100
Methicillin-resistant <i>S. aureus</i> ATCC 43300	6.25	>100	>100	>100
Methicillin-resistant <i>S. aureus</i> ATCC 33519	6.25	>100	>100	>100
<i>Escherichia coli</i> ATCC 25922	25	>100	>100	>100
<i>Pseudomonas aeruginosa</i> ATCC 10145	>100	>100	>100	>100
<i>Klebsiella pneumoniae</i> ATCC 10031	12.50	>100	>100	>100
<i>Shigella flexneri</i> ATCC 12022	>100	>100	>100	>100
<i>Candida albicans</i> IMR	>100	>100	>100	>100
<i>Candida albicans</i> clinical isolate	>100	>100	>100	>100
<i>Candida tropicalis</i> clinical isolate	>100	>100	>100	>100

Table 4.36: MIC value for L2, C2, M2, and T2 against a series of microbes in the presence of UV light.

Microbes	MIC (mg/mL)			
	L2	C2	M2	T2
<i>Bacillus cereus</i> ATCC 14579	3.13	12.50	25	25
<i>Bacillus subtilis</i> ATCC 8188	6.25	12.50	25	25
<i>Enterococcus faecalis</i> ATCC 29212	50	50	>100	>100
VRE ATCC 700802	50	>100	>100	>100
Methicillin-sensitive <i>S. aureus</i> ATCC 29213	6.25	25	50	50
Methicillin-sensitive <i>S. aureus</i> ATCC 33591	25	50	50	100
Methicillin-resistant <i>S. aureus</i> ATCC 43300	6.25	25	50	50
Methicillin-resistant <i>S. aureus</i> ATCC 33519	6.25	25	50	>100
<i>Escherichia coli</i> ATCC 25922	25	50	50	100
<i>Pseudomonas aeruginosa</i> ATCC 10145	>100	>100	>100	>100
<i>Klebsiella pneumoniae</i> ATCC 10031	12.50	25	50	50
<i>Shigella flexneri</i> ATCC 12022	>100	50	100	100
<i>Candida albicans</i> IMR	>100	>100	>100	>100
<i>Candida albicans</i> clinical isolate	>100	>100	>100	>100
<i>Candida tropicalis</i> clinical isolate	>100	>100	>100	>100

Table 4.37: MBC value for L2, C2, M2, and T2 against a series of microbes in the absence of UV light.

Microbes	MBC (mg/mL)			
	L2	C2	M2	T2
<i>Bacillus cereus</i> ATCC 14579	25	>100	>100	>100
<i>Bacillus subtilis</i> ATCC 8188	25	>100	>100	>100
<i>Enterococcus faecalis</i> ATCC 29212	25	>100	>100	>100
VRE ATCC 700802	>100	>100	>100	>100
Methicillin-sensitive <i>S. aureus</i> ATCC 29213	25	>100	>100	>100
Methicillin-sensitive <i>S. aureus</i> ATCC 33591	50	>100	>100	>100
Methicillin-resistant <i>S. aureus</i> ATCC 43300	25	>100	>100	>100
Methicillin-resistant <i>S. aureus</i> ATCC 33519	12.50	>100	>100	>100
<i>Escherichia coli</i> ATCC 25922	>100	>100	>100	>100
<i>Pseudomonas aeruginosa</i> ATCC 10145	>100	>100	>100	>100
<i>Klebsiella pneumoniae</i> ATCC 10031	>100	>100	>100	>100
<i>Shigella flexneri</i> ATCC 12022	>100	>100	>100	>100
<i>Candida albicans</i> IMR	>100	>100	>100	>100
<i>Candida albicans</i> clinical isolate	>100	>100	>100	>100
<i>Candida tropicalis</i> clinical isolate	>100	>100	>100	>100

Table 4.38: MBC value for L2, C2, M2, and T2 against a series of microbes in the presence of UV light.

Microbes	MBC (mg/mL)			
	L2	C2	M2	T2
<i>Bacillus cereus</i> ATCC 14579	25	>100	>100	>100
<i>Bacillus subtilis</i> ATCC 8188	25	>100	>100	>100
<i>Enterococcus faecalis</i> ATCC 29212	25	>100	>100	>100
VRE ATCC 700802	>100	>100	>100	>100
Methicillin-sensitive <i>S. aureus</i> ATCC 29213	25	50	100	100
Methicillin-sensitive <i>S. aureus</i> ATCC 33591	50	50	>100	>100
Methicillin-resistant <i>S. aureus</i> ATCC 43300	25	50	50	100
Methicillin-resistant <i>S. aureus</i> ATCC 33519	12.50	25	50	50
<i>Escherichia coli</i> ATCC 25922	>100	>100	>100	>100
<i>Pseudomonas aeruginosa</i> ATCC 10145	>100	>100	>100	>100
<i>Klebsiella pneumoniae</i> ATCC 10031	>100	50	100	100
<i>Shigella flexneri</i> ATCC 12022	>100	>100	>100	>100
<i>Candida albicans</i> IMR	>100	>100	>100	>100
<i>Candida albicans</i> clinical isolate	>100	>100	>100	>100
<i>Candida tropicalis</i> clinical isolate	>100	>100	>100	>100

4.5.3 Antimicrobial activity of L3, C3, M3, and T3

The antimicrobial activity of the third series compounds, namely **L3**, **C3**, **M3**, and **T3** were evaluated against 15 different strains of bacteria and fungi, and the results are expressed in minimum inhibitory concentration (MIC) and minimum bactericidal concentration (MBC) values. The MIC value of the compounds in the absence and presence of UV are shown in Table 4.39 and Table 4.40, respectively. Similarly, the MBC value of the compounds in the absence and presence of UV are shown at Table 4.41 and Table 4.42, respectively.

In the absence of UV, all compounds were generally non-active in inhibiting the growth of most of the bacteria and fungi, viz., *B. cereus*, *B. subtilis*, *C. albicans* (IMR and clinical isolate), *C. tropicalis*, *E. faecalis*, methicillin-resistant *S. aureus* (ATCC 29213, 33519, 33591, and 43300), *P. aeruginosa*, and VRE with MIC \geq 50 mg/ml. However, ligand **L3** showed substantial activity against *B. cereus*, *B. subtilis*, *E. coli*, *K. pneumoniae*, and *S. flexneri* with MIC \leq 12.5 mg/ml. The activity of **L3** in the absence of UV can be attributed to the presence of hydroxyl group and phenanthroline N–N in the structure, which improved its solubility in water and therefore inhibiting the growth of the microbes. The complexation of **L3** into the three metal carbonyls to form the three photoCORMs caused a decrease in water solubility and the loss of phenanthroline N–N site for **C3**, **M3**, and **T3**, which may have caused a significant decrease in inhibitory effect against most microbes tested. Similarly, all compounds did not show bactericidal activity against all of the microbes tested, except for **L3** that displayed slight activity with MBC = 25 mg/ml against *S. flexneri*.

In the presence of UV light illumination, the growth inhibitory effect of ligand **L3** remained unchanged for all microbes tested. Nonetheless, all three photoCORMs have shown significant improvement in the growth inhibitory effect against *B. cereus*, *B.*

subtilis, *C. albicans*, *C. tropicalis*, *E. coli*, *K. pneumoniae*, methicillin-sensitive *S. aureus* (ATCC 29213, 33591, and 33519), and *S. flexneri*. It is interesting to note that the MIC value of **C3** elevated substantially against *B. cereus* and *B. subtili* with MIC = 12.50 mg/ml and **T3** also improves drastically against *E. coli* and *K. pneumoniae* with MIC = 12.50 mg/ml, while **M3** did not show appreciable changes to the effect. The bactericidal activity of **C3**, **M3**, and **T3** showed notable enhancement against *S. flexneri*, but no breakthrough against the rest of the bacteria and fungi. Only **C3** showed strong improvement against *S. flexneri*, *C. tropicalis*, *E. coli*, and *K. pneumoniae* with MBC = 25 mg/ml after exposure to UV.

Table 4.39: MIC value for L3, C3, M3, and T3 against a series of microbes in the absence of UV light.

Microbes	MIC (mg/mL)			
	L3	C3	M3	T3
<i>Bacillus cereus</i> ATCC 14579	12.50	100	50	>100
<i>Bacillus subtilis</i> ATCC 8188	12.50	100	50	>100
<i>Enterococcus faecalis</i> ATCC 29212	>100	>100	>100	>100
VRE ATCC 700802	>100	>100	>100	>100
Methicillin-sensitive <i>S. aureus</i> ATCC 29213	100	>100	>100	>100
Methicillin-sensitive <i>S. aureus</i> ATCC 33591	100	>100	>100	>100
Methicillin-resistant <i>S. aureus</i> ATCC 43300	100	>100	>100	>100
Methicillin-resistant <i>S. aureus</i> ATCC 33519	100	>100	>100	>100
<i>Escherichia coli</i> ATCC 25922	6.25	50	25	100
<i>Pseudomonas aeruginosa</i> ATCC 10145	>100	>100	>100	>100
<i>Klebsiella pneumoniae</i> ATCC 10031	12.50	50	25	>100
<i>Shigella flexneri</i> ATCC 12022	12.50	100	50	>100
<i>Candida albicans</i> IMR	50	100	100	>100
<i>Candida albicans</i> clinical isolate	50	100	100	>100
<i>Candida tropicalis</i> clinical isolate	100	100	>100	>100

Table 4.40: MIC value for L3, C3, M3, and T3 against a series of microbes in the presence of UV light.

Microbes	MIC (mg/mL)			
	L3	C3	M3	T3
<i>Bacillus cereus</i> ATCC 14579	12.50	12.50	25	25
<i>Bacillus subtilis</i> ATCC 8188	12.50	12.50	25	25
<i>Enterococcus faecalis</i> ATCC 29212	>100	>100	>100	>100
VRE ATCC 700802	>100	>100	>100	>100
Methicillin-sensitive <i>S. aureus</i> ATCC 29213	100	50	50	50
Methicillin-sensitive <i>S. aureus</i> ATCC 33591	100	25	50	25
Methicillin-resistant <i>S. aureus</i> ATCC 43300	100	100	>100	>100
Methicillin-resistant <i>S. aureus</i> ATCC 33519	100	100	50	>100
<i>Escherichia coli</i> ATCC 25922	6.25	50	25	12.50
<i>Pseudomonas aeruginosa</i> ATCC 10145	>100	>100	>100	>100
<i>Klebsiella pneumoniae</i> ATCC 10031	12.50	50	25	12.50
<i>Shigella flexneri</i> ATCC 12022	12.50	50	25	25
<i>Candida albicans</i> IMR	50	100	50	50
<i>Candida albicans</i> clinical isolate	50	100	100	100
<i>Candida tropicalis</i> clinical isolate	100	25	100	100

Table 4.41: MBC value for L3, C3, M3, and T3 against a series of microbes in the absence of UV light.

Microbes	MBC (mg/mL)			
	L3	C3	M3	T3
<i>Bacillus cereus</i> ATCC 14579	100	>100	>100	>100
<i>Bacillus subtilis</i> ATCC 8188	100	>100	>100	>100
<i>Enterococcus faecalis</i> ATCC 29212	>100	>100	>100	>100
VRE ATCC 700802	>100	>100	>100	>100
Methicillin-sensitive <i>S. aureus</i> ATCC 29213	100	>100	>100	>100
Methicillin-sensitive <i>S. aureus</i> ATCC 33591	100	>100	>100	>100
Methicillin-resistant <i>S. aureus</i> ATCC 43300	>100	>100	>100	>100
Methicillin-resistant <i>S. aureus</i> ATCC 33519	>100	>100	>100	>100
<i>Escherichia coli</i> ATCC 25922	>100	100	50	100
<i>Pseudomonas aeruginosa</i> ATCC 10145	>100	>100	>100	>100
<i>Klebsiella pneumoniae</i> ATCC 10031	>100	100	>100	>100
<i>Shigella flexneri</i> ATCC 12022	25	100	100	>100
<i>Candida albicans</i> IMR	100	100	100	>100
<i>Candida albicans</i> clinical isolate	>100	100	100	>100
<i>Candida tropicalis</i> clinical isolate	>100	100	>100	>100

Table 4.42: MBC value for L3, C3, M3, and T3 against a series of microbes in the presence of UV light.

Microbes	MBC (mg/mL)			
	L3	C3	M3	T3
<i>Bacillus cereus</i> ATCC 14579	100	100	>100	>100
<i>Bacillus subtilis</i> ATCC 8188	100	>100	100	>100
<i>Enterococcus faecalis</i> ATCC 29212	>100	>100	>100	>100
VRE ATCC 700802	>100	>100	>100	>100
Methicillin-sensitive <i>S. aureus</i> ATCC 29213	100	>100	>100	>100
Methicillin-sensitive <i>S. aureus</i> ATCC 33591	100	>100	>100	>100
Methicillin-resistant <i>S. aureus</i> ATCC 43300	>100	>100	>100	>100
Methicillin-resistant <i>S. aureus</i> ATCC 33519	>100	>100	>100	>100
<i>Escherichia coli</i> ATCC 25922	>100	25	50	100
<i>Pseudomonas aeruginosa</i> ATCC 10145	>100	>100	>100	>100
<i>Klebsiella pneumoniae</i> ATCC 10031	>100	25	100	100
<i>Shigella flexneri</i> ATCC 12022	25	25	50	100
<i>Candida albicans</i> IMR	100	100	100	>100
<i>Candida albicans</i> clinical isolate	>100	100	100	>100
<i>Candida tropicalis</i> clinical isolate	>100	25	100	100

4.5.4 Antimicrobial activity of L4, C4, M4, and T4

The antimicrobial activity of the fourth series compounds, namely **L4**, **C4**, **M4**, and **T4** were evaluated against 15 different strains of bacteria and fungi, and the results were expressed in MIC and MBC values shown in Table 4.43 and Table 4.44, respectively. All the photoCORMs, namely **C4**, **M4**, and **T4** showed no antimicrobial activity against all the tested microbes and the compounds also showed no photo-induced antimicrobial activities despite their ability to release more than 6 COs, almost twice as much as the first three series photoCORMs when UV light is presence. However, ligand **L4** showed notable growth inhibitory effects against *B. cereus*, *B. subtilis*, *E. coli*, *E. faecalis*, *K. pneumoniae*, methicillin-resistant *S. aureus* (ATCC 29213, 33519, 33591, and 43300), and VRE. Besides, **L4** also showed significant bactericidal activities against *B. cereus*, *B. subtilis*, *E. faecalis*, methicillin-resistant *S. aureus* (ATCC 29213, 33519, 33591), and VRE. The loss of activities of the photoCORMs **C4**, **M4**, and **T4** may be attributed their high molecular weight (**C4** = 816.02 g/mol, **M4** = 907.95 g/mol, and **T4** = 1080.04 g/mol) which significantly lower their water solubility and thereby hinder their ability to penetrate the cell membranes (Matuszewska et al., 2018).

Table 4.43: MIC value for L4, C4, M4, and T4 against a series of microbes.

Microbes	MIC (mg/mL)			
	L4	C4	M4	T4
<i>Bacillus cereus</i> ATCC 14579	25	>100	>100	>100
<i>Bacillus subtilis</i> ATCC 8188	25	>100	>100	>100
<i>Enterococcus faecalis</i> ATCC 29212	50	>100	>100	>100
VRE ATCC 700802	50	>100	>100	>100
Methicillin-sensitive <i>S. aureus</i> ATCC 29213	6.25	>100	>100	>100
Methicillin-sensitive <i>S. aureus</i> ATCC 33591	25	>100	>100	>100
Methicillin-resistant <i>S. aureus</i> ATCC 43300	6.25	>100	>100	>100
Methicillin-resistant <i>S. aureus</i> ATCC 33519	6.25	>100	>100	>100
<i>Escherichia coli</i> ATCC 25922	25	>100	>100	>100
<i>Pseudomonas aeruginosa</i> ATCC 10145	>100	>100	>100	>100
<i>Klebsiella pneumoniae</i> ATCC 10031	12.50	>100	>100	>100
<i>Shigella flexneri</i> ATCC 12022	>100	>100	>100	>100
<i>Candida albicans</i> IMR	>100	>100	>100	>100
<i>Candida albicans</i> clinical isolate	>100	>100	>100	>100
<i>Candida tropicalis</i> clinical isolate	>100	>100	>100	>100

Table 4.44: MBC value for L4, C4, M4, and T4 against a series of microbes.

Microbes	MBC (mg/mL)			
	L4	C4	M4	T4
<i>Bacillus cereus</i> ATCC 14579	25	>100	>100	>100
<i>Bacillus subtilis</i> ATCC 8188	25	>100	>100	>100
<i>Enterococcus faecalis</i> ATCC 29212	25	>100	>100	>100
VRE ATCC 700802	50	>100	>100	>100
Methicillin-sensitive <i>S. aureus</i> ATCC 29213	25	>100	>100	>100
Methicillin-sensitive <i>S. aureus</i> ATCC 33591	50	>100	>100	>100
Methicillin-resistant <i>S. aureus</i> ATCC 43300	25	>100	>100	>100
Methicillin-resistant <i>S. aureus</i> ATCC 33519	12.50	>100	>100	>100
<i>Escherichia coli</i> ATCC 25922	>100	>100	>100	>100
<i>Pseudomonas aeruginosa</i> ATCC 10145	>100	>100	>100	>100
<i>Klebsiella pneumoniae</i> ATCC 10031	>100	>100	>100	>100
<i>Shigella flexneri</i> ATCC 12022	>100	>100	>100	>100
<i>Candida albicans</i> IMR	>100	>100	>100	>100
<i>Candida albicans</i> clinical isolate	>100	>100	>100	>100
<i>Candida tropicalis</i> clinical isolate	>100	>100	>100	>100

4.5.5 Overall Antimicrobial activity

The overall result suggested that all ligands, namely **L1**, **L2**, **L3**, and **L4** displayed significant antimicrobial activities. However, only second and third series photoCORMs are slightly active against the tested microbes and showed minimal photo-induced antimicrobial activities, whereas first and fourth series are non-active. Besides, the results also suggested that binding of the ligands to the group 6 metal carbonyls had significantly lower their antimicrobial activities. The slight antimicrobial activities of second and third series may be attributed to the presence of phenolic hydroxyl group, Ph–OH which may have improved their water solubility in the cell culture media. Hence, the overall results suggest that the presence phenanthroline nitrogens and phenolic hydroxyl groups are vital for the antimicrobial activities regardless of the presence of CO.

4.6 ADME Properties

4.6.1 ADME calculations of L1, C1, M1, and T1

The absorption, distribution, metabolism, and excretion (ADME) properties of all compounds were predicted using SwissADME simulation and the first series compounds' data are shown in Table 4.45 (Daina et al., 2017). Based on the rule of five (Ro5) model proposed by Lipinski et.al. all first series compounds, namely **L1**, **C1**, **M1**, and **T1** have acceptable number of hydrogen bond acceptor (HBA) group with **L1** = 3 and photoCORMs = 5 (Ideal HBA = $10 \leq$) (Lipinski et al., 1997). However, no hydrogen bond donor (HBD) group present in the structures of all compounds (Ideal HBD = $5 \leq$). In terms of rotatable bonds (RotB) which correspond to the molecular flexibility whereby it dictates the potential oral bioavailability of the compounds, all compounds showed only 2 rotatable bonds in the structure (Ideal RotB = $10 \leq$). The compounds also displayed acceptable octanol-water partition coefficient ($\text{Log } P_{o/w}$) with values lower than 5 except for **L1** with $\text{Log } P_{o/w} = 5.11$ (Ideal $\text{Log } P_{o/w} = 5 \leq$). The photoCORMs violated the Ro5 in terms of molecular weight (M.W) with $\text{M.W} = > 500$ g/mol except for **L1**. The calculated topological polar surface area (TPSA) and $\text{Log } K_p$ suggest that all compounds may have good cells and skin permeability (Ideal TPSA = $20 - 130 \text{ \AA}^2$ and $\text{Log } K_p$ = more negative, less skin permeation) which may have contributed to their high cytotoxicity against the colon cancer cell lines. The Bioavailability Radar of the compounds are shown in Figure 4.20, Figure 4.22, Figure 4.24, and Figure 4.26, respectively, which are visual representations of the potential “drug-likeness” of the compounds in which the pink area represented the ideal lipophilicity, molecular weight, polarity, water solubility, saturation, and flexibility. The Lipinski (Pfizer) model predicts that all first series compounds can be potential drugs despite the slight violation in the molecular weight for the photoCORMs. The BOILED-Egg graphical representations of the compounds are shown in Figure 4.21, Figure 4.23, Figure 4.25, and Figure 4.27, respectively, which evaluate the potential of

the compounds in terms of passive gastrointestinal absorption (HIA) and blood brain barrier penetration (BBB). If the compound falls in the “egg-white” region, it is likely that the compound will be passively absorbed in the gastrointestinal tract and if the compound falls in the “egg-yolk” region, it suggests that the compound has the ability to penetrate the BBB, however, the two regions are not mutually exclusive. The ligand **L1** is predicted to be able to absorb into the gastrointestinal tract but it will not penetrate the BBB. In contrast, the photoCORMs are predicted to be able to absorb into the gastrointestinal tract and able to penetrate the BBB but will be actively efflux by the permeability glycoprotein (PGP) in the BBB.

Table 4.45: ADME properties of L1, C1, M1, and T1.

	L1	C1	M1	T1
Molecular weight (g/mol)	371.43	535.47	579.43	667.31
Consensus Log $P_{o/w}$	5.11	2.92	2.98	3.09
HBA	3	5	5	5
HBD	0	0	0	0
Rotatable bonds	2	2	2	2
TPSA (\AA^2)	38.14	22.22	22.22	22.22
Log K_p (SP*) (cm/s)	-4.75	-3.97	-4.24	-4.78
BBB permeant	No	Yes	Yes	Yes
Drug-likeness (Lipinski [Pfizer] model)	Yes	Yes	Yes	Yes

*SP = Skin permeability.

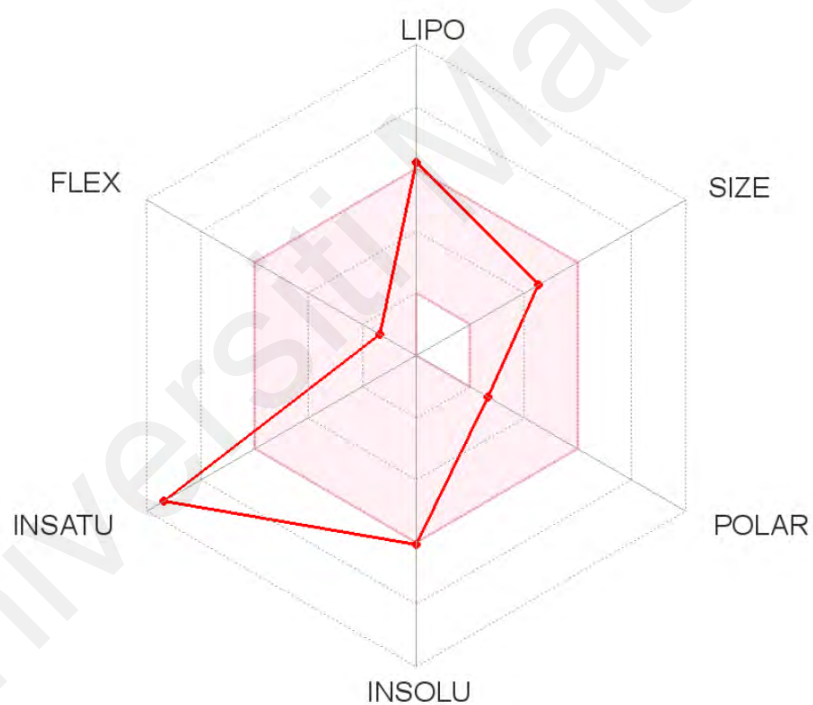
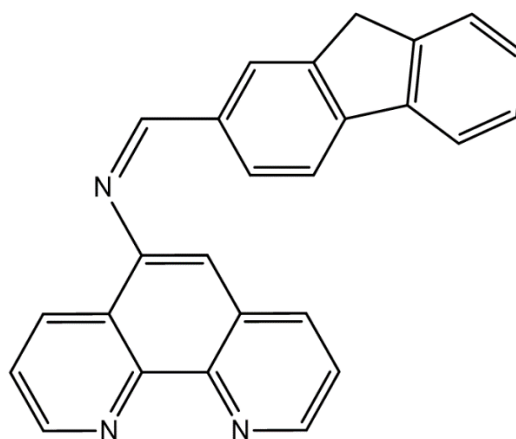


Figure 4.20: The drug-likeness bioavailability radar of L1.

*LIPO = Lipophilicity, SIZE = Molecular weight, POLAR = Polarity, INSOLU = solubility, INSATU = Unsaturated bonds, and FLEX = Flexibility/rotatable bonds

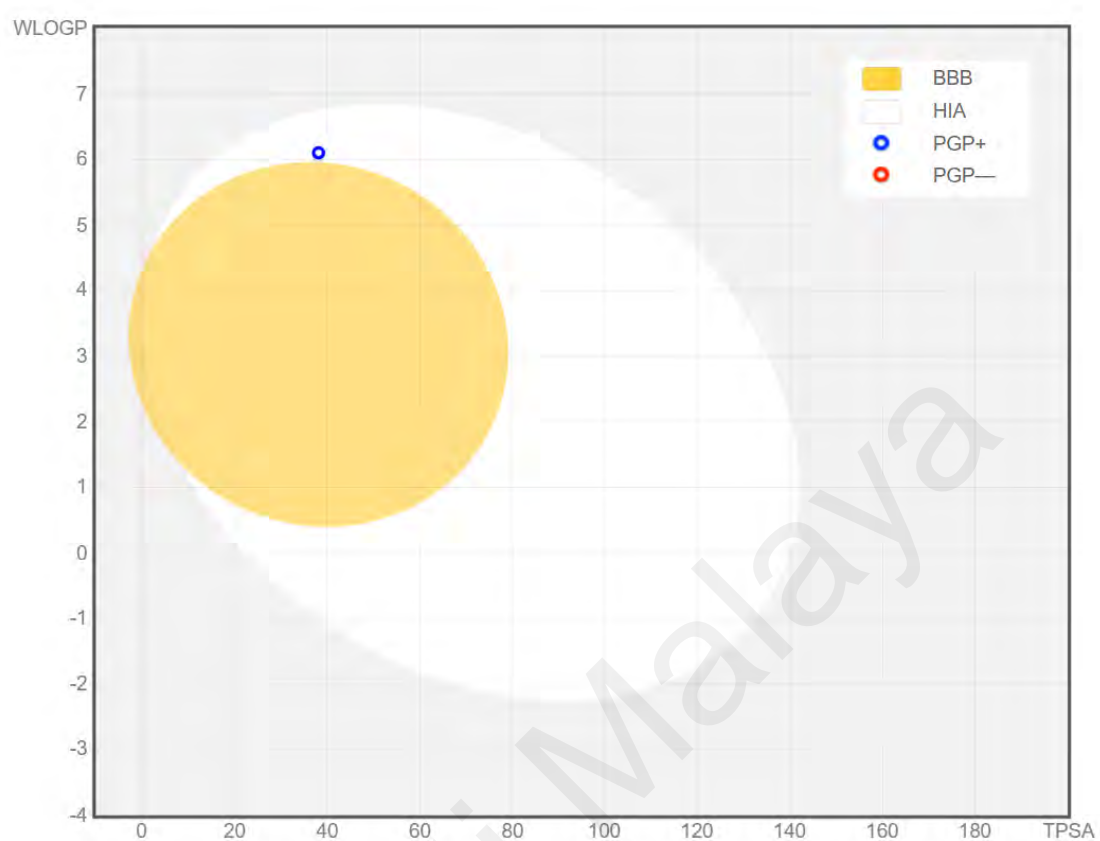


Figure 4.21 : The BOILED-Egg graphical representation of L1.

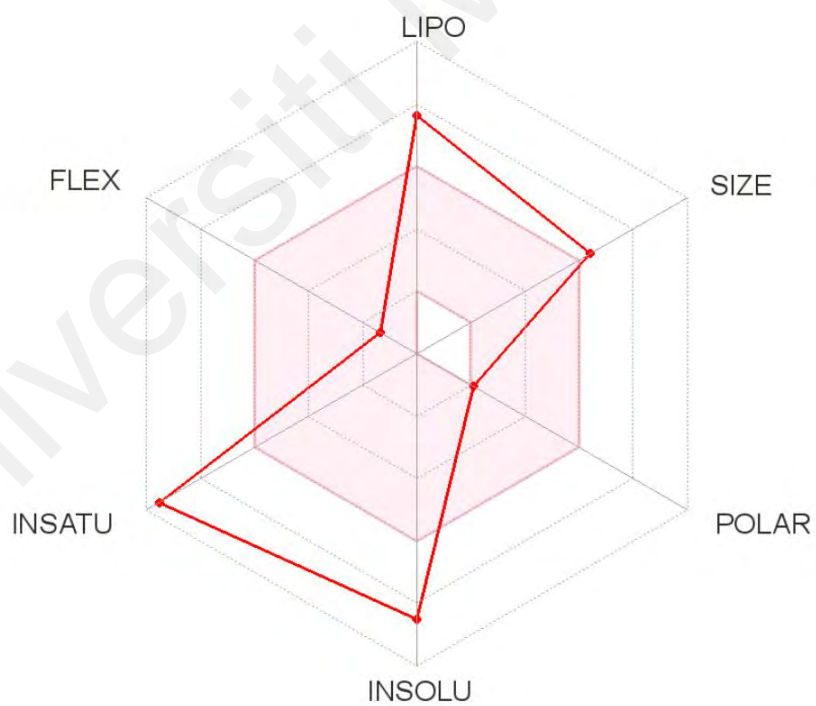
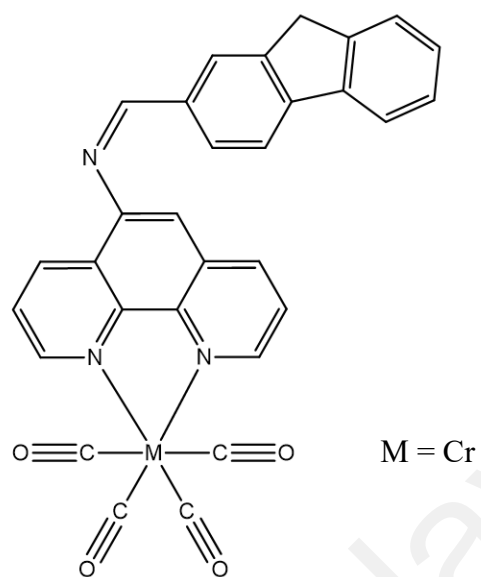


Figure 4.22: The drug-likeness bioavailability radar of C1.

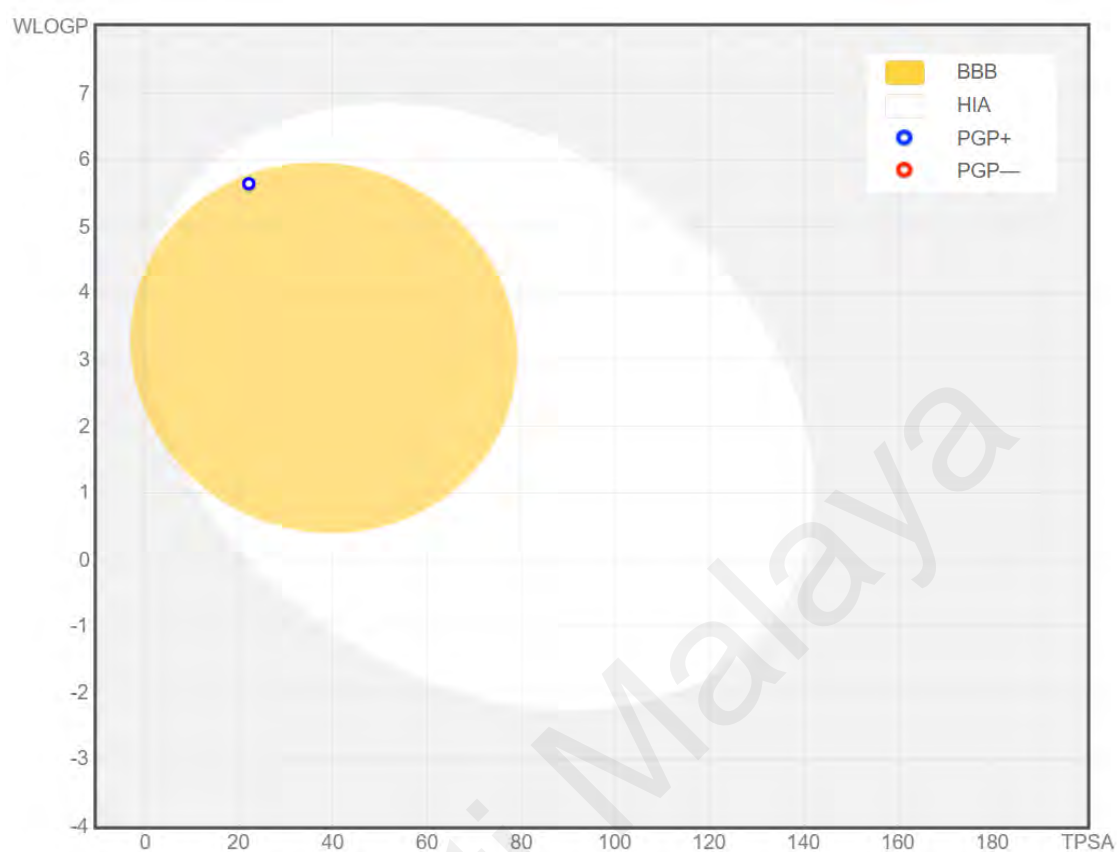


Figure 4.23: The BOILED-Egg graphical representation of C1.

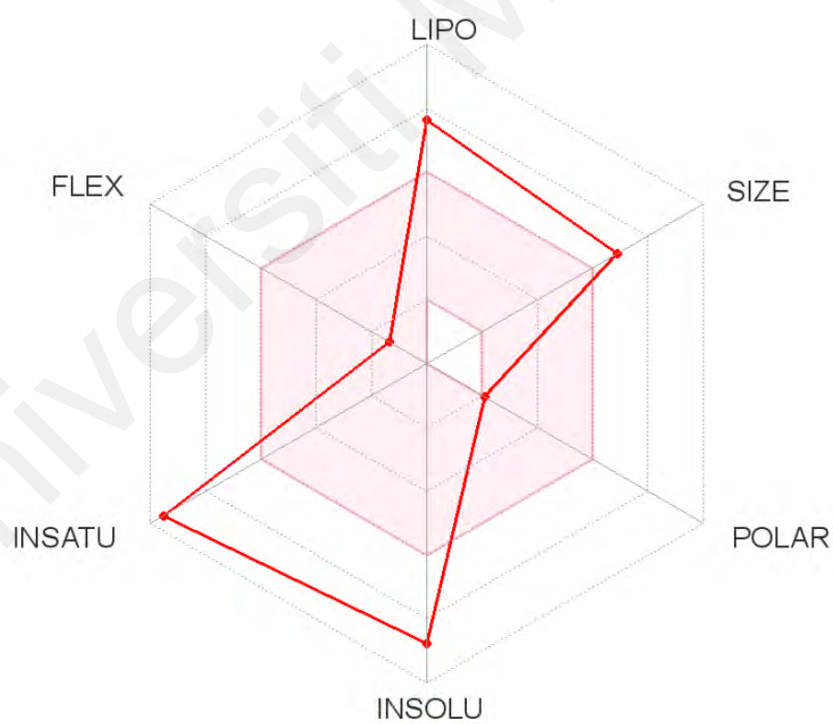
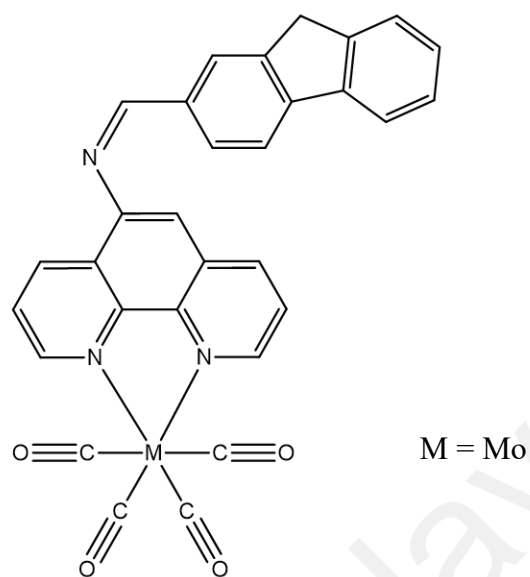


Figure 4.24: The drug-likeness bioavailability radar of M1.

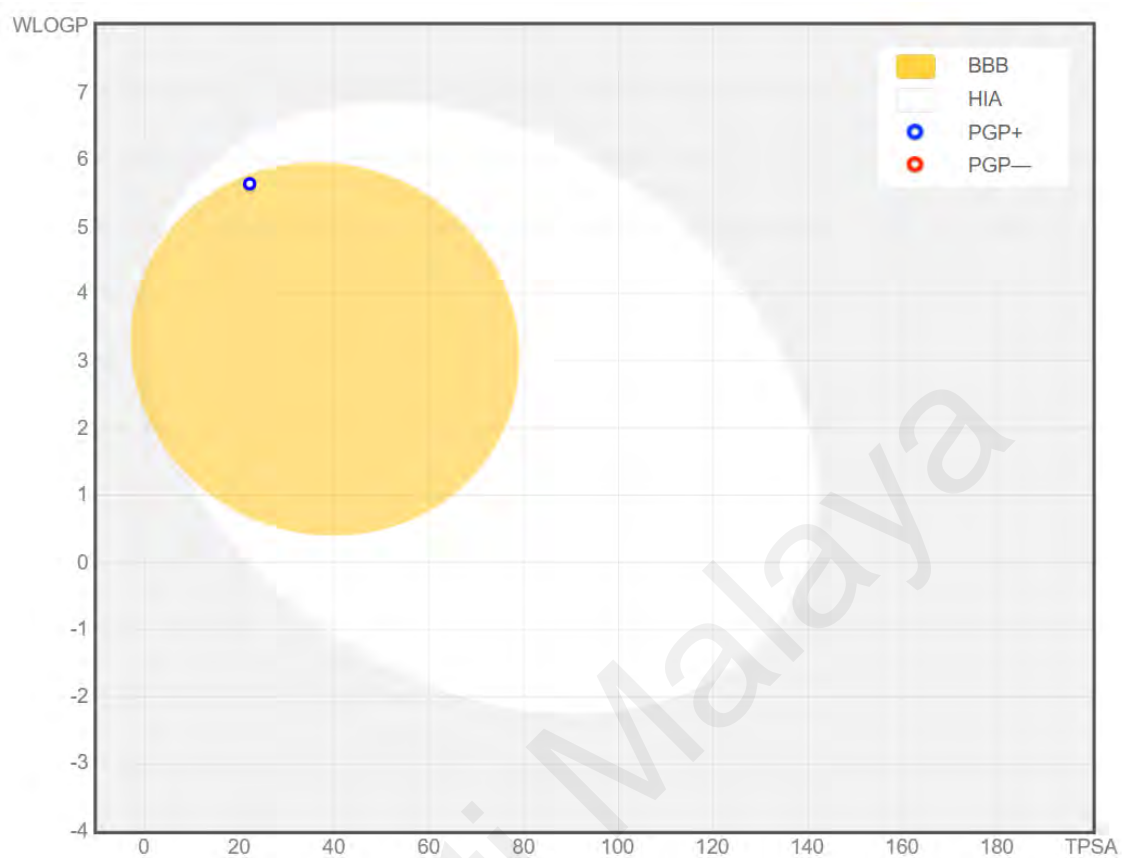


Figure 4.25: The BOILED-Egg graphical representation of M1.

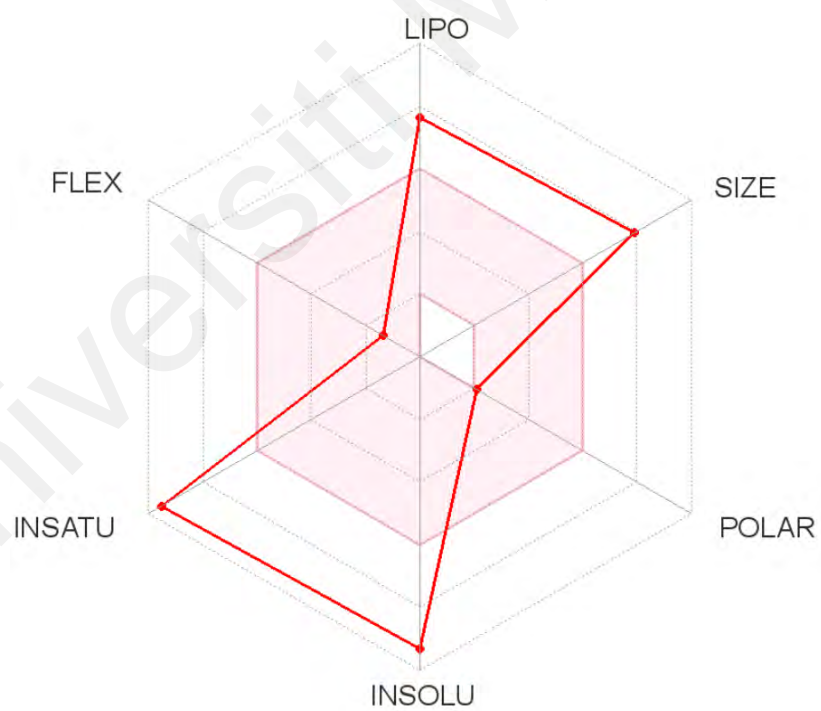
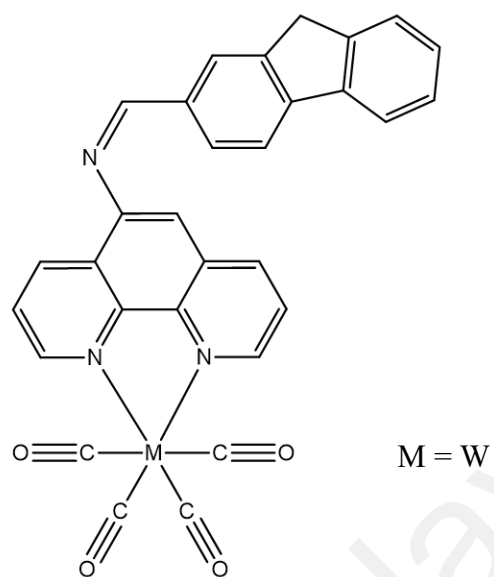


Figure 4.26: The drug-likeness bioavailability radar of T1.

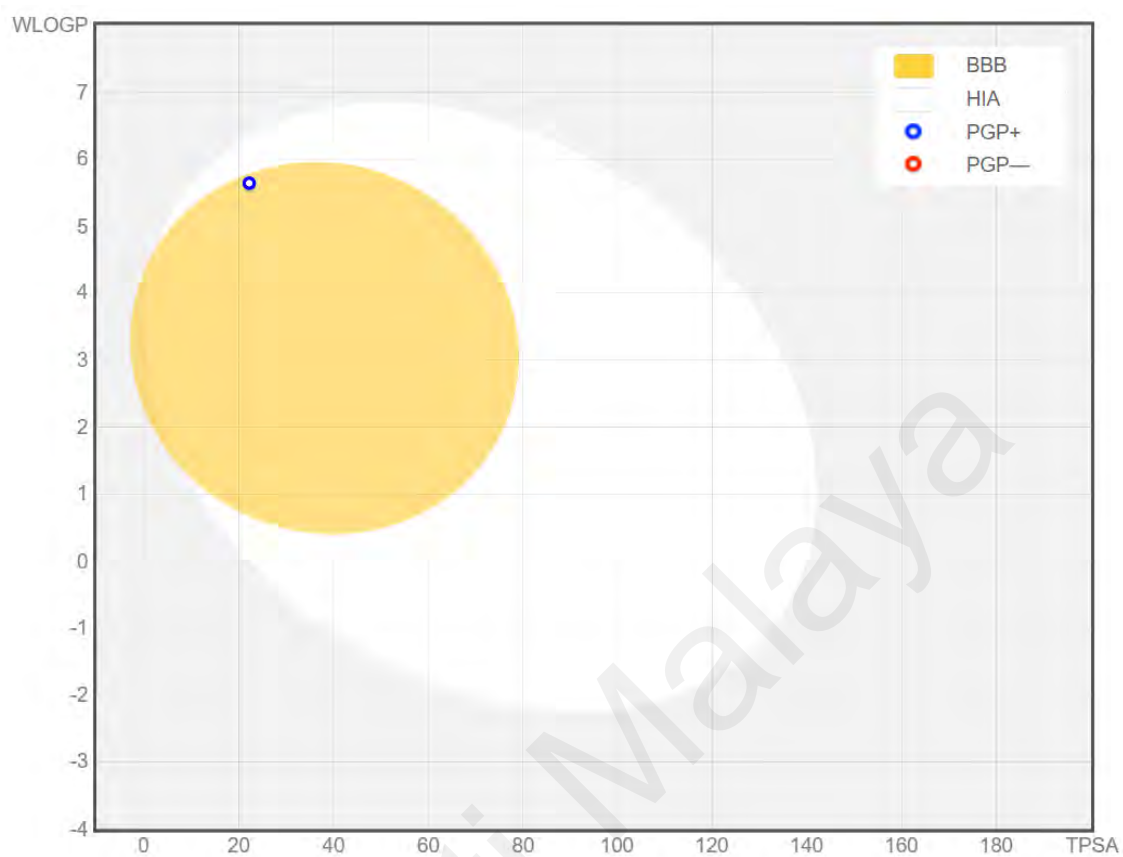


Figure 4.27: The BOILED-Egg graphical representation of T1.

4.6.2 ADME calculations of L2, C2, M2, and T2

The simulated ADME properties of second series compounds, namely **L2**, **C2**, **M2**, and **T2** are shown in Table 4.46. All compounds have 1 HBD and 2 RotB present in the structures and **L1** has 4 HBA whereas the photoCORMs **C2**, **M2**, and **T2** have 6 HBA. The Log $P_{o/w}$ values of the compounds showed that the photoCORMs have a higher lipophilicity compared to the ligand **L2**. All compounds are within the acceptable range stated by Lipinski Ro5 except of the molecular weight in which the photoCORMs violated the molecular weight rule with M.W > 500 g/mol. The calculated topological polar surface area (TPSA) and Log K_p suggest that all second series compounds may have excellent cells and skin permeability with **C2** being the most skin permeable which may have contributed to their high cytotoxicity against the colon cancer cell lines. The Bioavailability Radar of the compounds are shown in Figure 4.28, Figure 4.30, Figure 4.32, and Figure 4.34. The Lipinski (Pfizer) model predicts that all second series compounds can be potential drugs despite the slight violation in the molecular weight for the second series photoCORMs. The BOILED-Egg graphical representations of the compounds are shown in Figure 4.29, Figure 4.31, Figure 4.33, and Figure 4.35, respectively, which evaluate the potential of the compounds in terms of passive gastrointestinal absorption (HIA) and blood brain barrier penetration (BBB). All compounds are predicted to be able to absorb in the gastrointestinal tract and also able to penetrate the BBB but the compounds will be actively effluxed from the brain by the PGP proteins in the BBB.

Table 4.46: ADME properties of L2, C2, M2, and T2.

	L2	C2	M2	T2
Molecular weight (g/mol)	349.38	513.42	557.39	645.27
Consensus Log $P_{o/w}$	4.15	2.13	2.19	2.30
HBA	4	6	6	6
HBD	1	1	1	1
Rotatable bonds	2	2	2	2
TPSA (\AA^2)	58.37	42.45	42.45	42.45
Log K_p (SP) (cm/s)	-5.13	-4.36	-4.62	-5.16
BBB* permeant	Yes	Yes	Yes	Yes
Drug-likeness (Lipinski [Pfizer] model)	Yes	Yes	Yes	Yes

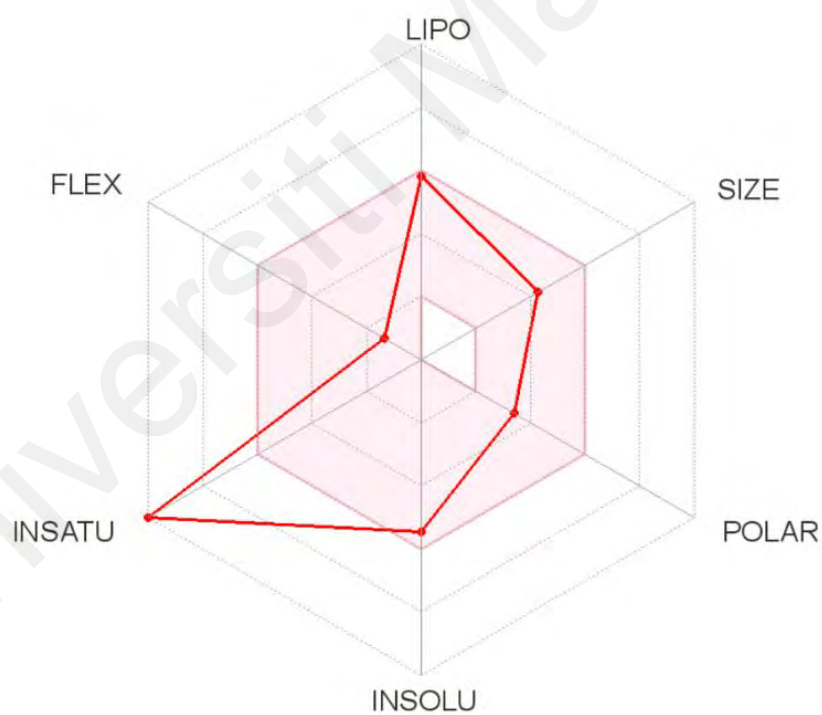
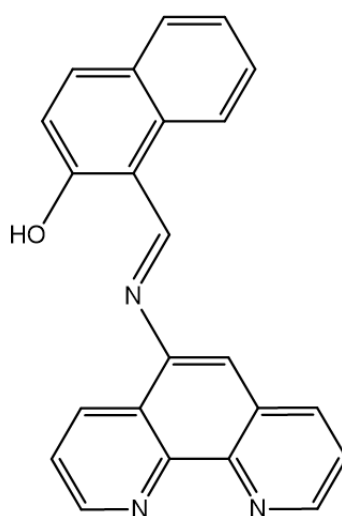


Figure 4.28: The drug-likeness bioavailability radar of L2.

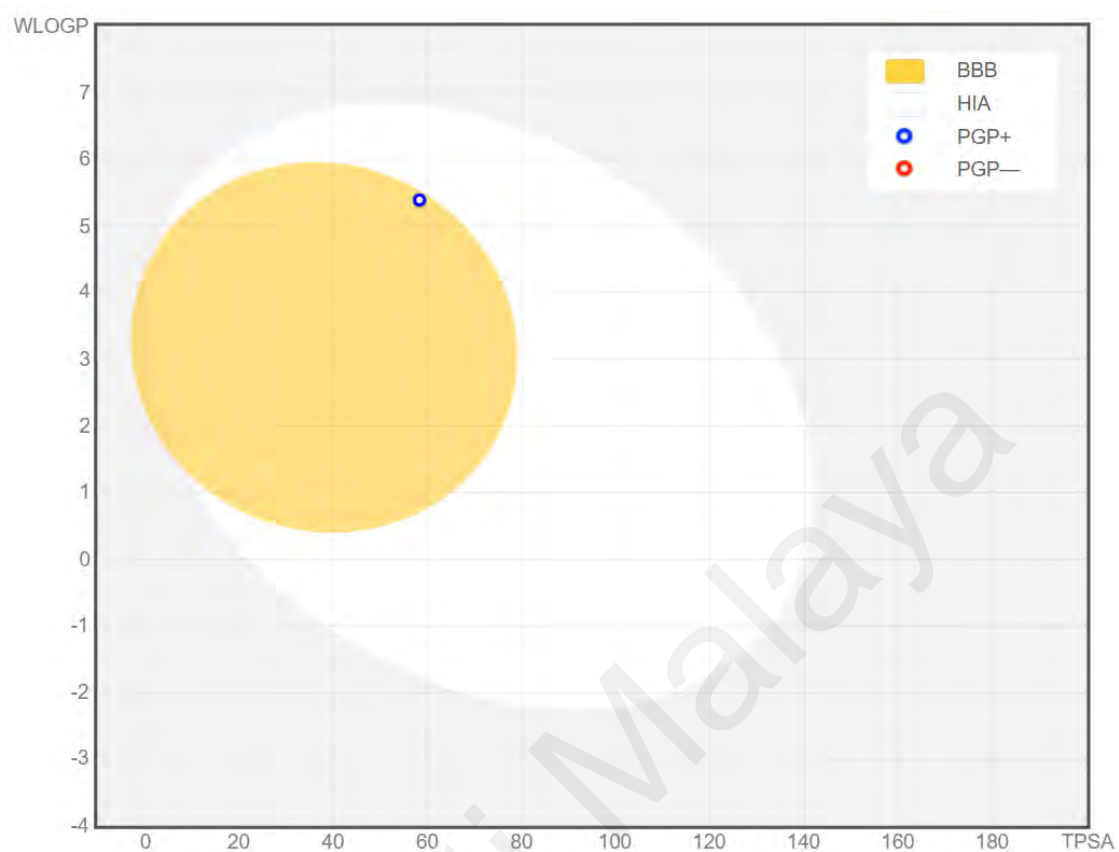


Figure 4.29: The BOILED-Egg graphical representation of L2.

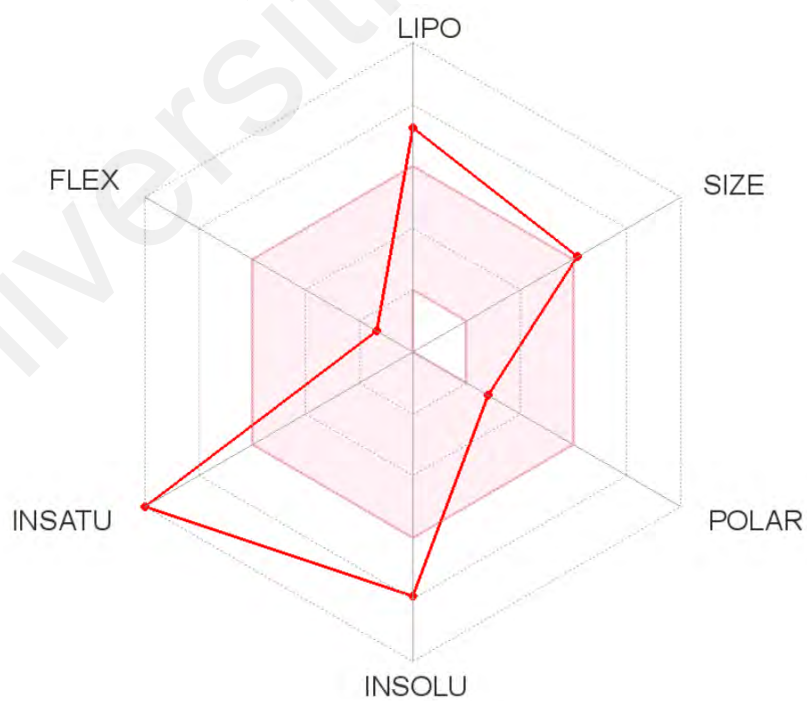
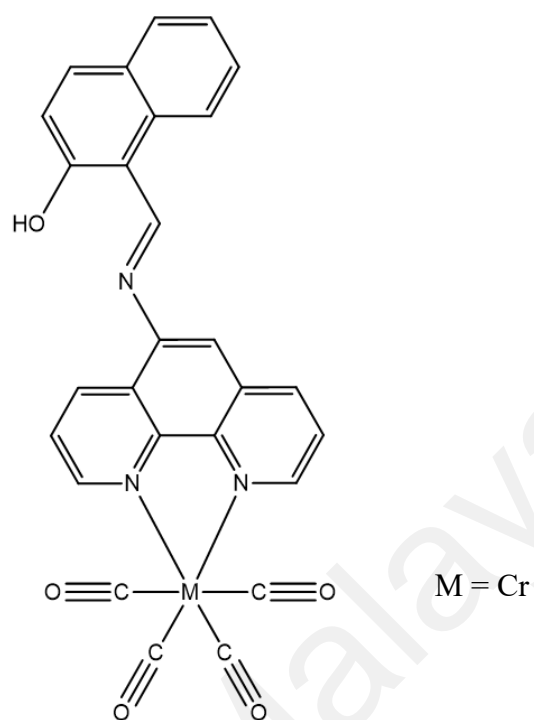


Figure 4.30: The drug-likeness bioavailability radar of C2.

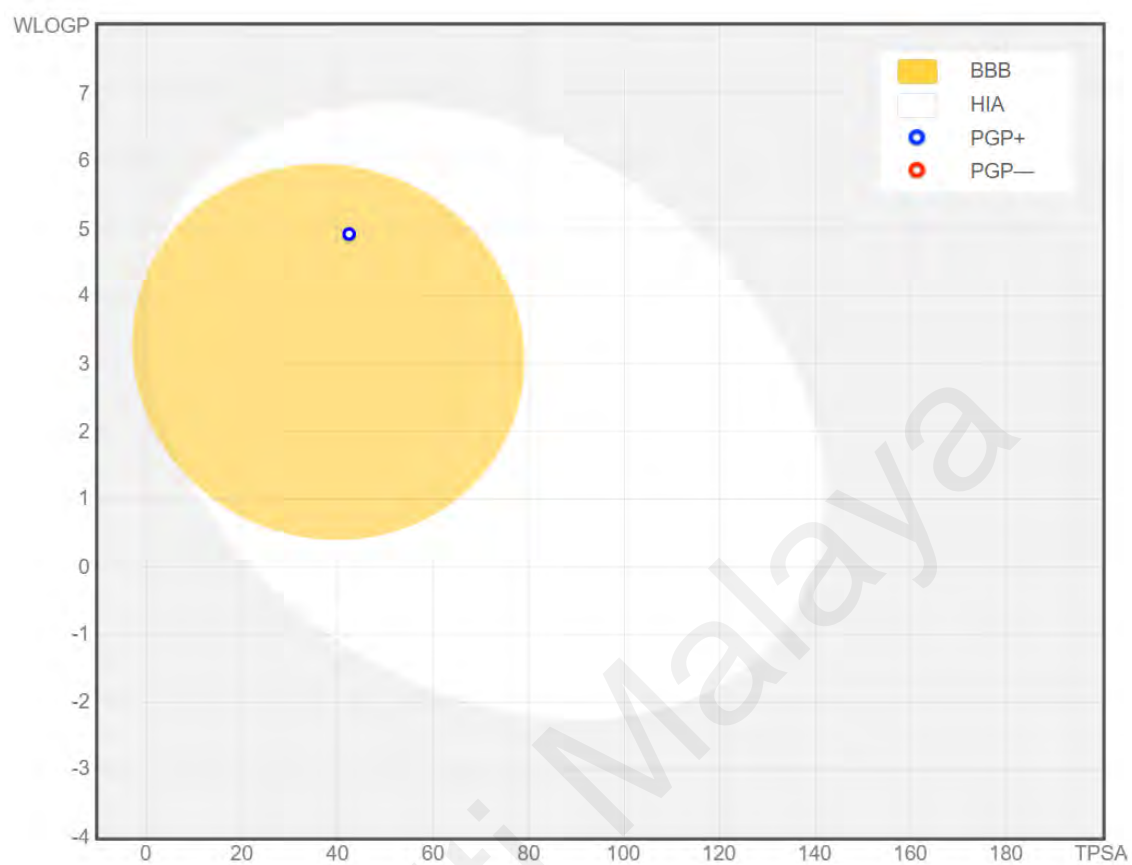


Figure 4.31: The BOILED-Egg graphical representation of C2.

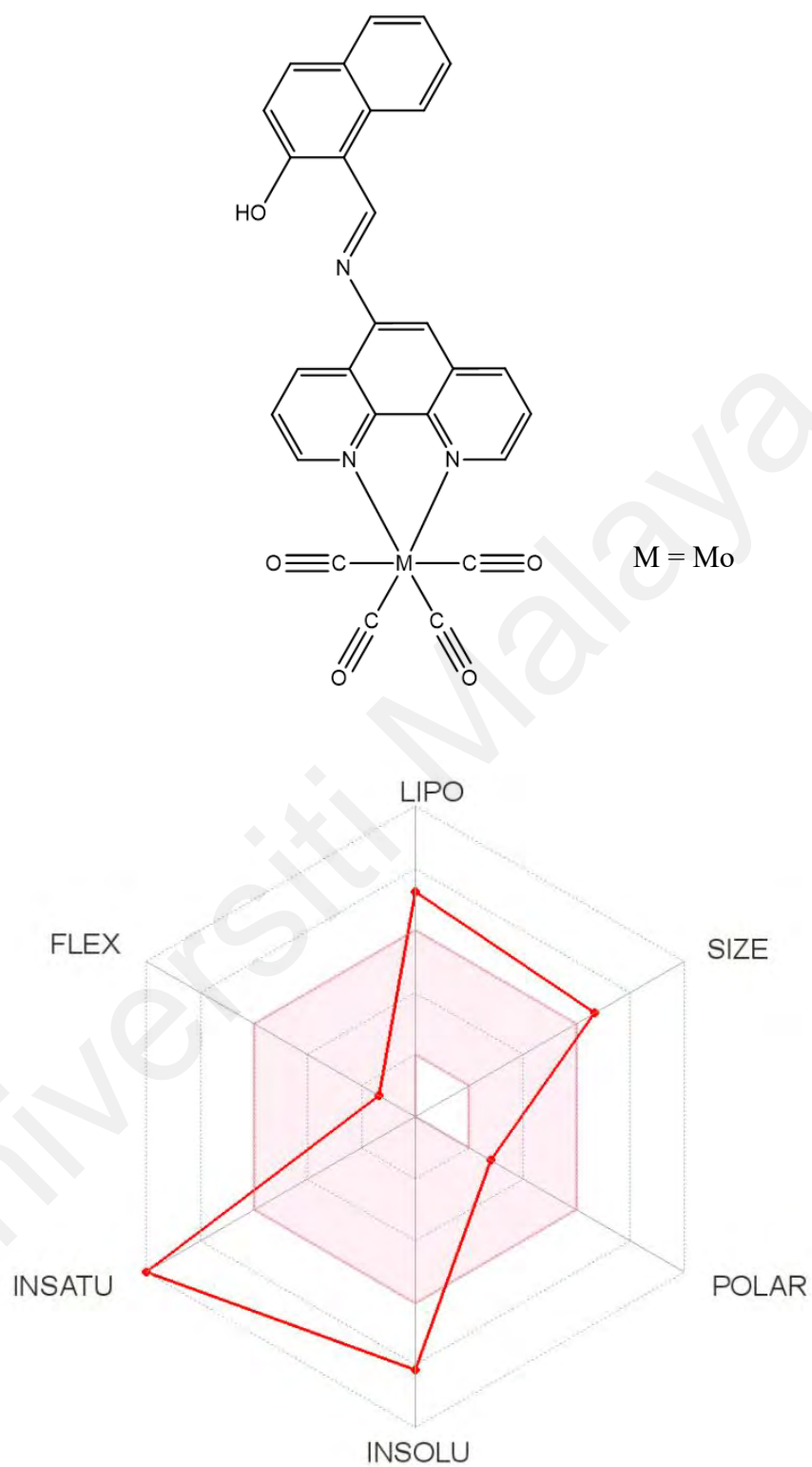


Figure 4.32: The drug-likeness bioavailability radar of M2.

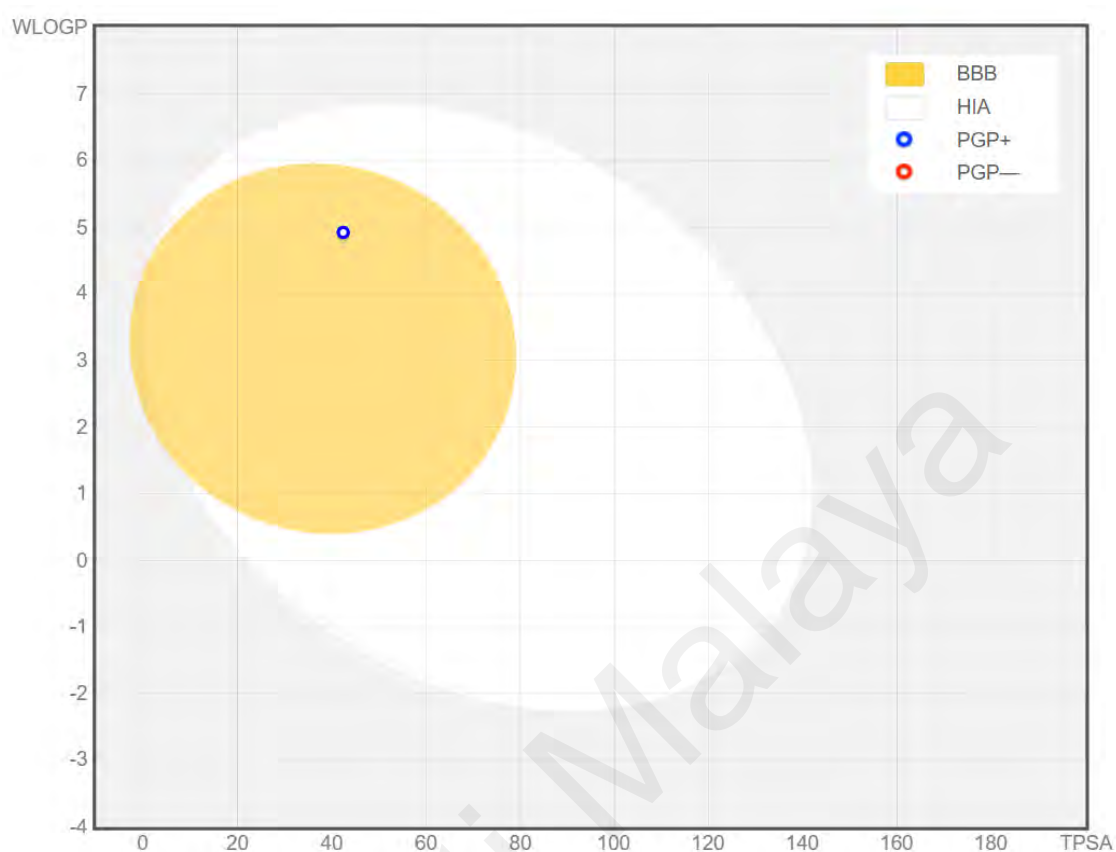


Figure 4.33: The BOILED-Egg graphical representation of M2.

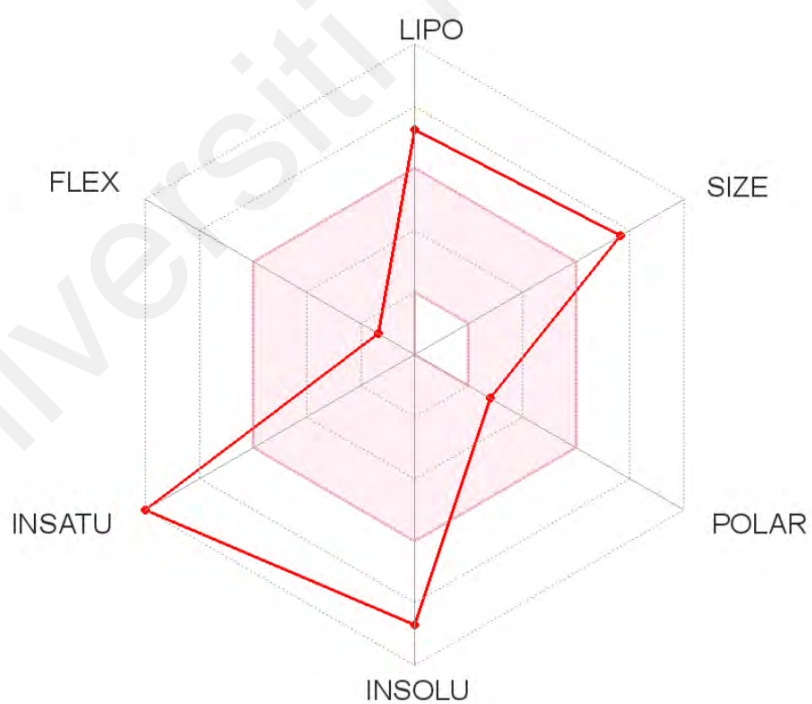
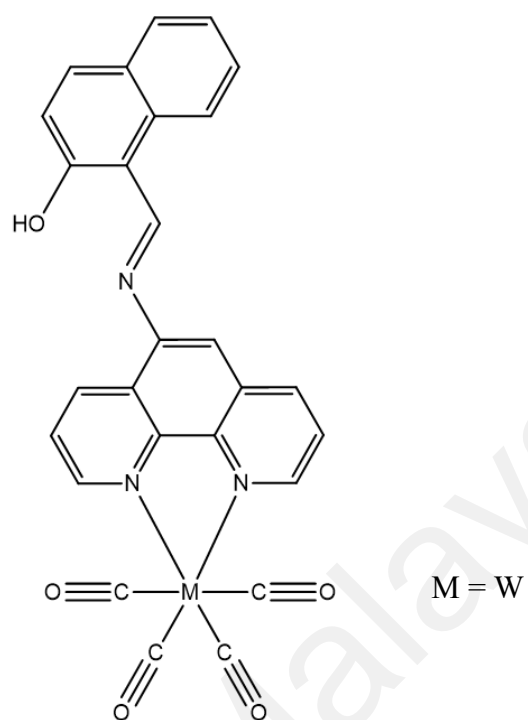


Figure 4.34: The drug-likeness bioavailability radar of T2.

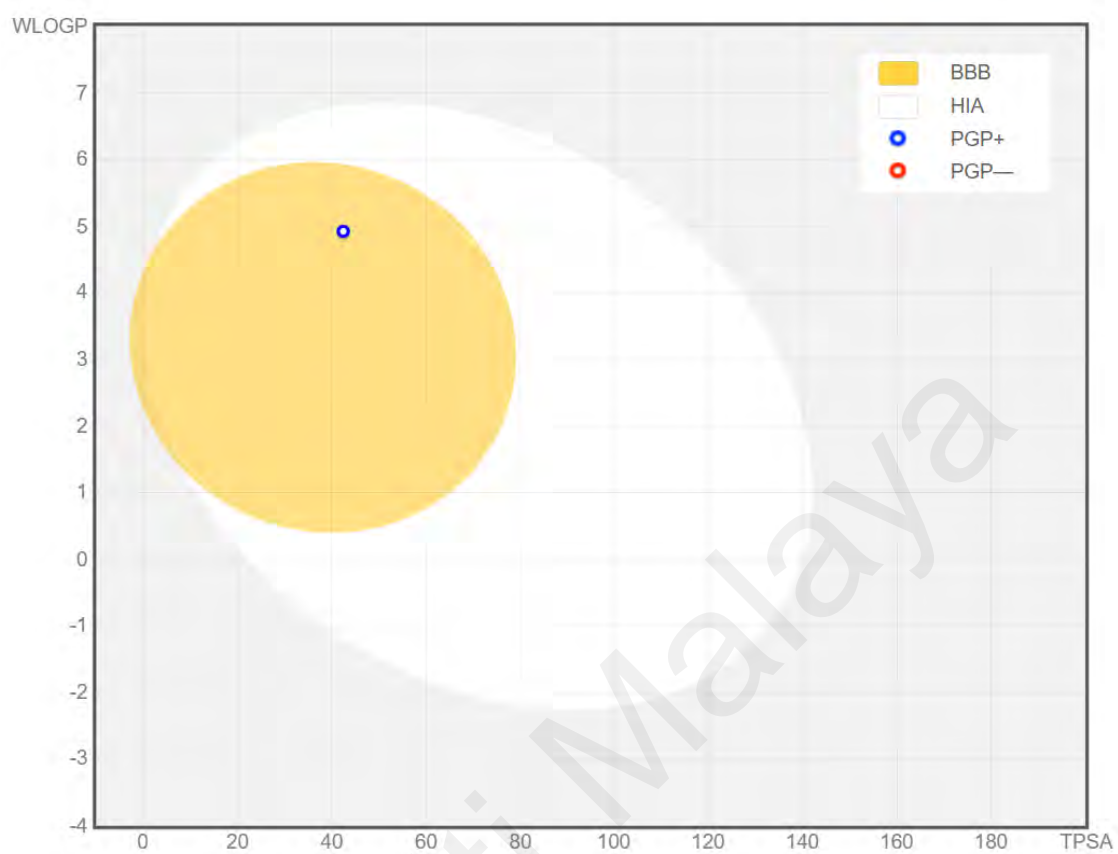


Figure 4.35: The BOILED-Egg graphical representation of T2.

4.6.3 ADME calculations of L3, C3, M3, and T3

The simulated ADME properties of third series compounds, namely **L3**, **C3**, **M3**, and **T3** are shown in Table 4.47. All compounds have 1 HBD and 3 RotB present in the structures and **L3** has 5 HBA whereas the photoCORMs **C3**, **M3**, and **T3** have 7 HBA. Similar to second series compounds, the Log $P_{o/w}$ values of the compounds showed that the photoCORMs have a higher lipophilicity compared to the ligand **L3**. All compounds are within the acceptable range stated by Lipinski Ro5 except of the molecular weight in which two of the photoCORMs, namely **M3** and **T3** violated the molecular weight rule with M.W > 500 g/mol. The calculated topological polar surface area (TPSA) and Log K_p suggest that all third series compounds may have excellent cells and skin permeability with **C3** being the most skin permeable among the third series compounds which may have contributed to their high cytotoxicity against the colon cancer cell lines. The Bioavailability Radar of the compounds are shown in Figure 4.36, Figure 4.38, Figure 4.40, and Figure 4.42. The Lipinski (Pfizer) model predicts that all third series compounds can be potential drugs despite the slight violation in the molecular weight for the **M3** and **T3**. The BOILED-Egg graphical representations of the compounds are shown in Figure 4.37, Figure 4.39, Figure 4.41, and Figure 4.43, respectively. All compounds are predicted to be able to absorb in the gastrointestinal tract and also able to penetrate the BBB. However, the simulation predicts that the photoCORMs **C3**, **M3**, and **T3** will be actively effluxed from the BBB by PGP protein after penetration but the ligand **L3** will not be effluxed.

Table 4.47: ADME properties of L3, C3, M3, and T3.

	L3	C3	M3	T3
Molecular weight (g/mol)	329.35	493.39	537.35	625.23
Consensus Log $P_{o/w}$	3.31	1.27	1.32	1.43
HBA	5	7	7	7
HBD	1	1	1	1
Rotatable bonds	3	3	3	3
TPSA (\AA^2)	67.60	51.68	51.68	51.68
Log K_p (SP) (cm/s)	-5.92	-5.14	-5.41	-5.95
BBB permeant	Yes	Yes	Yes	Yes
Drug-likeness (Lipinski [Pfizer] model)	Yes	Yes	Yes	Yes

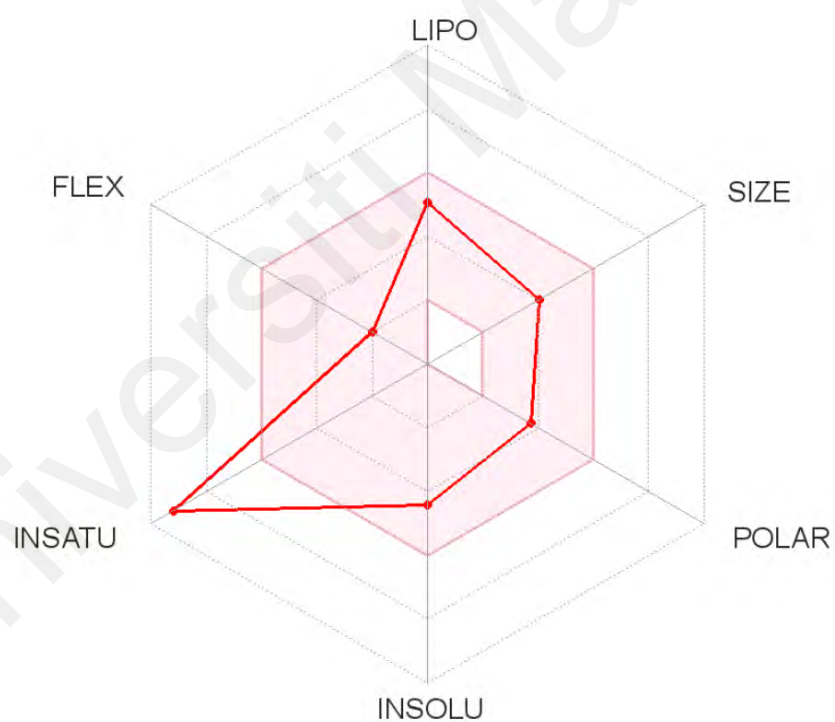
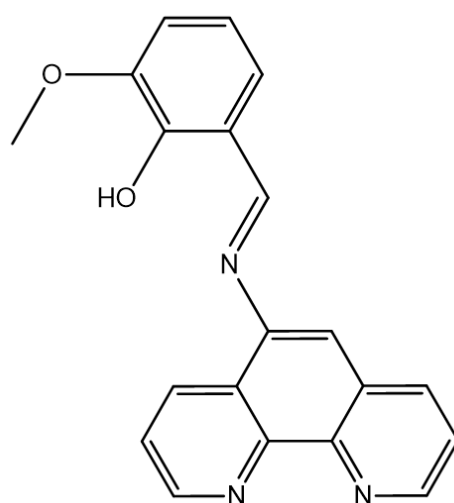


Figure 4.36: The drug-likeness bioavailability radar of L3.

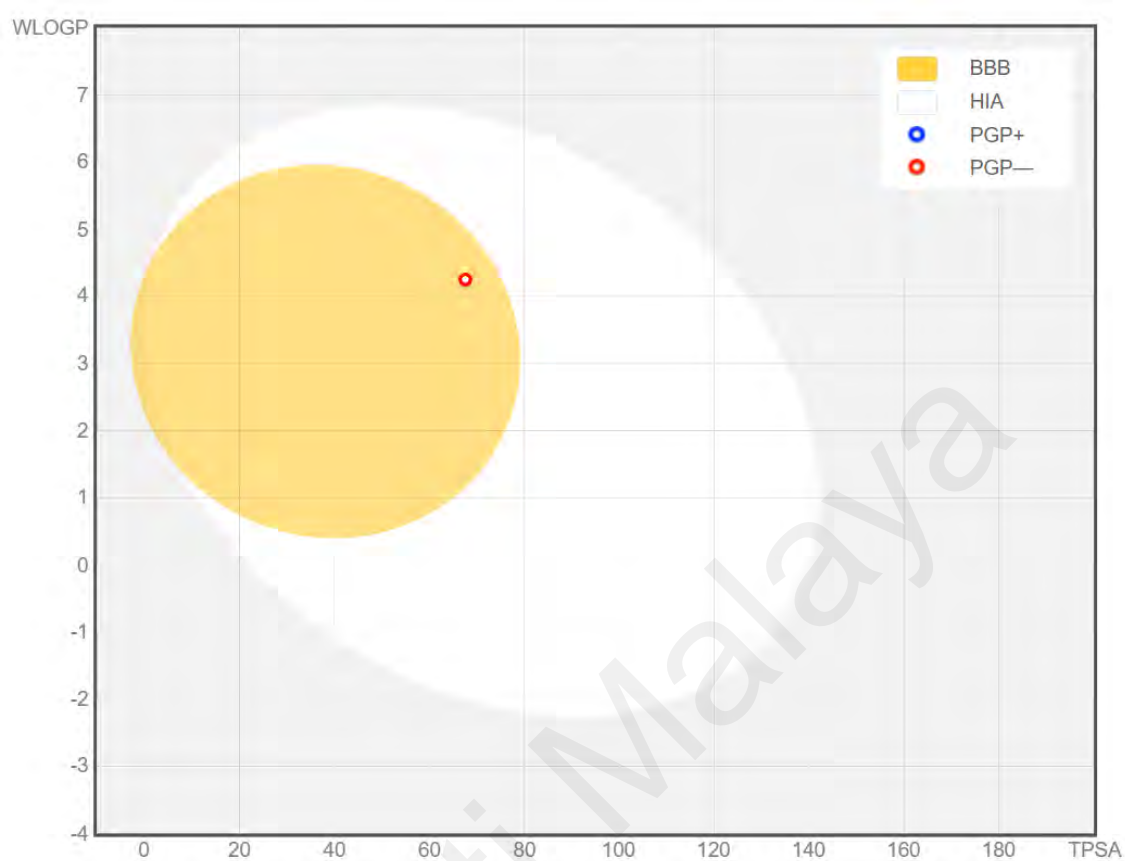


Figure 4.37: The BOILED-Egg graphical representation of L3.

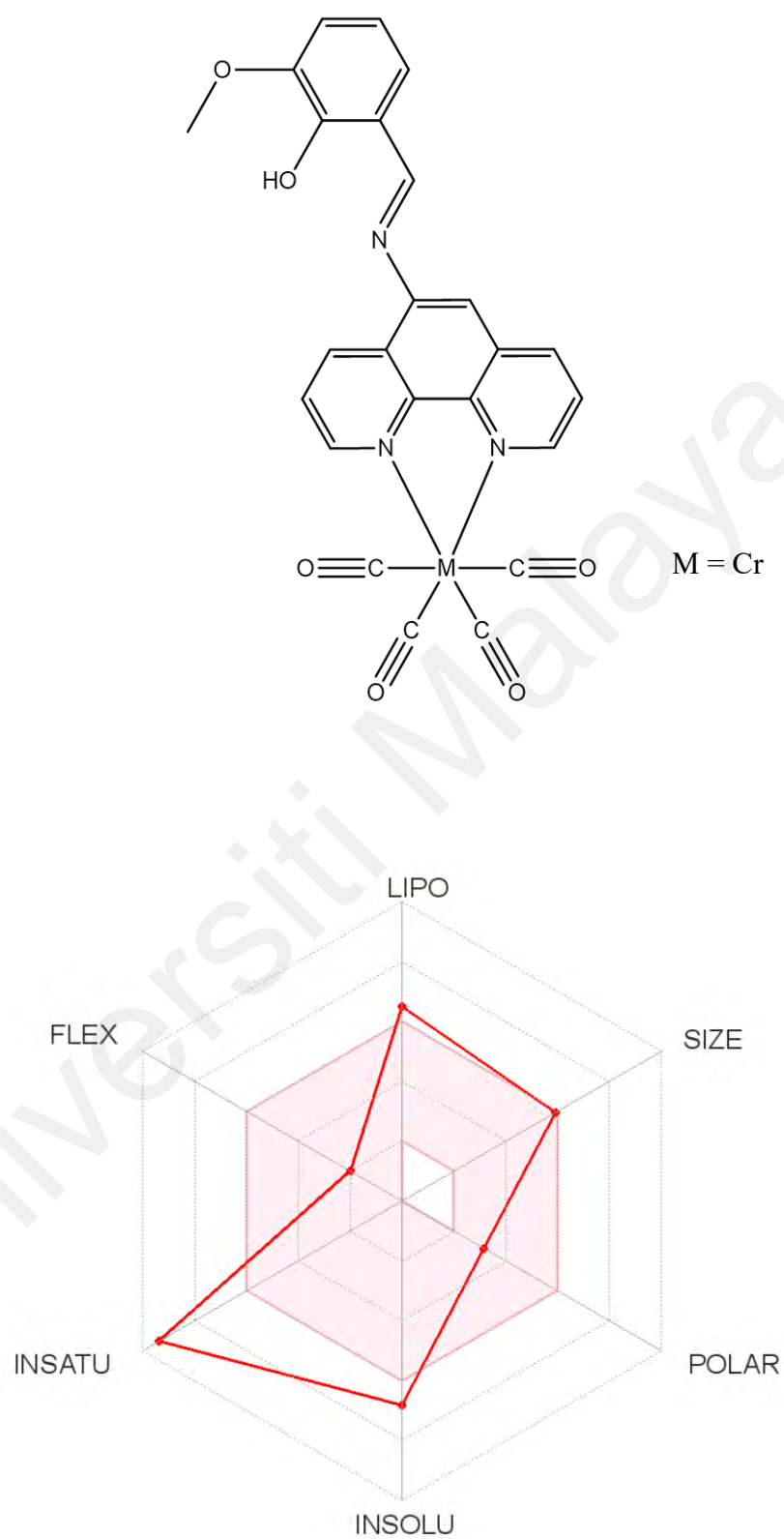


Figure 4.38: The drug-likeness bioavailability radar of C3.

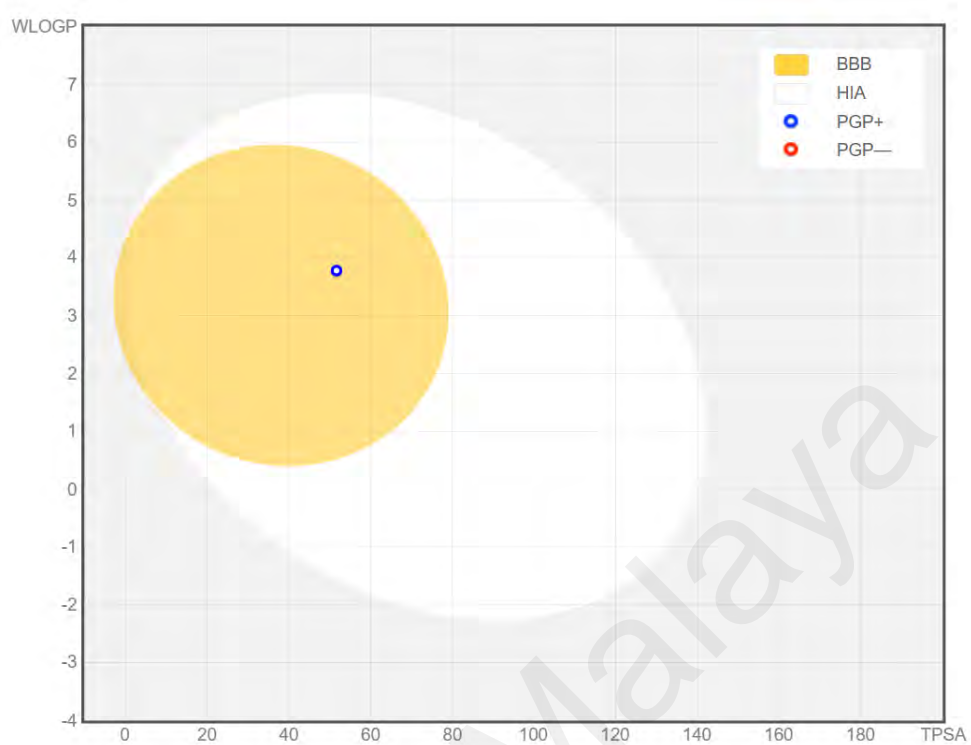


Figure 4.39: The BOILED-Egg graphical representation of C3.

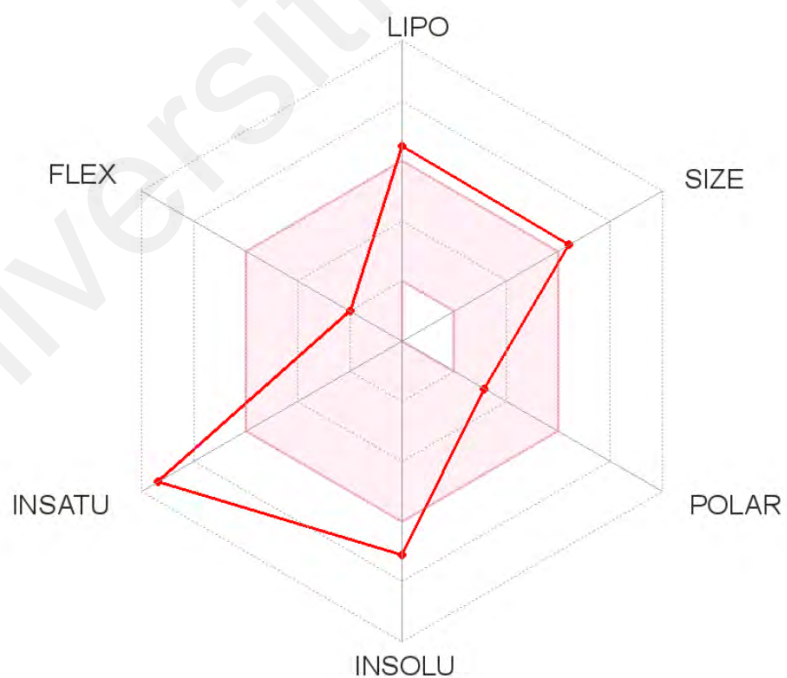
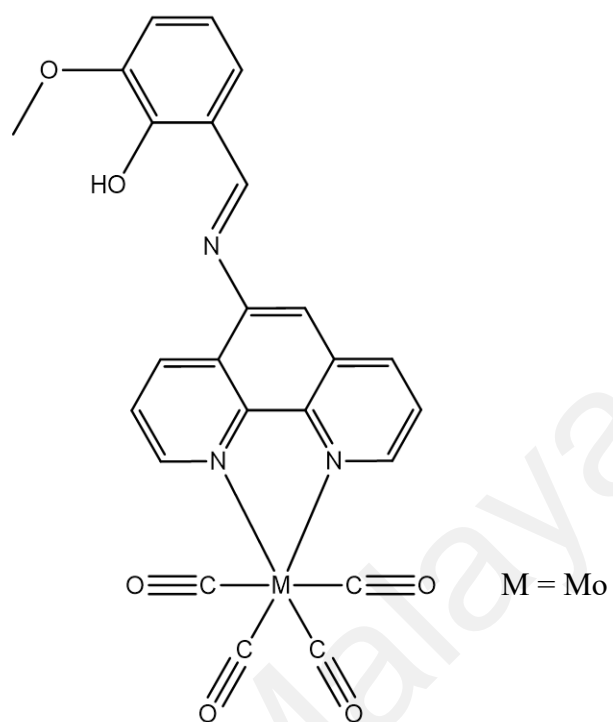


Figure 4.40: The drug-likeness bioavailability radar of M3.

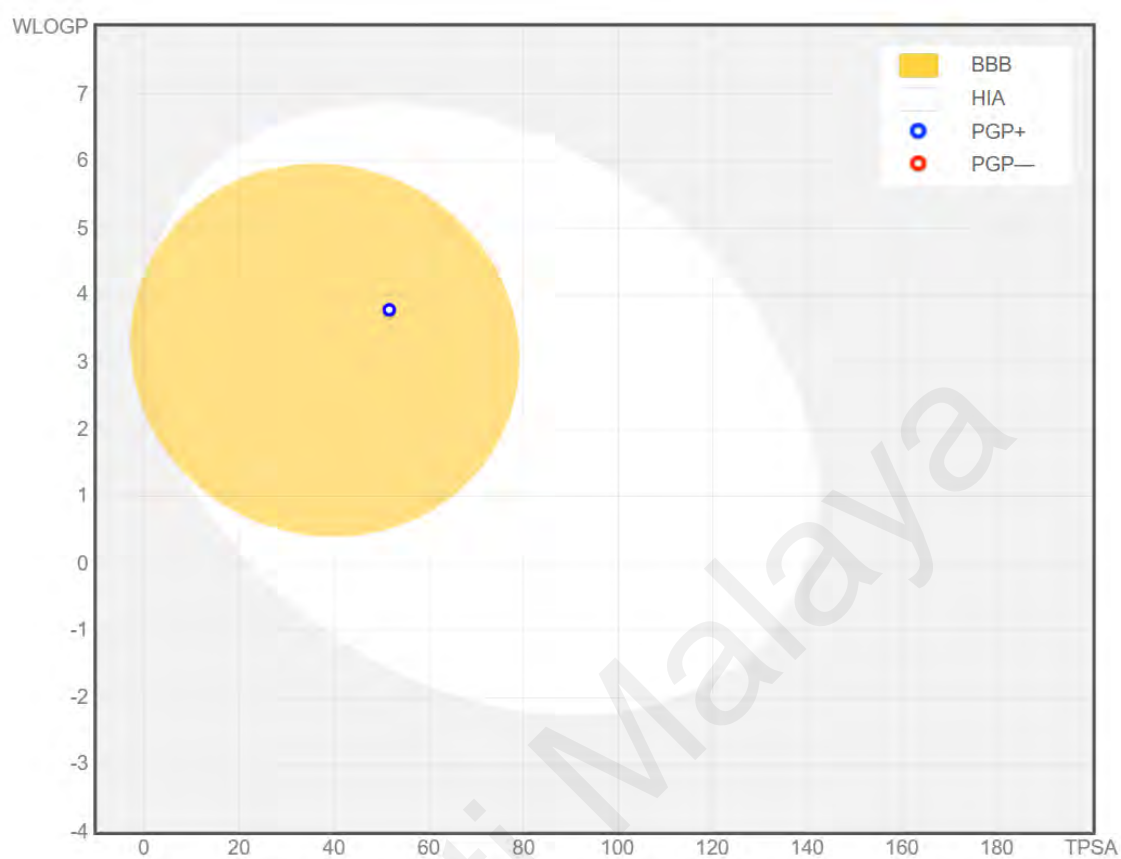


Figure 4.41: The BOILED-Egg graphical representation of M3.

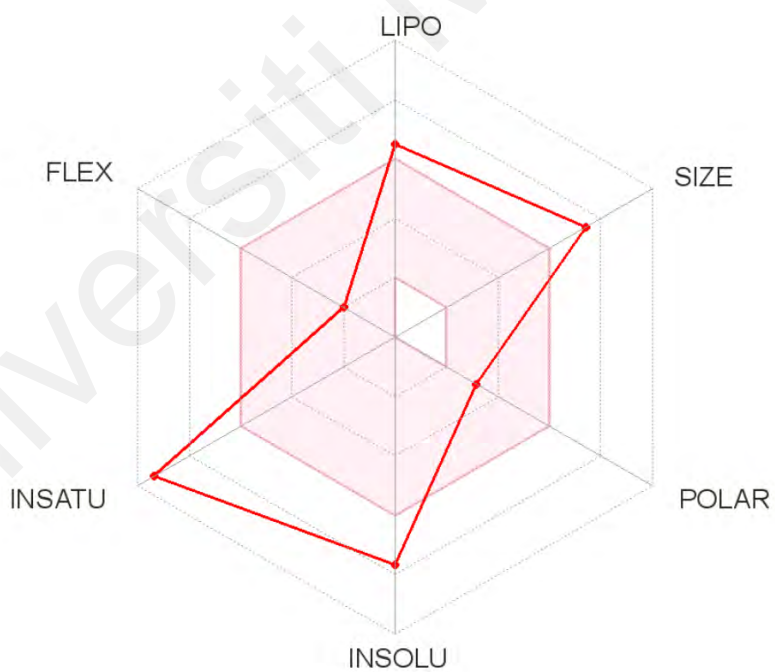
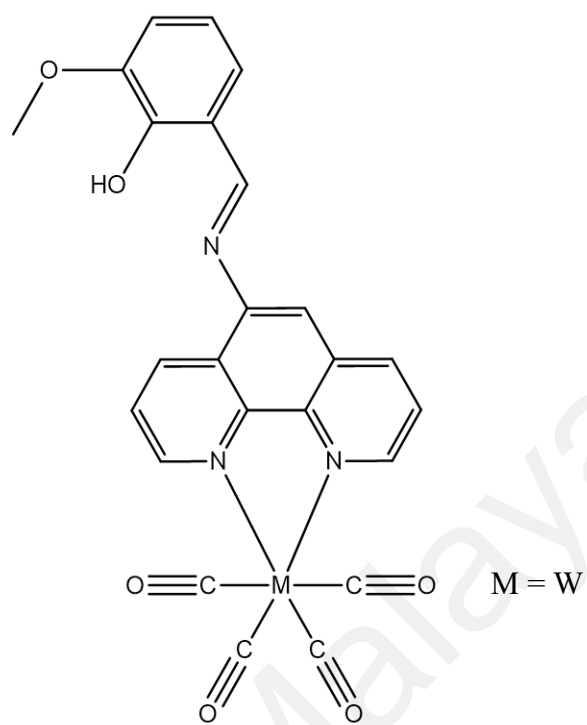


Figure 4.42: The drug-likeness bioavailability radar of T3.

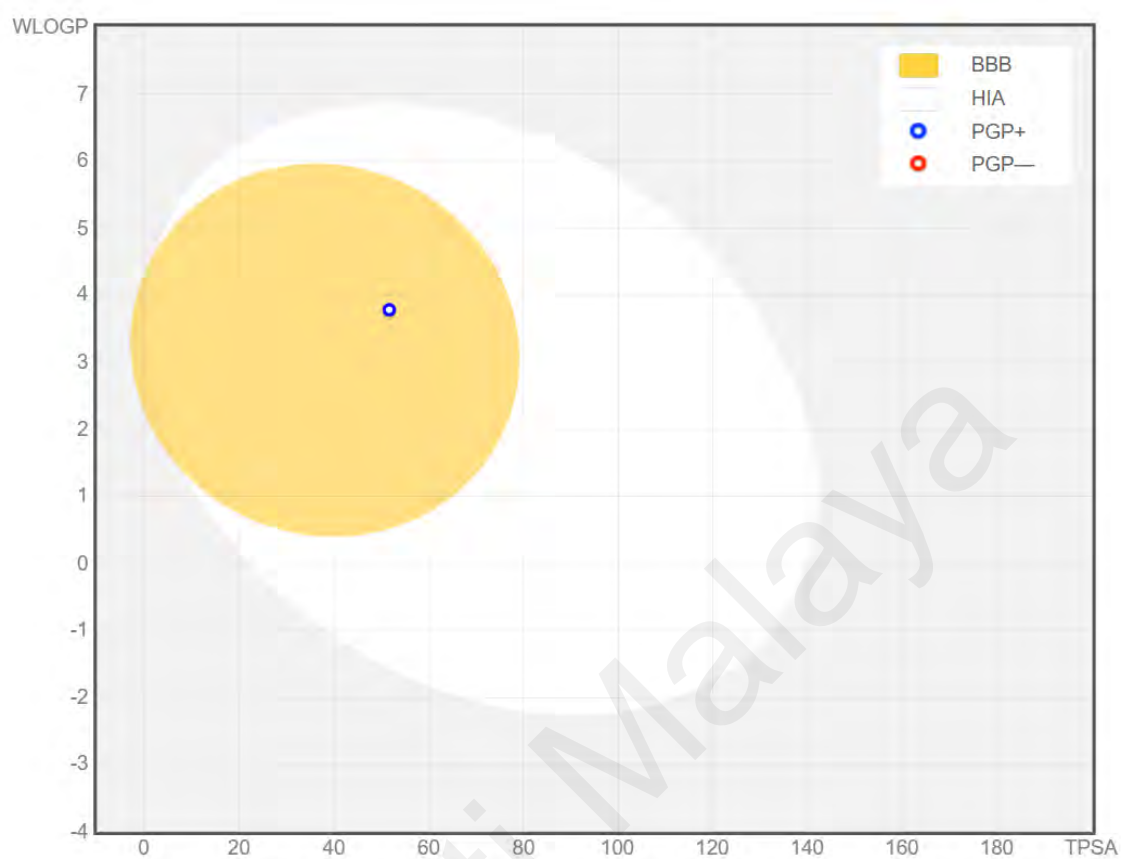


Figure 4.43: The BOILED-Egg graphical representation of T3.

4.6.4 ADME calculations of L4, C4, M4, and T4

The simulated ADME properties of fourth series compounds, namely **L4**, **C4**, **M4**, and **T4** are shown in Table 4.48. All compounds have no HBD but have 4 RotB present in the structures and the ligand **L4** has 6 HBA whereas the bimetallic photoCORMs **C4**, **M4**, and **T4** have 10 HBA. Similar to the aforementioned series compounds, the Log $P_{o/w}$ values of the compounds showed that the photoCORMs have a higher lipophilicity compared to the ligand. All compounds have parameters within the acceptable range proposed by Lipinski Ro5 except of the molecular weight in which the photoCORMs, namely **C4**, **M4**, and **T4** violated the molecular weight rule with M.W > 500 g/mol. The calculated topological polar surface area (TPSA) and Log K_p suggest that all third series compounds may have excellent cells and skin permeability with **C4** being the most skin permeable among the fourth series compounds. The Bioavailability Radar of the compounds are shown in Figure 4.44, Figure 4.46, Figure 4.48, and Figure 4.50. However, the Lipinski (Pfizer) model predicts that ligand **L4** can be potential drug but not for the photoCORMs because the compounds have M.W > 500 g/mol and the structure contained more than 10 nitrogens or oxygens due to the presence of more carbon monoxides compared to the other series photoCORMs. The BOILED-Egg graphical representations of the compounds are shown in Figure 4.45, Figure 4.47, Figure 4.49, and Figure 4.51, respectively, which evaluate the potential of the compounds in terms of passive human gastrointestinal absorption (HIA) and blood brain barrier penetration (BBB). All fourth series photoCORMs are predicted to be able to absorb in the gastrointestinal tract but not able to penetrate the BBB. However, the simulation predicts that the ligand **L4** will not be able to absorb into the gastrointestinal track and will not penetrate the BBB.

Table 4.48: ADME properties of L4, C4, M4, and T4.

	L4	C4	M4	T4
Molecular weight (g/mol)	488.54	816.61	904.54	1080.30
Consensus Log $P_{o/w}$	5.42	1.78	1.89	2.10
HBA	6	10	10	10
HBD	0	0	0	0
Rotatable bonds	4	4	4	4
TPSA (\AA^2)	76.28	44.44	44.44	44.44
Log K_p (SP) (cm/s)	-5.31	-3.76	-4.30	-5.37
BBB permeant	No	No	No	No
Drug-likeness (Lipinski [Pfizer] model)	Yes	No	No	No

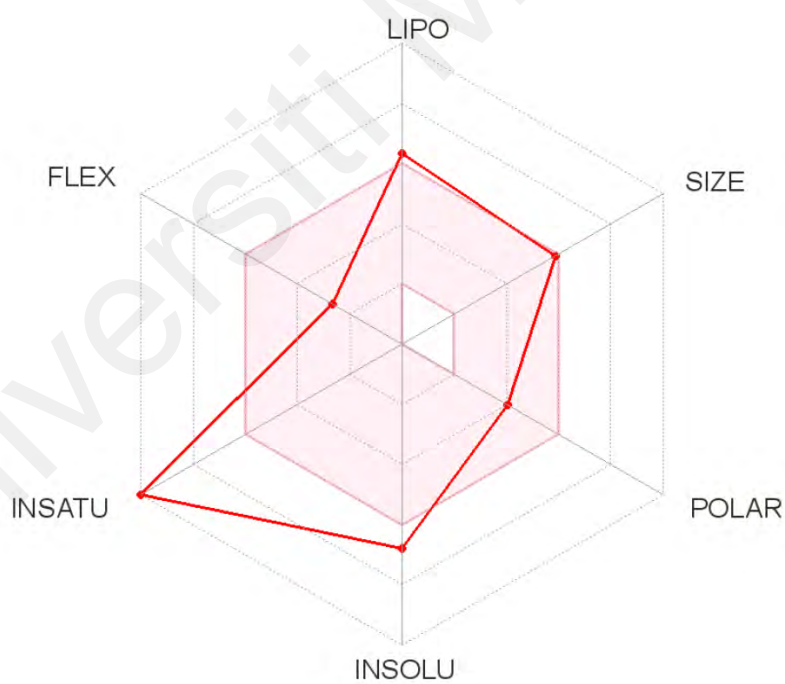
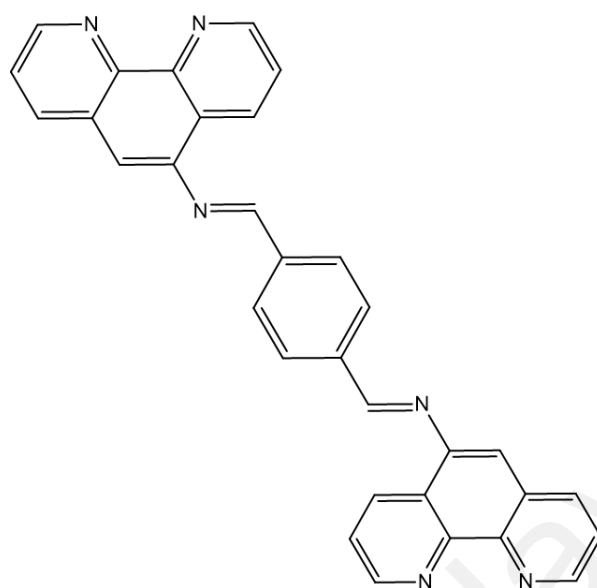


Figure 4.44: The drug-likeness bioavailability radar of L4.

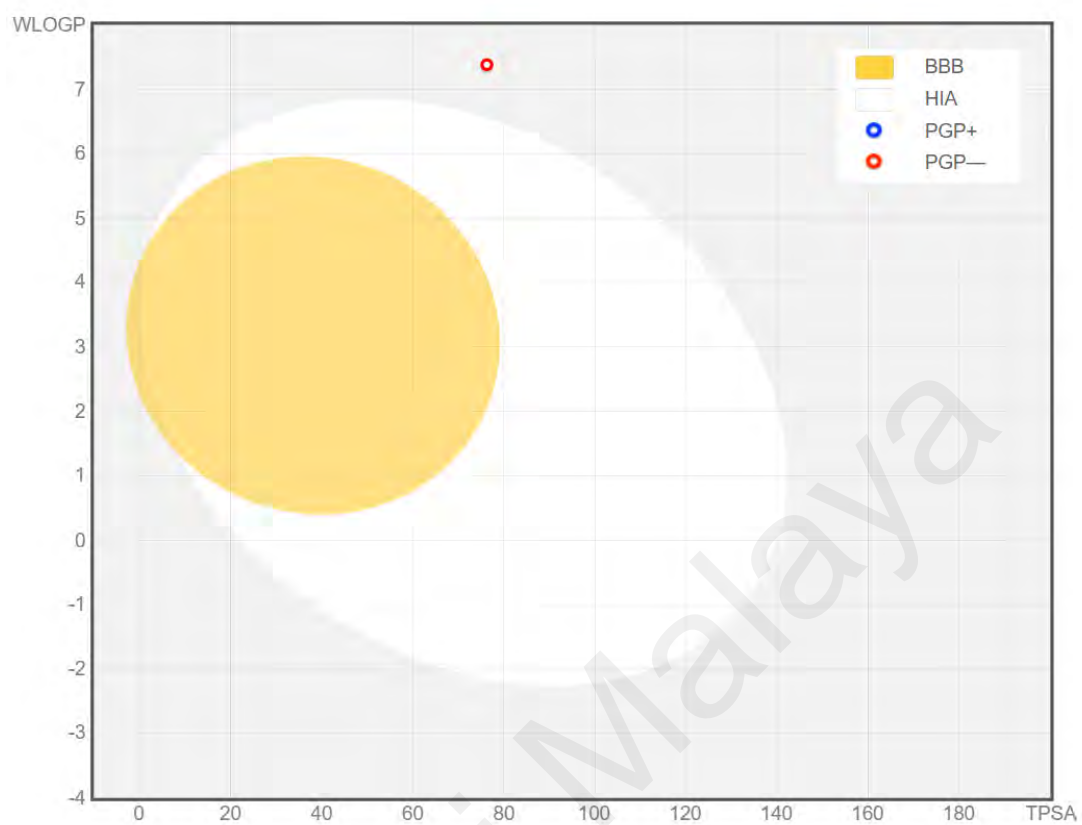


Figure 4.45: The BOILED-Egg graphical representation of L4.

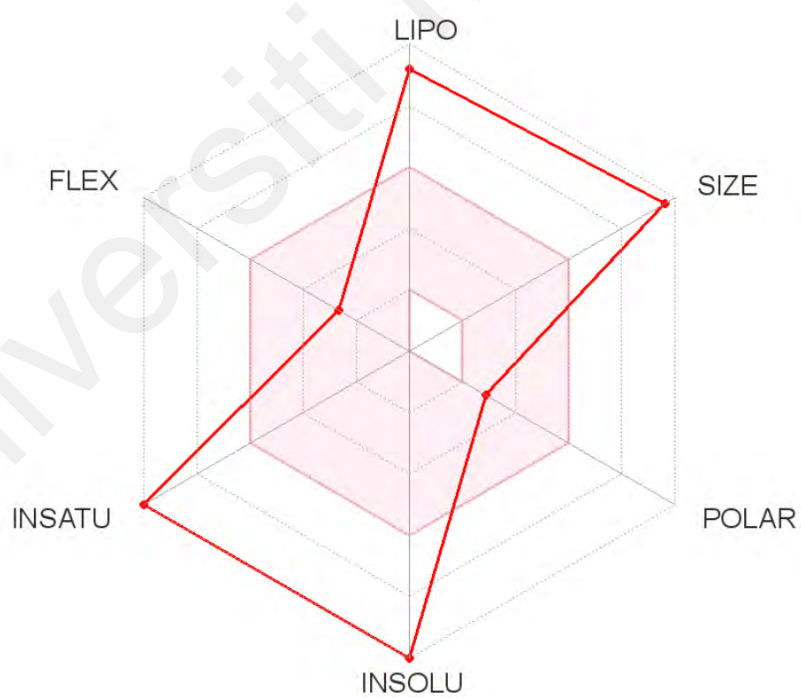
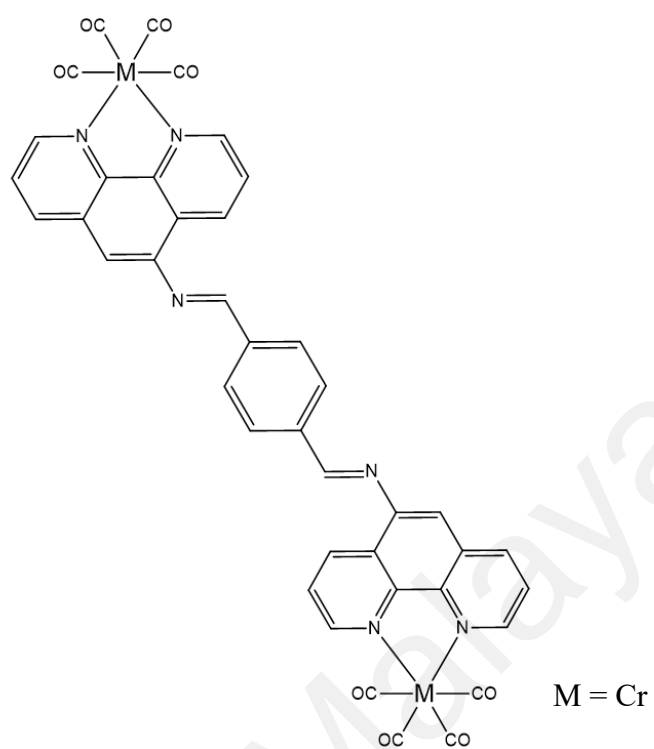


Figure 4.46: The drug-likeness bioavailability radar of C4.

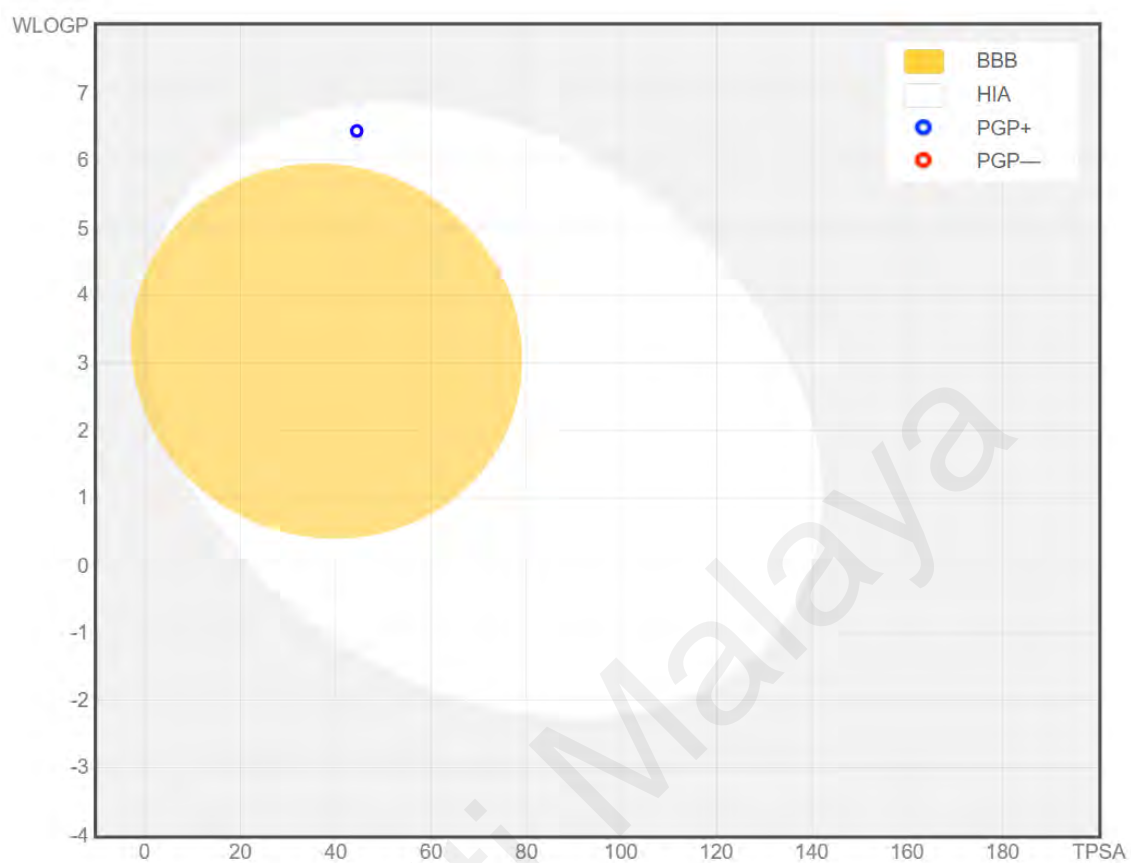


Figure 4.47: The BOILED-Egg graphical representation of C4.

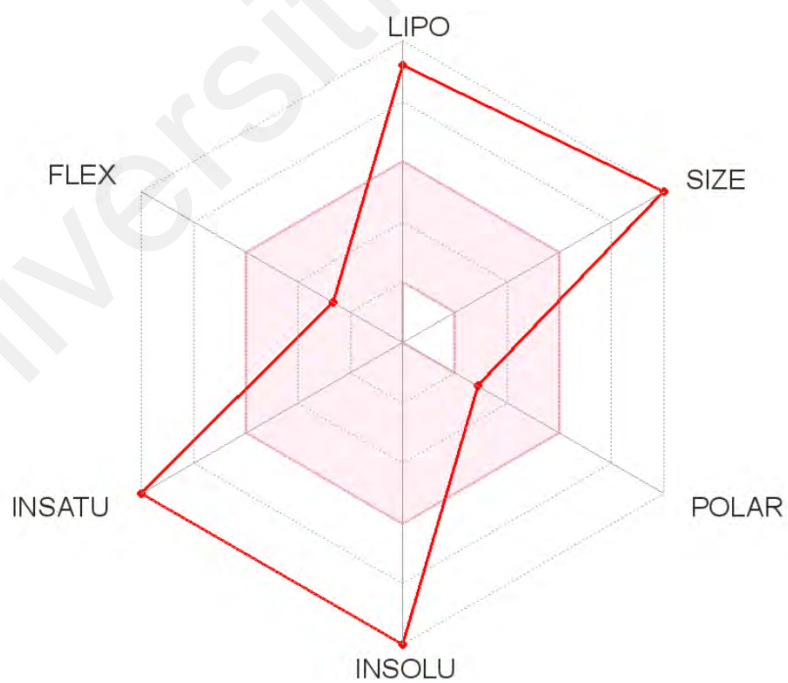
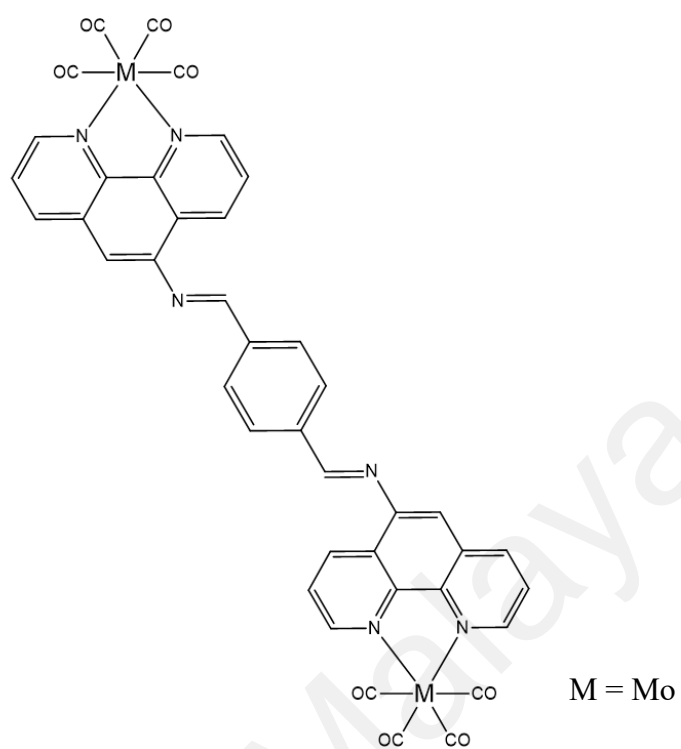


Figure 4.48: The drug-likeness bioavailability radar of M4.

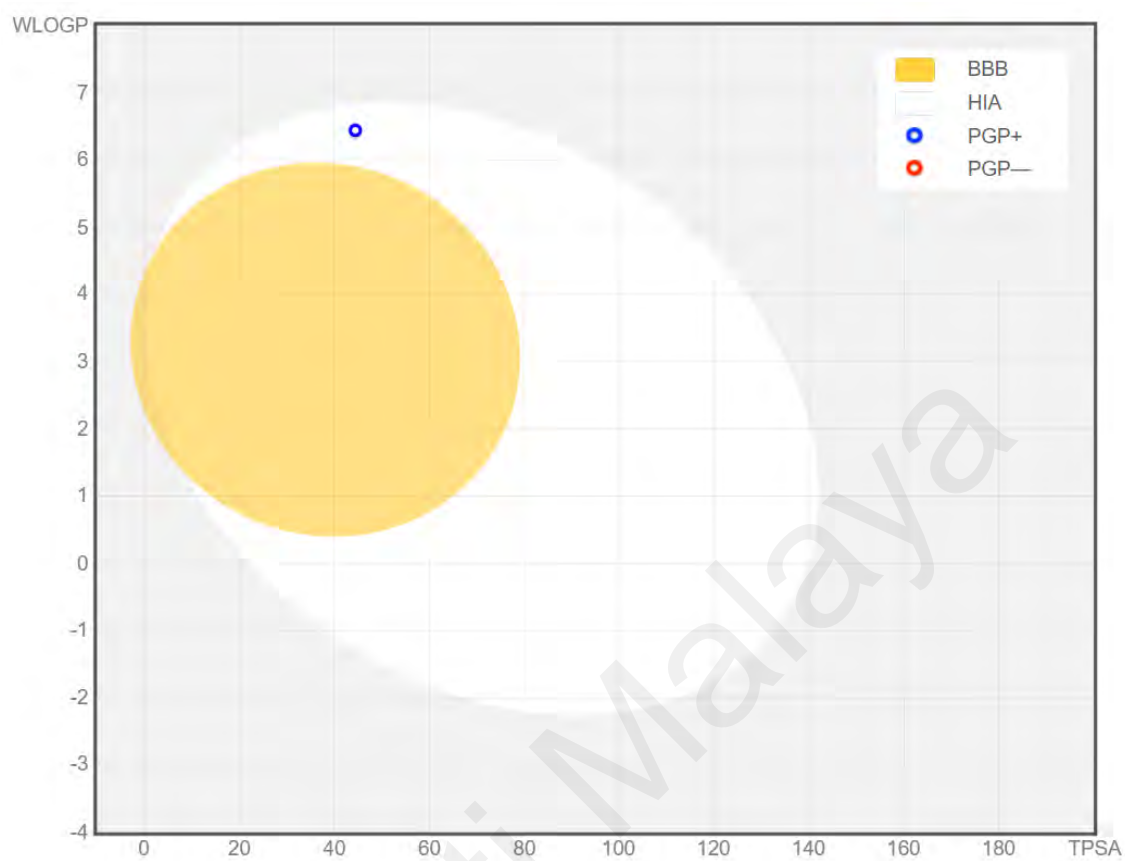


Figure 4.49: The BOILED-Egg graphical representation of M4.

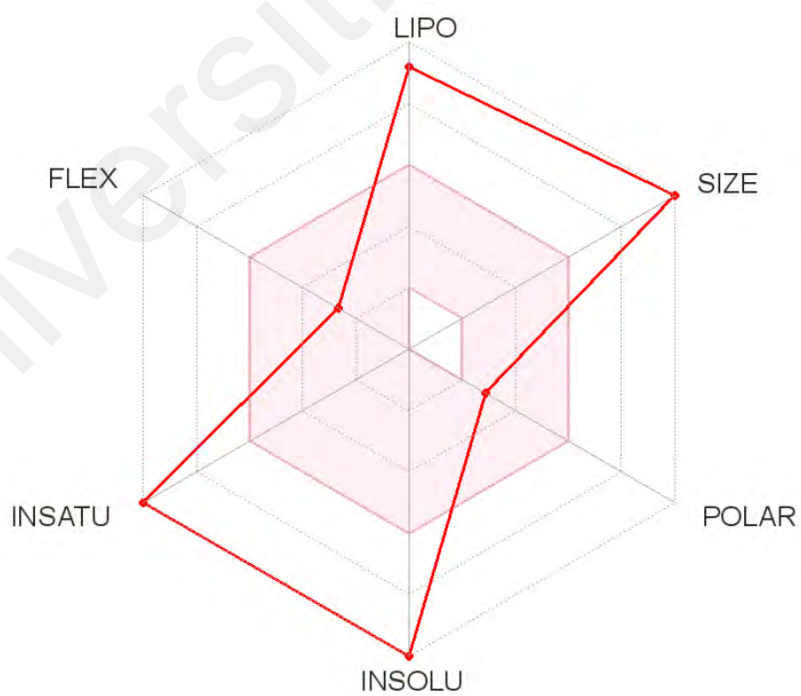
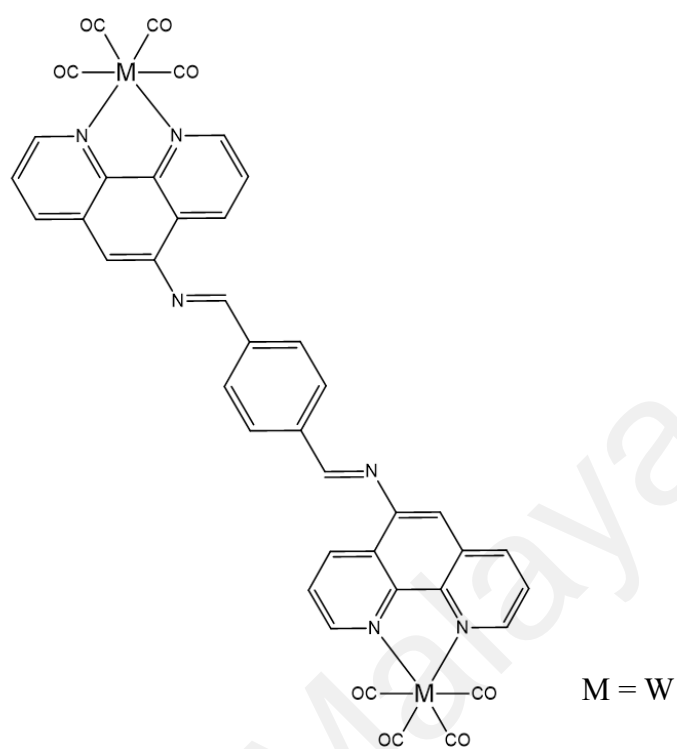


Figure 4.50: The drug-likeness bioavailability radar of T4.

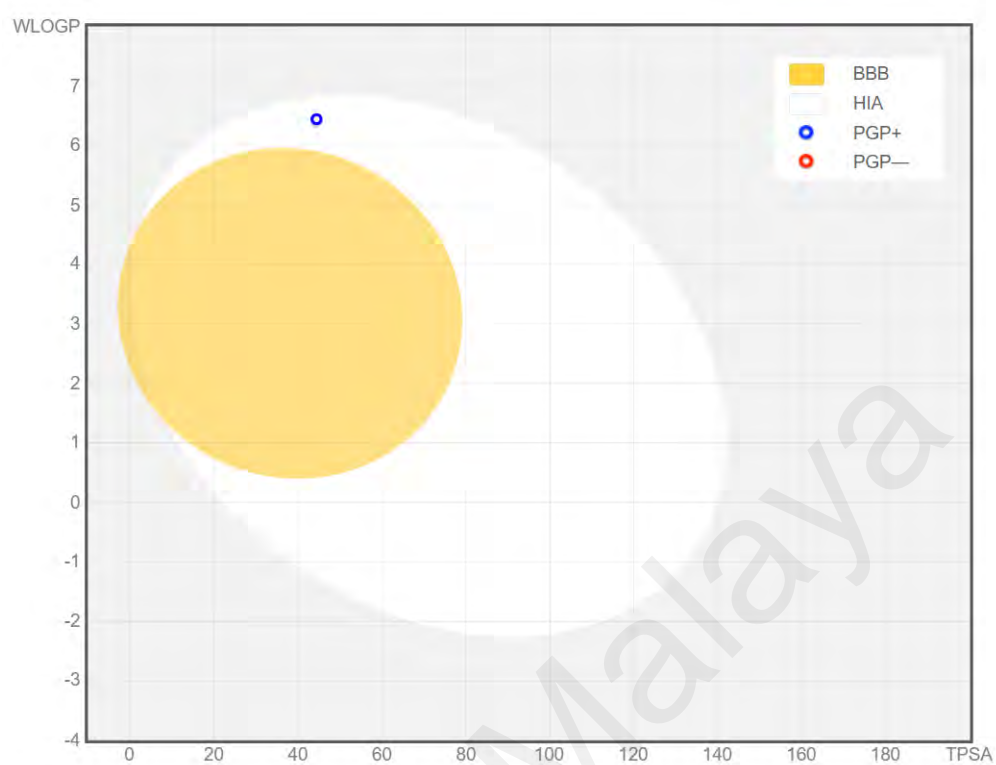


Figure 4.51: The BOILED-Egg graphical representation of T4.

4.6.5 Overall ADME calculations

The overall results predicted by the SwissADME suggest that the ligands, namely **L1**, **L2**, **L3**, and **L4** have better “drug-like” properties compared to their corresponding photoCORMs due to their lower molecular weight. Almost all the synthesized photoCORMs violated one of the Lipinski Ro5 rules with molecular weight, M.W = 500 ≤ g/mol, except for **C3**. However, despite the Ro5 violation, the Lipinski (Pfizer) model suggest that first, second and third series photoCORMs have the potentials to be drugs despite their relatively large molecular weight. The Ro5 rules are just a general guideline than actual rules for synthetic chemist. One of the most significant orally prescribed drugs approved by Food and Drug Administration (FDA) in the United State that violated all of the Lipinski Ro5 rules is Cyclosporine A. The drug is a natural product with M.W = 1202.63 g/mol and the chemical structure is shown in Figure 4.52 (Lipinski, 2016). The third series chromium photoCORM, **C3** has the most “drug-like” properties among all the synthesized photoCORMs with significant cytotoxicity and selectivity against human colon cancer cell lines, fast CO-releasing rate in the presence of UV, may be absorbed into the gastrointestinal tract, able to penetrate BBB and will be actively effluxed from the brain by PGP in the BBB. More pharmacological studies will be conducted on **C3** to determine the actual ADME and pharmacokinetics of the compound.

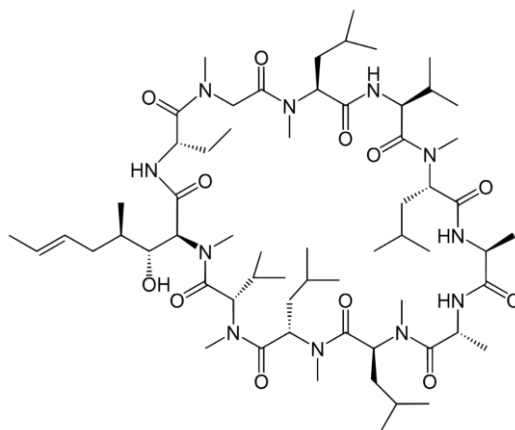


Figure 4.52: The chemical structure of Cyclosporine A.

CHAPTER 5: CONCLUSION

5.1 Conclusion

Four new series of photoCORMs based on chromium, molybdenum, and tungsten carbonyl were successfully synthesized and characterized. All photoCORMs displayed distorted octahedral structures due to the steric hindrance imposed by the ligands. A modified version of standard myoglobin assay which was termed three-layered myoglobin solution was developed and allowed a more accurate CO-releasing rates determination. In general, CO releasing rate of chromium photoCORMs are much higher than that of molybdenum and tungsten photoCORMs. The chromium photoCORMs with 2-hydroxy-3-methoxy and 2-hydroxynaphthalene moiety in its ligand had higher CO releasing rate compared to the rest. Besides, molybdenum and tungsten photoCORMs are stable in aerobic aqueous solution in the absence of light for at least 48 hours whereas chromium photoCORMs are not stable. In the absence of UV light illumination most of the ligands displayed a higher cytotoxicity compared to photoCORMs against human colorectal carcinoma and adenocarcinoma, HCT 116 and HT-29 cell lines and the ligands also showed higher antimicrobial activities compared to photoCORMs. However, in the presence of UV light illumination the cytotoxicity and cancer cell selectivity of the photoCORMs against HCT 116 and HT-29 cell lines were elevated significantly but only slight improvements were observed in the antimicrobial activities. The SwissADME simulation predicted that most of the synthesized compounds possess potential “drug-like” properties except for the bimetallic photoCORMs due to the violation of Lipinski Ro5.

5.2 Future works

1. Detailed mechanisms of CO release by the photoCORMs will be studied thereby determining the factors leading to the trend of CO release in group 6 photoCORMs.
2. Detailed biological studies will be conducted to determine the mechanism of action of the synthesized compounds in human body.
3. Physiological properties of the compounds will be conducted by using animal models and clinical studies through the collaboration with medical faculty.
4. To study the potential commercialization of the synthesized compounds as therapeutic drugs.

REFERENCES

- Aiassa, V., Zoppi, A., Becerra, M. C., Albesa, I., & Longhi, M. R. (2016). Enhanced inhibition of bacterial biofilm formation and reduced leukocyte toxicity by chloramphenicol: β -cyclodextrin: N-acetylcysteine complex. *Carbohydrate Polymers*, 152, 672-678.
- Alreja, P., & Kaur, N. (2019). "Test kit" of chromogenic and ratiometric 1, 10-phenanthroline based chemosensor for the recognition of F^- and CN^- ions. *Inorganic Chemistry Communications*, 110, 107600.
- Atkin, A. J., Lynam, J. M., Moulton, B. E., Sawle, P., Motterlini, R., Boyle, N. M., . . . Fairlamb, I. J. (2011). Modification of the deoxy-myoglobin/carbonmonoxy-myoglobin UV-vis assay for reliable determination of CO-release rates from organometallic carbonyl complexes. *Dalton Transactions*, 40(21), 5755-5761.
- Bahron, H., Khaidir, S. S., Tajuddin, A. M., Ramasamy, K., & Yamin, B. M. (2019). Synthesis, characterization and anticancer activity of mono- and dinuclear Ni(II) and Co(II) complexes of a Schiff base derived from o-vanillin. *Polyhedron*, 161, 84-92.
- Bauer, M., Huse, K., Settmacher, U., & Claus, R. A. (2008). The heme oxygenase–carbon monoxide system: regulation and role in stress response and organ failure. *Intensive Care Medicine*, 34(4), 640-648.
- Berends, H.-M., & Kurz, P. (2012). Investigation of light-triggered carbon monoxide release from two manganese photoCORMs by IR, UV–Vis and EPR spectroscopy. *Inorganica Chimica Acta*, 380, 141-147.
- Bischof, C., Joshi, T., Dimri, A., Spiccia, L., & Schatzschneider, U. (2013). Synthesis, Spectroscopic Properties, and Photoinduced CO-Release Studies of Functionalized Ruthenium(II) Polypyridyl Complexes: Versatile Building Blocks for Development of CORM–Peptide Nucleic Acid Bioconjugates. *Inorganic Chemistry*, 52(16), 9297-9308.
- Botov, S., Stamellou, E., Romanski, S., Guttentag, M., Alberto, R., Neudörfl, J.-M., . . . Schmalz, H.-G. (2013). Synthesis and Performance of Acyloxy-diene-Fe(CO)₃ Complexes with Variable Chain Lengths as Enzyme-Triggered Carbon Monoxide-Releasing Molecules. *Organometallics*, 32(13), 3587-3594.
- Brathwaite, A. D., Maner, J. A., & Duncan, M. A. (2014). Testing the limits of the 18-electron rule: the gas-phase carbonyls of Sc^+ and Y^+ . *Inorganic Chemistry*, 53(2), 1166-1169.
- Cabrales, P., Tsai, A. G., & Intaglietta, M. (2007). Hemorrhagic shock resuscitation with carbon monoxide saturated blood. *Resuscitation*, 72(2), 306-318.

- Cano, M., Campo, J. A., Ovejero, P., & Heras, J. V. (1993). Spectroscopic elucidation of the coordinative form of the DPPM ligand in $[\text{Mo}(\text{CO})_4(2\text{-dppm})]$ and *fac*- $[\text{Mo}(\text{CO})_3(2\text{-phen})(1\text{-dppm})]$ complexes: A challenging organometallic experiment for undergraduate students. *Journal of Chemical Education*, 70(7), 600.
- Cardell, L. O., Ueki, I. F., Stjärne, P., Agusti, C., Takeyama, K., Lindén, A., & Nadel, J. A. (1998). Bronchodilatation *in vivo* by carbon monoxide, a cyclic GMP related messenger. *British Journal of Pharmacology*, 124(6), 1065-1068.
- Chakraborty, I., Carrington, S. J., & Mascharak, P. K. (2014). Design strategies to improve the sensitivity of photoactive metal carbonyl complexes (photoCORMs) to visible light and their potential as CO-donors to biological targets. *Accounts of Chemical Research*, 47(8), 2603-2611.
- Chakraborty, I., Jimenez, J., & Mascharak, P. (2017). CO-Induced apoptotic death of colorectal cancer cells by a luminescent photoCORM grafted on biocompatible carboxymethyl chitosan. *Chemical Communications*, 53(40), 5519-5522.
- Chen, B., Guo, L., Fan, C., Bolisetty, S., Joseph, R., Wright, M. M., . . . George, J. F. (2009). Carbon monoxide rescues heme oxygenase-1-deficient mice from arterial thrombosis in allogeneic aortic transplantation. *The American Journal of Pathology*, 175(1), 422-429.
- Cheng, J.-P., Lin, Q.-Y., Rui-Ding, H., Zhu, W.-Z., Li, H.-Q., & Wang, D.-H. (2009). Synthesis, DNA interaction and antibacterial activities of La(III) and Gd(III) complexes of Schiff base derived from o-vanillin and lysine. *Central European Journal of Chemistry*, 7(1), 105-110.
- Choo, K. B., Mah, W. L., Lee, S. M., Lee, W. L., & Cheow, Y. L. (2018). Palladium complexes of bidentate pyridine *N*-heterocyclic carbenes: Optical resolution, antimicrobial and cytotoxicity studies. *Applied Organometallic Chemistry*, 32(8), e4377.
- Chora, Â. A., Fontoura, P., Cunha, A., Pais, T. F., Cardoso, S., Ho, P. P., . . . Soares, M. P. (2007). Heme oxygenase-1 and carbon monoxide suppress autoimmune neuroinflammation. *The Journal of Clinical Investigation*, 117(2), 438-447.
- Chung, S. W., Liu, X., Macias, A. A., Baron, R. M., & Perrella, M. A. (2008). Heme oxygenase-1-derived carbon monoxide enhances the host defense response to microbial sepsis in mice. *The Journal of Clinical Investigation*, 118(1), 239-247.
- Clark James, E., Naughton, P., Shurey, S., Green Colin, J., Johnson Tony, R., Mann Brian, E., . . . Motterlini, R. (2003). Cardioprotective Actions by a Water-Soluble Carbon Monoxide-Releasing Molecule. *Circulation Research*, 93(2), e2-e8.
- Contreras, R. H., Biekofsky, R. R., De Kowalewski, D. G., Orendt, A. M., & Facelli, J. C. (1993). Effects of electronic resonance interaction on methoxy group NMR parameters: theoretical and experimental study of substituted 2-methoxypyridines. *The Journal of Physical Chemistry*, 97(1), 91-93.

- Cordes, E., & Jencks, W. (1962). On the mechanism of Schiff base formation and hydrolysis. *Journal of the American Chemical Society*, 84(5), 832-837.
- Cotton, F. A., Darensbourg, D. J., Klein, S., & Kolthammer, B. W. S. (1982). Steric contributions to the solid-state structures of bis(phosphine) derivatives of molybdenum carbonyl. X-ray structural studies of cis-Mo(CO)₄[PPh₃-nMen]₂ (n = 0, 1, 2). *Inorganic Chemistry*, 21(1), 294-299.
- Daina, A., Michielin, O., & Zoete, V. (2017). SwissADME: a free web tool to evaluate pharmacokinetics, drug-likeness and medicinal chemistry friendliness of small molecules. *Scientific Reports*, 7(1), 1-13.
- De Backer, O., Elinck, E., Blanckaert, B., Leybaert, L., Motterlini, R., & Lefebvre, R. A. (2009). Water-soluble CO-releasing molecules reduce the development of postoperative ileus via modulation of MAPK/HO-1 signalling and reduction of oxidative stress. *Gut*, 58(3), 347-356.
- Desai, S., Desai, V., & Shingade, S. (2020a). *In-vitro* Anti-cancer assay and apoptotic cell pathway of newly synthesized benzoxazole-*N*-heterocyclic hybrids as potent tyrosine kinase inhibitors. *Bioorganic Chemistry*, 94, 103382.
- Desmard, M., Davidge, K. S., Bouvet, O., Morin, D., Roux, D., Foresti, R., . . . Montravers, P. (2009). A carbon monoxide-releasing molecule (CORM-3) exerts bactericidal activity against *Pseudomonas aeruginosa* and improves survival in an animal model of bacteraemia. *The FASEB Journal*, 23(4), 1023-1031.
- Dubuis, E., Potier, M., Wang, R., & Vandier, C. (2005). Continuous inhalation of carbon monoxide attenuates hypoxic pulmonary hypertension development presumably through activation of BKCa channels. *Cardiovascular Research*, 65(3), 751-761.
- Duckers, H. J., Boehm, M., True, A. L., Yet, S.-F., San, H., Park, J. L., . . . Nabel, E. G. (2001). Heme oxygenase-1 protects against vascular constriction and proliferation. *Nature Medicine*, 7(6), 693-698.
- Elschenbroich, C., Voss, S., Schiemann, O., Lippek, A., & Harms, K. (1998). η^1 -Coordination of Phosphinine to Chromium, Molybdenum, and Tungsten. *Organometallics*, 17(20), 4417-4424.
- Foresti, R., Hammad, J., Clark, J. E., Johnson, T. R., Mann, B. E., Friebe, A., . . . Motterlini, R. (2004). Vasoactive properties of CORM-3, a novel water-soluble carbon monoxide-releasing molecule. *British Journal of Pharmacology*, 142(3), 453-460.
- Gonzalez, M. A., Yim, M. A., Cheng, S., Moyes, A., Hobbs, A. J., & Mascharak, P. K. (2012). Manganese carbonyls bearing tripodal polypyridine ligands as photoactive carbon monoxide-releasing molecules. *Inorganic Chemistry*, 51(1), 601-608.
- Gordon, C. P., Raynaud, C., Andersen, R. A., Copéret, C., & Eisenstein, O. (2019). Carbon-13 NMR Chemical Shift: A Descriptor for Electronic Structure and Reactivity of Organometallic Compounds. *Accounts of Chemical Research*, 52(8), 2278-2289.

- Gorman, D., Drewry, A., Huang, Y. L., & Sames, C. (2003). The clinical toxicology of carbon monoxide. *Toxicology*, 187(1), 25-38.
- Guo, Y., Stein, A. B., Wu, W.-J., Tan, W., Zhu, X., Li, Q.-H., . . . Bolli, R. (2004). Administration of a CO-releasing molecule at the time of reperfusion reduces infarct size *in vivo*. *American Journal of Physiology-Heart and Circulatory Physiology*, 286(5), H1649-H1653.
- Heng, M. P., Tan, C. H., Saad, H. M., Sim, K. S., & Tan, K. W. (2020). Mitochondria-dependent apoptosis inducer: Testosterone-N4-ethylthiosemicarbazone and its metal complexes with selective cytotoxicity towards human colorectal carcinoma cell line (HCT 116). *Inorganica Chimica Acta*, 507, 119581.
- Hussein, E. M., Malik, M. S., Alsantali, R. I., Asghar, B. H., Morad, M., Ansari, M. A., . . . Ahmed, S. A. (2021). Bioactive fluorenes. Part IV: Design, synthesis, and a combined *in vitro*, *in silico* anticancer and antibacterial evaluation of new fluorene-heterocyclic sulfonamide conjugates. *Journal of Molecular Structure*, 1246, 131232.
- Hussein, M. A., Guan, T. S., Haque, R. A., Ahamed, M. B. K., & Majid, A. M. S. A. (2015). Synthesis and characterization of thiosemicarbazone molybdenum(VI) complexes: *In vitro* DNA binding, cleavage, and antitumor activities. *Polyhedron*, 85, 93-103.
- Iacono, L. L., Boczkowski, J., Zini, R., Salouage, I., Berdeaux, A., Motterlini, R., & Morin, D. (2011). A carbon monoxide-releasing molecule (CORM-3) uncouples mitochondrial respiration and modulates the production of reactive oxygen species. *Free Radical Biology and Medicine*, 50(11), 1556-1564.
- Ishak, S., Yeap, G.-Y., Shanmugapriya, Sasidharan, S., & Ito, M. M. (2019). Synthesis, molecular structure and cytotoxic studies of fluorene compound with potential anti-cancer properties. *Journal of Molecular Structure*, 1175, 763-768.
- Jackson, C. S., Schmitt, S., Dou, Q. P., & Kodanko, J. J. (2011). Synthesis, characterization, and reactivity of the stable iron carbonyl complex [Fe(CO)(N₄Py)](ClO₄)₂: photoactivated carbon monoxide release, growth inhibitory activity, and peptide ligation. *Inorganic Chemistry*, 50(12), 5336-5338.
- Jimenez, J., Chakraborty, I., Carrington, S. J., & Mascharak, P. K. (2016). Light-triggered CO delivery by a water-soluble and biocompatible manganese photoCORM. *Dalton Transactions*, 45(33), 13204-13213.
- Jimenez, J., Chakraborty, I., Dominguez, A., Martinez-Gonzalez, J., Sameera, W. M. C., & Mascharak, P. K. (2018). A Luminescent Manganese PhotoCORM for CO Delivery to Cellular Targets under the Control of Visible Light. *Inorganic Chemistry*, 57(4), 1766-1773.
- Karges, J., Xiong, K., Blacque, O., Chao, H., & Gasser, G. (2021). Highly cytotoxic copper(II) terpyridine complexes as anticancer drug candidates. *Inorganica Chimica Acta*, 516, 120137.

- Kautz, A. C., Kunz, P. C., & Janiak, C. (2016). CO-releasing molecule (CORM) conjugate systems. *Dalton Transactions*, 45(45), 18045-18063.
- Kawahara, B., Sen, S., & Mascharak, P. K. (2020). Reaction of carbon monoxide with cystathionine β -synthase: implications on drug efficacies in cancer chemotherapy. *Future Medicinal Chemistry*, 12(04), 325-337.
- Kirakci, K., Zelenka, J., Rumlova, M., Cvacka, J., Ruml, T., & Lang, K. (2019). Cationic octahedral molybdenum cluster complexes functionalized with mitochondria-targeting ligands: photodynamic anticancer and antibacterial activities. *Biomater. Sci.*, 7(4), 1386-1392.
- Klein, M., Neugebauer, U., Gheisari, A., Malassa, A., Jazzazi, T. M. A., Froehlich, F., . . . Popp, J. (2014). IR Spectroscopic Methods for the Investigation of the CO Release from CORMs. *The Journal of Physical Chemistry A*, 118(29), 5381-5390.
- Kleinpeter, E., Klod, S., & Koch, A. (2007). Visualization of through space NMR shieldings of aromatic and anti-aromatic molecules and a simple means to compare and estimate aromaticity. *Journal of Molecular Structure: Theochem*, 811(1-3), 45-60.
- Kohmoto, J., Nakao, A., Sugimoto, R., Wang, Y., Zhan, J., Ueda, H., & McCurry, K. R. (2008). Carbon monoxide-saturated preservation solution protects lung grafts from ischemia-reperfusion injury. *The Journal of Thoracic and Cardiovascular Surgery*, 136(4), 1067-1075.
- Kretschmer, R., Gessner, G., Görls, H., Heinemann, S. H., & Westerhausen, M. (2011). Dicarbonyl-bis (cysteamine) iron (II): a light induced carbon monoxide releasing molecule based on iron (CORM-S1). *Journal of Inorganic Biochemistry*, 105(1), 6-9.
- Kubeil, M., Vernooij, R. R., Kubeil, C., Wood, B. R., Graham, B., Stephan, H., & Spiccia, L. (2017). Studies of carbon monoxide release from ruthenium (II) bipyridine carbonyl complexes upon UV-light exposure. *Inorganic Chemistry*, 56(10), 5941-5952.
- Kunz, P. C., Meyer, H., Barthel, J., Sollazzo, S., Schmidt, A. M., & Janiak, C. (2013). Metal carbonyls supported on iron oxide nanoparticles to trigger the CO-gasotransmitter release by magnetic heating. *Chemical Communications*, 49(43), 4896-4898.
- Kupwade, R., & Sawant, V. (2020). Carbonyl releasing Schiff base complex of Fe(III): synthesis, physicochemical characterization, antimicrobial and anticancer studies. *Journal of Chemical Sciences*, 132(1), 1-12.
- Lakshman, T. R., Deb, J., Ghosh, I., Sarkar, S., & Paine, T. K. (2019). Combining anti-inflammatory and anti-proliferative activities in ternary metal-NSAID complexes of a polypyridylamine ligand. *Inorganica Chimica Acta*, 486, 663-668.
- Lee, S. K., Tan, K. W., & Ng, S. W. (2014). Zinc, copper and nickel derivatives of 2-[2-bromoethyliminomethyl] phenol as topoisomerase inhibitors exhibiting anti-proliferative and anti-metastatic properties. *RSC Advances*, 4(104), 60280-60292.

- Lipinski, C. A. (2016). Rule of five in 2015 and beyond: Target and ligand structural limitations, ligand chemistry structure and drug discovery project decisions. *Advanced Drug Delivery Reviews*, 101, 34-41.
- Lipinski, C. A., Lombardo, F., Dominy, B. W., & Feeney, P. J. (1997). Experimental and computational approaches to estimate solubility and permeability in drug discovery and development settings. *Advanced Drug Delivery Reviews*, 23(1-3), 3-25.
- Mann, B. E. (2010). Carbon monoxide: an essential signalling molecule. In *Medicinal organometallic chemistry* (pp. 247-285): Springer.
- Mann, B. E., & Motterlini, R. (2007). CO and NO in medicine. *Chemical Communications*(41), 4197-4208.
- Mansour, A. M. (2017). Rapid green and blue light-induced CO release from bromazepam Mn (I) and Ru (II) carbonyls: synthesis, density functional theory and biological activity evaluation. *Applied Organometallic Chemistry*, 31(2), e3564.
- Matuszewska, A., Jaszek, M., Stefaniuk, D., Ciszewski, T., & Matuszewski, Ł. (2018). Anticancer, antioxidant, and antibacterial activities of low molecular weight bioactive subfractions isolated from cultures of wood degrading fungus *Cerrena unicolor*. *PloS One*, 13(6), e0197044.
- McLean, S., Mann, B. E., & Poole, R. K. (2012). Sulfite species enhance carbon monoxide release from CO-releasing molecules: implications for the deoxymyoglobin assay of activity. *Analytical Biochemistry*, 427(1), 36-40.
- Mendel, R. R. (2005). Molybdenum: biological activity and metabolism. *Dalton Transactions* (21), 3404-3409.
- Meyer, H., Winkler, F., Kunz, P., Schmidt, A. M., Hamacher, A., Kassack, M. U., & Janiak, C. (2015). Stabilizing alginate confinement and polymer coating of CO-releasing molecules supported on iron oxide nanoparticles to trigger the CO release by magnetic heating. *Inorganic Chemistry*, 54(23), 11236-11246.
- Mishra, S., Fujita, T., Lama, V. N., Nam, D., Liao, H., Okada, M., . . . Pinsky, D. J. (2006). Carbon monoxide rescues ischemic lungs by interrupting MAPK-driven expression of early growth response 1 gene and its downstream target genes. *Proceedings of the National Academy of Sciences*, 103(13), 5191-5196.
- Moondra, S., Maheshwari, R., Taneja, N., Tekade, M., & Tekadle, R. K. (2018). Chapter 6 - Bulk Level Properties and its Role in Formulation Development and Processing. In R. K. Tekade (Ed.), *Dosage Form Design Parameters* (pp. 221-256): Academic Press.
- Morita, T., Mitsialis, S. A., Koike, H., Liu, Y., & Kourembanas, S. (1997). Carbon monoxide controls the proliferation of hypoxic vascular smooth muscle cells. *Journal of Biological Chemistry*, 272(52), 32804-32809.

- Motterlini, R., Clark James, E., Foresti, R., Sarathchandra, P., Mann Brian, E., & Green Colin, J. (2002). Carbon Monoxide-Releasing Molecules. *Circulation Research*, 90(2), e17-e24.
- Motterlini, R., Clark, J. E., Foresti, R., Sarathchandra, P., Mann, B. E., & Green, C. J. (2002). Carbon monoxide-releasing molecules: characterization of biochemical and vascular activities. *Circulation Research*, 90(2), 17-24.
- Motterlini, R., & Otterbein, L. E. (2010). The therapeutic potential of carbon monoxide. *Nature Reviews Drug Discovery*, 9(9), 728-743.
- Nagel, C., McLean, S., Poole, R. K., Braunschweig, H., Kramer, T., & Schatzschneider, U. (2014). Introducing $[\text{Mn}(\text{CO})_3(\text{tpa-}\kappa_3\text{N})]^+$ as a novel photoactivatable CO-releasing molecule with well-defined iCORM intermediates—synthesis, spectroscopy, and antibacterial activity. *Dalton Transactions*, 43(26), 9986-9997.
- Nakao, A., Toyokawa, H., Abe, M., Kiyomoto, T., Nakahira, K., Choi, A. M., . . . Murase, N. (2006). Heart allograft protection with low-dose carbon monoxide inhalation: effects on inflammatory mediators and alloreactive T-cell responses. *Transplantation*, 81(2), 220-230.
- Niesel, J., Pinto, A., Peindy N'Dongo, H. W., Merz, K., Ott, I., Gust, R., & Schatzschneider, U. (2008). Photoinduced CO release, cellular uptake and cytotoxicity of a tris(pyrazolyl)methane (tpm) manganese tricarbonyl complex. *Chemical Communications* (15), 1798-1800.
- Nobre, L. S., Jeremias, H., Romão, C. C., & Saraiva, L. M. (2016). Examining the antimicrobial activity and toxicity to animal cells of different types of CO-releasing molecules. *Dalton Transactions*, 45(4), 1455-1466.
- Otterbein, L. E., Mantell, L. L., & Choi, A. M. (1999). Carbon monoxide provides protection against hyperoxic lung injury. *American Journal of Physiology-Lung Cellular and Molecular Physiology*, 276(4), L688-L694.
- Otterbein, L. E., Otterbein, S. L., Ifedigbo, E., Liu, F., Morse, D. E., Fearn, C., . . . Choi, A. M. (2003). MKK3 mitogen-activated protein kinase pathway mediates carbon monoxide-induced protection against oxidant-induced lung injury. *The American Journal of Pathology*, 163(6), 2555-2563.
- Pfeiffer, H., Sowik, T., & Schatzschneider, U. (2013). Bioorthogonal oxime ligation of a $\text{Mo}(\text{CO})_4(\text{N-N})$ CO-releasing molecule (CORM) to a TGF β -binding peptide. *Journal of Organometallic Chemistry*, 734, 17-24.
- Pierri, A. E., Pallaoro, A., Wu, G., & Ford, P. C. (2012). A Luminescent and Biocompatible PhotoCORM. *Journal of the American Chemical Society*, 134(44), 18197-18200.
- Poh, H. T., Sim, B. T., Chwee, T. S., Leong, W. K., & Fan, W. Y. (2014). The dithiolate-bridged diiron hexacarbonyl complex $\text{Na}_2[(\mu\text{-SCH}_2\text{CH}_2\text{COO})\text{Fe}(\text{CO})_3]_2$ as a water-soluble PhotoCORM. *Organometallics*, 33(4), 959-963.

- Ren, Y., D'Ambrosio, M. A., Wang, H., Liu, R., Garvin, J. L., & Carretero, O. A. (2008). Heme oxygenase metabolites inhibit tubuloglomerular feedback (TGF). *American Journal of Physiology-Renal Physiology*, 295(4), F1207-F1212.
- Rimmer, R. D., Pierri, A. E., & Ford, P. C. (2012). Photochemically activated carbon monoxide release for biological targets. Toward developing air-stable photoCORMs labilized by visible light. *Coordination Chemistry Reviews*, 256(15-16), 1509-1519.
- Rimmer, R. D., Richter, H., & Ford, P. C. (2010). A Photochemical Precursor for Carbon Monoxide Release in Aerated Aqueous Media. *Inorganic Chemistry*, 49(3), 1180-1185.
- Rodríguez, M. R., Balsa, L. M., Del Pla, J., García-Tojal, J., Pis-Diez, R., Parajón-Costa, B. S., . . . González-Baró, A. C. (2019). Synthesis, characterization, DFT calculations and anticancer activity of a new oxidovanadium (iv) complex with a ligand derived from o-vanillin and thiophene. *New Journal of Chemistry*, 43(29), 11784-11794.
- Romanski, S., Kraus, B., Schatzschneider, U., Neudörfl, J. M., Amslinger, S., & Schmalz, H. G. (2011). Acyloxybutadiene iron tricarbonyl complexes as enzyme-triggered CO-releasing molecules (ET-CORMs). *Angewandte Chemie, International Edition in English*, 50(10), 2392-2396.
- Romão, C. C., Blättler, W. A., Seixas, J. D., & Bernardes, G. J. (2012). Developing drug molecules for therapy with carbon monoxide. *Chemical Society Reviews*, 41(9), 3571-3583.
- Romão, M. J. (2009). Molybdenum and tungsten enzymes: a crystallographic and mechanistic overview. *Dalton Transactions* (21), 4053-4068.
- Ryter, S. W., & Otterbein, L. E. (2004). Carbon monoxide in biology and medicine. *Bioessays*, 26(3), 270-280.
- Santos-Silva, T., Mukhopadhyay, A., Seixas, J. D., Bernardes, G. J. L., Romão, C. C., & Romão, M. J. (2011). CORM-3 Reactivity toward Proteins: The Crystal Structure of a Ru(II) Dicarbonyl–Lysozyme Complex. *Journal of the American Chemical Society*, 133(5), 1192-1195.
- Sari, S., Koçak, E., Kart, D., Özdemir, Z., Acar, M. F., Sayoğlu, B., . . . Dalkara, S. (2021). Azole derivatives with naphthalene showing potent antifungal effects against planktonic and biofilm forms of *Candida Spp.*: An *in vitro* and *in silico* study. *International Microbiology*, 24(1), 93-102.
- Sato, K., Balla, J., Otterbein, L., Smith, R. N., Brouard, S., Lin, Y., . . . Vercellotti, G. (2001). Carbon monoxide generated by heme oxygenase-1 suppresses the rejection of mouse-to-rat cardiac transplants. *The Journal of Immunology*, 166(6), 4185-4194.

- Savir, S., Wei, Z. J., Liew, J. W. K., Vythilingam, I., Lim, Y. A. L., Saad, H. M., . . . Tan, K. W. (2020). Synthesis, cytotoxicity and antimalarial activities of thiosemicarbazones and their nickel (II) complexes. *Journal of Molecular Structure*, 128090.
- Schallner, N., Romão, C. C., Biermann, J., Lagrèze, W. A., Otterbein, L. E., Buerkle, H., . . . Goebel, U. (2013). Carbon monoxide abrogates ischemic insult to neuronal cells via the soluble guanylate cyclase-cGMP pathway. *PloS One*, 8(4), e60672.
- Slanina, T., & Šebej, P. (2018). Visible-light-activated photoCORMs: Rational design of CO-releasing organic molecules absorbing in the tissue-transparent window. *Photochemical & Photobiological Sciences*, 17(6), 692-710.
- Tidwell, T. T. (2008). Hugo (Ugo) Schiff, Schiff bases, and a century of β -lactam synthesis. *Angewandte Chemie International Edition*, 47(6), 1016-1020.
- Tinajero-Trejo, M., Rana, N., Nagel, C., Jesse, H. E., Smith, T. W., Wareham, L. K., . . . Poole, R. K. (2016). Antimicrobial Activity of the Manganese Photoactivated Carbon Monoxide-Releasing Molecule $[\text{Mn}(\text{CO})_3(\text{tpa}-\kappa(3)\text{N})]^+$ Against a Pathogenic *Escherichia coli* that Causes Urinary Infections. *Antioxidants & Redox Signaling*, 24(14), 765-780.
- Tsoyi, K., Lee, T. Y., Lee, Y. S., Kim, H. J., Seo, H. G., Lee, J. H., & Chang, K. C. (2009). Heme-oxygenase-1 induction and carbon monoxide-releasing molecule inhibit lipopolysaccharide (LPS)-induced high-mobility group box 1 release in vitro and improve survival of mice in LPS-and cecal ligation and puncture-induced sepsis model *in vivo*. *Molecular Pharmacology*, 76(1), 173-182.
- Tsui, T.-Y., Obed, A., Siu, Y.-T., Yet, S.-F., Prantl, L., Schlitt, H. J., & Fan, S.-T. (2007). Carbon monoxide inhalation rescues mice from fulminant hepatitis through improving hepatic energy metabolism. *Shock*, 27(2), 165-171.
- Ulbrich, F., Hagmann, C., Buerkle, H., Romao, C. C., Schallner, N., Goebel, U., & Biermann, J. (2017). The Carbon monoxide releasing molecule ALF-186 mediates anti-inflammatory and neuroprotective effects via the soluble guanylate cyclase ss1 in rats' retinal ganglion cells after ischemia and reperfusion injury. *Journal of Neuroinflammation*, 14(1), 1-14.
- Wang, G., Liu, W., Peng, Z., Huang, Y., Gong, Z., & Li, Y. (2020). Design, synthesis, molecular modeling, and biological evaluation of pyrazole-naphthalene derivatives as potential anticancer agents on MCF-7 breast cancer cells by inhibiting tubulin polymerization. *Bioorganic Chemistry*, 103, 104141.
- Weaver, L. K. (2009). Carbon monoxide poisoning. *New England Journal of Medicine*, 360(12), 1217-1225.
- Wilson, J. L., Jesse, H. E., Hughes, B., Lund, V., Naylor, K., Davidge, K. S., . . . Poole, R. K. (2013). $\text{Ru}(\text{CO})_3\text{Cl}(\text{Glycinate})$ (CORM-3): a carbon monoxide-releasing molecule with broad-spectrum antimicrobial and photosensitive activities against respiration and cation transport in *Escherichia coli*. *Antioxidants & Redox Signaling*, 19(5), 497-509.

- Wright, M. A., & Wright, J. A. (2016). PhotoCORMs: CO release moves into the visible. *Dalton Transactions*, 45(16), 6801-6811.
- Yabluchanskiy, A., Sawle, P., Homer-Vanniasinkam, S., Green, C. J., Foresti, R., & Motterlini, R. (2012). CORM-3, a carbon monoxide-releasing molecule, alters the inflammatory response and reduces brain damage in a rat model of hemorrhagic stroke. *Critical Care Medicine*, 40(2), 544-552.
- Zhang, W.-Q., Atkin, A. J., Fairlamb, I. J., Whitwood, A. C., & Lynam, J. M. (2011). Synthesis and reactivity of molybdenum complexes containing functionalized alkynyl ligands: A photochemically activated CO-releasing molecule (PhotoCORM). *Organometallics*, 30(17), 4643-4654.
- Zobi, F. (2013). CO and CO-releasing molecules in medicinal chemistry. *Future Medicinal Chemistry*, 5(2), 175-188.
- Zobi, F., Quaroni, L., Santoro, G., Zlateva, T., Blacque, O., Sarafimov, B., . . . Bogdanova, A. Y. (2013). Live-fibroblast IR imaging of a cytoprotective photoCORM activated with visible light. *Journal of Medicinal Chemistry*, 56(17), 6719-6731.
- Zuckerbraun, B. S., Chin, B. Y., Wegiel, B., Billiar, T. R., Czimadia, E., Rao, J., . . . Otterbein, L. E. (2006). Carbon monoxide reverses established pulmonary hypertension. *The Journal of Experimental Medicine*, 203(9), 2109-2119.
- Zuckerbraun, B. S., McCloskey, C. A., Gallo, D., Liu, F., Ifedigbo, E., Otterbein, L. E., & Billiar, T. R. (2005). Carbon monoxide prevents multiple organ injury in a model of hemorrhagic shock and resuscitation. *Shock*, 23(6), 527-532.